Carsten Pietzka

Characterization of Oxygen-terminated Diamond Electrodes for Electrochemical Applications

Cuvillier Verlag Göttingen
Internationaler wissenschaftlicher Fachverlag

ulm university universität

uulm

Characterization of Oxygen-terminated Diamond Electrodes for Electrochemical Applications

DISSERTATION

zur Erlangung des akademischen Grades eines

DOKTOR-INGENIEURS

(DR.-ING.)

der Fakultät für Ingenieurwissenschaften
und Informatik der Universität Ulm

von

CARSTEN PIETZKA

AUS SÖGEL

Contents

List of Figures

List of symbols

C	capacitance
C_{DL}	double-layer capacitance
C_{SC}	depletion-layer (space charge) capacitance
$\underline{C}$	complex capacitance
c_0	reference concentration
c_b	bulk concentration in electrolyte
$c_{H_3O^+}$	H_3O^+ concentration
D	diffusion constant
d_A	thickness of layer A
d_{CO}	thickness of C-O-layer
$d_{\alpha C}$, $d_{\alpha C1}$, $d_{\alpha C2}$	thicknesses of α-C layers
E	energy
E_a	activation energy of dopants
E_b	binding energy
E_g	bandgap
E_{kin}	kinetic energy
F	Faraday constant
f	measurement frequency
h	Planck constant
I_A, I_B	intensities
I_{A0}, I_{B0}	maximum intensities
J	current density
J_0	exchange current density
k_B	Boltzmann constant
m^*	effective mass
N_A	acceptor concentration
n	n-factor of constant phase element

$n(x)$	charge carrier profile
Q	charge
Q_0	nominal capacitance of constant phase element
q	elementary charge
R_1	resistance
R_{CT}	charge-transfer resistance
R_{DL}	double-layer resistance
R_g	gas constant
R_{GB}	resistance across grain boundaries
R_{SC}	depletion layer resistance
r_0	radius of microelectrode
s	scan rate
T	absolute temperature
t	time
V, V_s	electrode potential
V_0	equilibrium potential of redox reaction
V_{FB}	flatband potential
V_{OCP}	open-circuit potential
Z	impedance
$\underline{Z}$	complex impedance
z	number of exchanged electrons
α	transfer coefficient
β_A	surface coverage with layer A
ϵ_0	dielectric constant
ϵ_r	relative permittivity
λ	escape length of photoelectrons
ν	frequency (X-rays)
θ	detection angle
Φ_{det}	work function of photoelectron detector
Φ_{SC}	potential drop across depletion layer
ϕ_B	electronic surface barrier
ω	circular frequency

Abstract

The topic of this thesis is the electrochemical characterization of oxygen-terminated single-crystal- and nanocrystalline diamond electrodes. Diamond is a very attractive material for bio- and electrochemical applications due to its exceptional stability, its biocompatibility, and its electrochemical properties like wide potential window of water dissociation and low background current. The oxygen-termination improves the stability of the electrode characteristics, which is the main advantage compared to the hydrogen termination, which is apparent directly after growth.

However, the characterisitcs of oxygen-terminated diamond electrodes are very dependent on the oxidation treatment, as it is shown in this work. Four different oxidation treatments are investigated by electrochemical measurements: Wet-chemical oxidation in a H_2SO_4/H_2O_2 mixture, anodic oxidation in KOH, RF oxygen plasma without DC bias and an etching process in argon/oxygen plasma including a DC bias. The electrode characterisitcs are correlated with the results from X-ray photoemission spectroscopy (XPS) measurements. It is shown that these oxidation treatments induce different carbon-oxygen functional groups on the diamond surface. In addition, plasma treatments can lead to sp^2-like defects, especially in the case of the argon/oxygen etching process. In the latter case, the plasma process results in a thin layer of non-diamond phases, which is expected to degrade the performance of the diamond electrodes exposed to this treatment. The different carbon-oxygen surface groups and the different amounts of sp^2-like defects have a significant influence on the electrochemical characterisitcs of the corresponding diamond electrodes, which can be observed by cyclic voltammetry and electrochemical impedance spectroscopy measurements. These two measurement techniques play an important role in the characterization of the diamond electrodes and are therefore discussed in detail. One important parameter which is investigated is the electronic surface barrier of diamond in contact to the electrolyte, which can vary over a range from below 1.0 eV to almost 2.0 eV depending on the oxidation treatment.

Apart from the oxidation treatments, the cases of single-crystal and nanocrystalline diamond are compared. It is shown that the grain boundary network can also affect the characterisitcs of diamond electrodes.

Within this thesis, possible applications of diamond are introduced: It is shown that diamond electrodes can be used for the detection of ethanol at high anodic potentials. Besides, promising electrode concepts could be the fabrication of sub-microelectrode arrays or diamond electrodes with metal nanoparticles. These two electrode concepts are also analyzed by cyclic voltammetry and impedance spectroscopy and show heterogeneous characterisitcs including active and non-active surface areas, which is important for further optimization of these devices.

Finally, this work gives also a short overview about the electrochemical characterisitcs of gallium nitride and indium nitride electrodes. Such III-nitride electrodes are also considered to be relatively inert and therefore promising for electrochemical applications. However, it is shown that these materials are not fully stable under high anodic potentials. This shows that diamond is indeed a promising electrode material for the operation under extreme conditions.

Chapter 1

Introduction

Diamond has attracted much attention due to its promising electrical, mechanical, and electrochemical properties. The wide bandgap of approx. 5.4 eV, the high electrical breakdown field, the high saturation velocities for holes and electrons and the high thermal conductivity are expected to enable the use of diamond for electronic devices for high power- and high temperature applications which cannot be realized with silicon-based MOS devices. Another promising field of application are micro-electro-mechanical systems (MEMS) like switches or mechanical sensors, since diamond has also attractive mechanical properties like a high Young´s modulus or a high fracture strength.

In addition, diamond is exceptionally chemically stable, which makes it an ideal material for electrochemical applications in harsh environments, like waste water treatments or electrochemical sensing in a wide range of pH. Other important electrochemical characteristics of diamond are the wide potential window of water dissociation and the extremely low background current. Besides, diamond is a biocompatible and optically transparent material. This is essential for the analysis of biochemical processes with simultaneous fluorescence measurements. However, the electrochemical properties of diamond are strongly dependent on the surface termination and are therefore sensitive to surface treatments. One common example is the oxidation of the hydrogen-terminated diamond surface, e.g. by chemical or plasma treatments. For applications under strong oxidizing conditions, oxygen-terminated diamond is therefore the standard material. However, there is a variety of different carbon-oxygen functional groups with different bond strengths possible on the diamond surface. Therefore, the electronic and electrochemical properties of diamond oxidized by different surface treatments might not be the same. To optimize the characteristics of diamond for electro- or biochemical applications, it is therefore necessary to analyze and understand the effect of different surface treatments on the electrochemical properties of diamond.

Another important point is that poly- or nanocrystalline diamond is used for many practical applications, since the growth of single-crystal diamond is cur-

rently limited to relatively small samples. The characteristics of nanocrystalline diamond might differ from those of single-crystal diamond due to the grain boundary network, which might have sp^2-like characteristics.

This work describes the characterization of oxygen-terminated boron-doped diamond for electrochemical applications. The work is focussed on the effect of different surface oxidation treatments on the electrochemical and electronic properties like the electronic surface barrier in contact with an electrolyte, the potential window of water dissociation, the background current, and the oxygen evolution characteristics. The characterization will be performed for single-crystal and nanocrystalline diamond electrodes.

After an introduction summarizing the electrochemical properties of diamond (chapter 2), the growth of diamond films by chemical vapor deposition will be shortly described in chapter 3. In chapter 4, the electrochemical measurement methods used for the characterization of the diamond electrodes will be explained. This analysis is another important point of this work. This chapter also contains an introduction into the characteristics of a semiconductor-electrolyte interface. In chapter 5, the oxidation of diamond by wet-chemical, electrochemical and plasma treatments will be explained. It will be shown by X-ray photoemission spectroscopy (XPS) that these oxidation treatments induce different carbon-oxygen groups on the diamond surface as well as different amounts of sp^2-content. The effect of these surface treatments on the electrochemical characteristics of diamond electrodes will be shown in chapter 6, which is one of the main parts of this work.

In chapter 7, possible applications of diamond in electrochemistry are shown. This chapter describes the use of diamond electrodes for the oxidation of ethanol, the fabrication of sub-microelectrode arrays realized completely in diamond and nanocrystalline diamond electrodes with Au nanoparticles. In this chapter, it will be also shown that the analysis used for the characterization of the diamond electrodes in chapter 6 can also resolve the heterogeneous characteristics of the microelectrode arrays or the electrodes decorated with metal particles.

As a comparison to diamond, the electrochemical properties of gallium nitride and indium nitride electrodes will be discussed in chapter 8. It will be shown that these electrodes are not stable under harsh anodic conditions, although III-nitride semiconductors are usually considered to be chemically inert. The stability against anodic oxidation is therefore one main advantage of diamond electrodes.

Chapter 2

Diamond for Electrochemical Sensing

2.1 Electrochemical properties of diamond

Apart from the exceptional electronic and mechanical properties like high electron and hole mobility (for intrinsic material), high electronic breakdown voltage, high mechanical fracture strength and high Young´s modulus [1, 2, 3, 4], diamond is also a very attractive material for electro- and biochemical applications [5]. Diamond is chemically inert and in the case of oxygen termination stable even under harsh oxidizing conditions, e.g. under anodic polarization or in oxidizing acids. Besides, the stability of diamond is not limited to aqueous electrolytes. As an example, it has been shown that diamond electrodes can be used in very corrosive molten alkali chloride electrolytes [6].

  Another important property which makes diamond interesting for electrochemical applications is its wide potential window of water dissociation with extremely low background currents compared to widely used metal electrodes like platinum or gold. Fig. 2.1 shows typical cyclic voltammetry measurements (which display the current across the electrode-electrolyte interface in dependence on the electrode potential) of a high-quality diamond and a platinum electrode. The potential window is limited by the hydrogen evolution reaction at negative (cathodic) potentials and the oxygen evolution reaction at positive (anodic) potentials. For platinum and other metals, the potential window is close to 1.23 V, which is the difference between the equilibrium potentials of both reactions [7]. For diamond, the potential window is typically in the range of 3.0 - 3.5 V, as it will be also shown later. The wide potential window of diamond in aqueous electrolytes is usually ascribed to the weak interaction of the diamond surface with molecules from the electrolyte. Therefore, reactions which require the adsorption of dissolved species are shifted to higher potentials [5, 8]. E.g., the hydrogen evolution reaction on hydrogen-terminated diamond can be described by the Volmer-Heyrovsky mech-
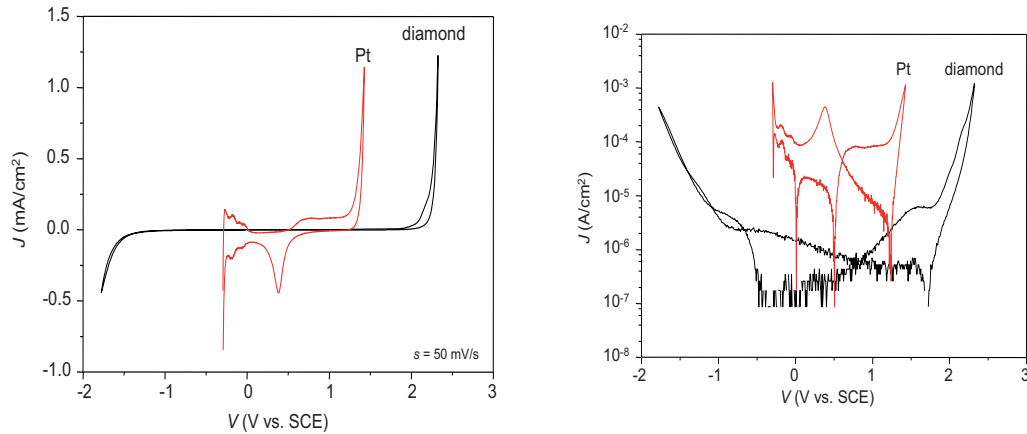
Figure 2.1: Typical cyclic voltammetry measurements of diamond and platinum in 0.1 M H_2SO_4. (a) linear scale, (b) semilogarithmic scale

anism [8, 9, 10], where a hydronium ion is discharged at a hydrogen site on the diamond surface:

$$C - H + H_3O^+ + e^- \rightarrow C \bullet + H_2 + H_2O \qquad (2.1)$$

This is the rate-determining step of the hydrogen evolution reaction. The diamond surface is then regenerated by the adsorption of another hydronium ion:

$$C \bullet + H_3O^+ + e^- \rightarrow C - H + H_2O \qquad (2.2)$$
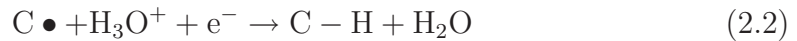
In these equations, C• depicts a reactive site on the diamond surface.

However, the diamond electrodes which are analyzed in this work are oxygen- and not hydrogen-terminated. It might be that the reaction proceeds again according to the Volmer-Heyrovski-mechanism, where the adsorption of the hydronium ions takes place at a C-OH or C=O site. Such a reaction mechanism has been proposed for metal oxide electrodes [11]. However, there are no detailed studies about the hydrogen evolution on oxygen-terminated diamond electrodes yet.

The mechanism of the oxygen evolution reaction on diamond proceeds most probably via several parallel reactions paths, which is the case even for metal electrodes [12]. Therefore, a detailed investigation is nearly impossible.

The wide potential window of diamond might enable the detection of charge-transfer reactions at high cathodic or anodic potentials outside the potential window of metal electrodes. However, this will be only the case for simple charge-transfer reactions which do not require a strong interaction of ions with the diamond surface, like the adsorption of reactants or intermediate products. Otherwise, also these reactions will be shifted to higher anodic potentials.

Another contribution to the *measured* potential window of diamond electrodes can be also the depletion layer close to the surface, which leads to an additional potential drop across the diamond. This is the case especially for low-doped electrodes.

The low background current, which is mainly determined by charging and decharging of the electrode interface, enables the detection of very small signals, which is important e.g. for biochemical measurements, where signals in the pA-range have to be resolved.

However, the potential window and the background current of diamond electrodes are very sensitive to the material quality. Low-quality diamond electrodes can contain a high amount of non-diamond (sp^2) contaminations. This leads to a decreased potential window and to higher background currents. In this case, the electrodes can be similar to glassy-carbon or graphite electrodes [5, 13, 14]. A similar effect has an extremely high boron doping concentration ($N_A \approx 5\times10^{21}$ cm^{-3} or more), which can lead to the formation of boron carbide clusters. Therefore, an optimization of the growth conditions is essential for the fabrication of diamond electrodes.

2.2 Diamond electrodes and ISFETs

The electrochemical applications of diamond can be divided into amperometric and potentiometric sensors. Amperometric sensors record a current across the diamond-electrolyte interface, which is related to the oxidation or reduction of the ions or molecules to be detected and therefore dependent on the concentration of this substance in the electrolyte. On the other hand, potentiometric sensors are based on the change of the surface potential in dependence on the electrolyte composition, e.g. the pH-value.

One example for amperometric sensing is the oxidation of organic compounds on diamond electrodes, which can be used for their detection. Examples are the detection of phenol [15, 16], carboxyl acids [17], ethanol, or other substances [18, 19]. As an example, the detection of ethanol on diamond electrodes will be shown in chapter 7. Besides, the anodic oxidation of such substances can be used for waste water treatment [16, 20], since the organic and maybe toxic compounds can be converted to non-toxic compounds. The stability of the diamond electrodes under high anodic potentials is an important condition for these applications.

Another widely studied application is the use of diamond for ion-sensitive FET (ISFET) structures, mainly for pH sensing. Such a device operates in the potentiometric mode, where the change in the surface potential due to the pH results in a change of the drain-source current of the ISFET. There are mainly three concepts for a pH sensor based on diamond: The most common one is the use of a partially hydrogen- and partially oxygen-terminated surface, where the hydrogen-

(a)   (b)
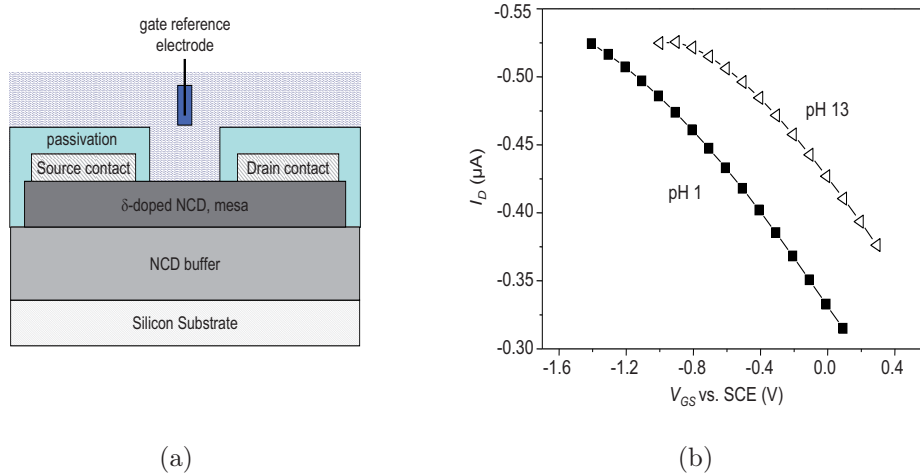
Figure 2.2: (a) scheme of an oxygen-terminated diamond ISFET with boron δ-doped channel, (b) transfer characteristics in pH = 1 and pH = 13 [23]

terminated areas induce the conducting channel and the oxygen-terminated areas the pH sensitivity [21]. A similar approach is the use of a partially aminated surface [22]. However, such devices suffer from instability, since the hydrogen termination can be converted to oxygen termination under anodic conditions, leading to a decrease of the channel conductivity. Therefore, the operation of such devices is limited to small drain-source and gate-source voltages and to non-oxidizing electrolytes. A better stability can be achieved using completely oxygen-terminated ISFET structures with boron-δ-doped channels [23, 24]. Such an ISFET structure on oxygen-terminated nanocrystalline diamond is shown in fig. 2.2(a). The drain-source current of a FET structure can be modulated by a gate voltage applied to a reference gate electrode which is immersed into the electrolyte. The pH sensitivity of the diamond surface results in a shift of the transfer characteristics with up to 59.2 mV/pH (fig. 2.2(b)).

The disadvantages of such FET structures are currently relative low current levels and a limited modulation of the channel. A third possibility is therefore the combination of an oxygen-terminated diamond electrode with a FET structure based on another material with better electronic properties, e.g. AlInN/GaN heterostructures [25].

Another field of growing interest is the use of diamond for biological applications, like attaching of DNA strands or proteins to the diamond surface [26, 27, 28], or cell measurements with patch-clamping systems [29] or quadrupole structures. Biochemical measurements can be done using electrode or FET structures. For such applications it is important that diamond is bio-compatible and optically transparent. Here it has to be noted that the optical transparancy is reduced by boron doping. However, the transparancy of the complete sample including a

transparent substrate, an intrinsic buffer layer and a boron-doped active layer is not significantly reduced as long as the thickness of the doped layer is in the range of a few hundred nanometers or below [30]. This promises to allow simultaneous electrochemical and fluorescence measurements. An attractive approach for this application is the growth of nanocrystalline diamond on optically transparent glass or sapphire substrates [30, 31, 32].

Chapter 3

Growth of Diamond Layers

In this chapter, the growth of single- and nanocrystalline diamond films will be described. Other aspects are the doping of diamond films and the role of the surface termination.

There are two main methods which were used to grow the diamond layers used within this work: The microwave plasma chemical vapor deposition (MWCVD) and the hot-filament chemical vapor deposition (HFCVD) technique. The diamond layers were grown at the Inst. of Electron Devices and Circuits (Ulm University). Details about the growth of diamond films like the influence of the various parameters on the growth are discussed in the references [33, 34, 35].

3.1 Diamond growth by CVD

Diamond films for electronic, electrochemical or other applications are usually grown by chemical vapor deposition (CVD). This growth technique usually operates at relative low pressure (in the kPa-range) and at high temperatures (>600 °C) and involves a carbon-containing gas like methane, and molecular hydrogen. The process gases are then dissociated into active carbon-hydrogen radicals and atomic hydrogen. The atomic hydrogen is required to etch sp^2-bonds on the surface and to stabilize the sp^3-bonds, which ensures the growth of diamond instead of graphite. The hydrogen also induces a hydrogen-termination of the diamond samples directly after the growth. The carbon-containing gas, whose concentration in the hydrogen is only in the range of a few percent or below, supplies the carbon atoms which are built into the crystal. The activation energy to crack the molecules into radicals can be supplied by temperature (hot filament CVD) or by plasma (microwave plasma CVD).

Until now, single-crystal CVD diamond is usually grown on diamond stones fabricated by the high-pressure high-temperature (HPHT) method [36]. However, the growth on HPHT stones reduces the available size of the diamond samples to approx. 5×5 mm². Therefore, the growth of single-crystal diamond on for-

eign substrates like iridium [37] is currently investigated. On the other hand, the growth of poly- and nanocrystalline diamond is possible on large-area foreign substrates, like silicon, glas, or metals. The main requirements for such a foreign substrate are the formation of a carbide layer and the substrate stability under atomic hydrogen atmosphere and under the growth temperature. Another important factor for the growth of diamond layers on foreign substrates is the formation of diamond nuclei with a sufficient density as starting points for the growth. One method is the bias-enhanced nucleation (BEN), where the surface of the carbon-forming substrate is bombarded with carbon ions by applying a negative bias to the conductive sample [33].

3.1.1   Hot-filament CVD

The hot filament CVD technique was used for the growth of the nanocrystalline diamond electrodes studied in this thesis. The hot-filament CVD (HFCVD) is based on thermal decomposition of the methane and hydrogen molecules in order to generate free radicals for the growth process [33, 38]. The cracking of the molecule bonds occurs at filaments which are heated to a temperature of 2000-2200 °C.

Fig. 3.1 shows the chamber used to grow the nanocrystalline diamond layers used in this work on silicon substrates. The machine consists basically of a

(a)   (b)
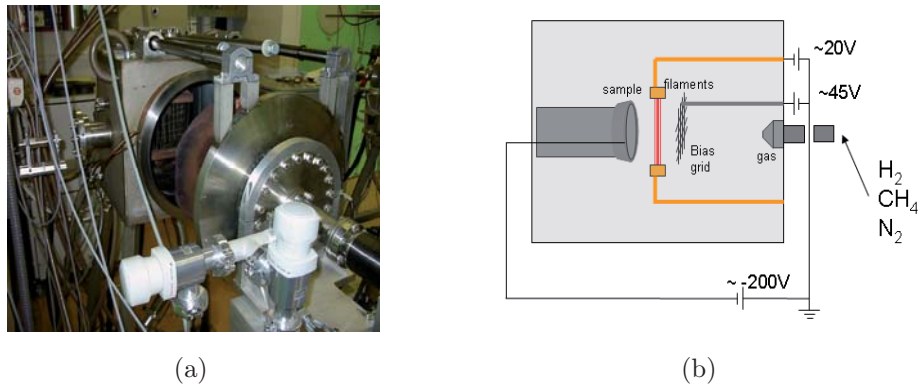
Figure 3.1: (a): photograph of the HFCVD reactor, (b): sketch [33, 38]

substrate holder, the filaments and the windows for the gas fluxes. The distance between the substrate and the filaments was typically 5-10 mm. The substrate is held vertically to prevent the deposition of contamination on the surface. The filaments are typically made of tungsten or tantalum, which have melting points higher than 2300 °C and do not react with atomic hydrogen. Boron doping is achieved using a liquid source of trimethyl borate (TMB). Hydrogen gas is used as a carrier for the TMB molecules. Typical process parameters were a substrate
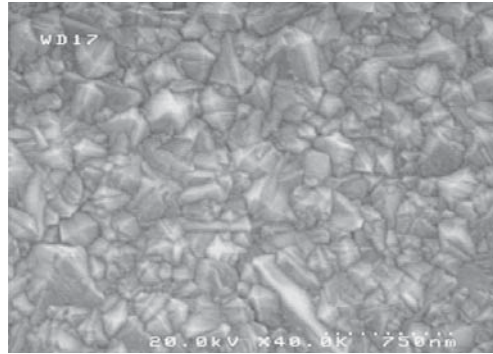
Figure 3.2: SEM image of a typical NCD electrode grown by HFCVD

temperature of 750 °C, a pressure of 2 kPa, and gas fluxes of 400 sccm, 2 sccm, and 4 sccm for hydrogen, methane and TMB/hydrogen, respectively.
The main advantage of HFCVD compared to the MWCVD used in this work is the availability of the large-area growth of diamond (in our case up to 4´´ diametre). However, HFCVD films might contain metal contaminations from the filaments. An SEM image of such a typical nanocrytsalline diamond electrode is shown in fig. 3.2.

3.1.2 Microwave plasma CVD

Microwave plasma CVD was used to grow the single-crystal diamond layers used in this work. In the MWCVD process, the radicals required for diamond growth are generated by electric discharge [33, 39]. Fig. 3.3(b) schematically shows the ASTeX microwave-plasma CVD system used for the growth of the single-crystal electrodes. The films were grown on commercially available HPHT substrates, as mentioned before. The microwave power was coupled into the chamber via a quartz window. The dimensions of the chamber and the waveguide were chosen so that only one microwave mode was possible, thus creating a plasma ball in the center of the chamber.
Boron doping was achieved by inserting a boron rod into the plasma, where the length of this inserted rod determined the doping concentration. Typical growth parameters were a RF power in the range of 700 W, a pressure of 4 kPa, a substrate temperature of 700 °C, and gas fluxes of 200 sccm and 3 sccm for hydrogen and methane, respectively. The main advantages of MWCVD compared to HFCVD are less contamination of the samples and a higher reproducibility. A disadvantage of the MWCVD machine used in this work was the limited size of the plasma ball. Therefore, large-area growth like in HFCVD was not possible. In addition, non-diamond substrates or metal interlayers can be etched in the hydrogen plasma or atmosphere, which limits the choice of the substrate.

(a) (b)
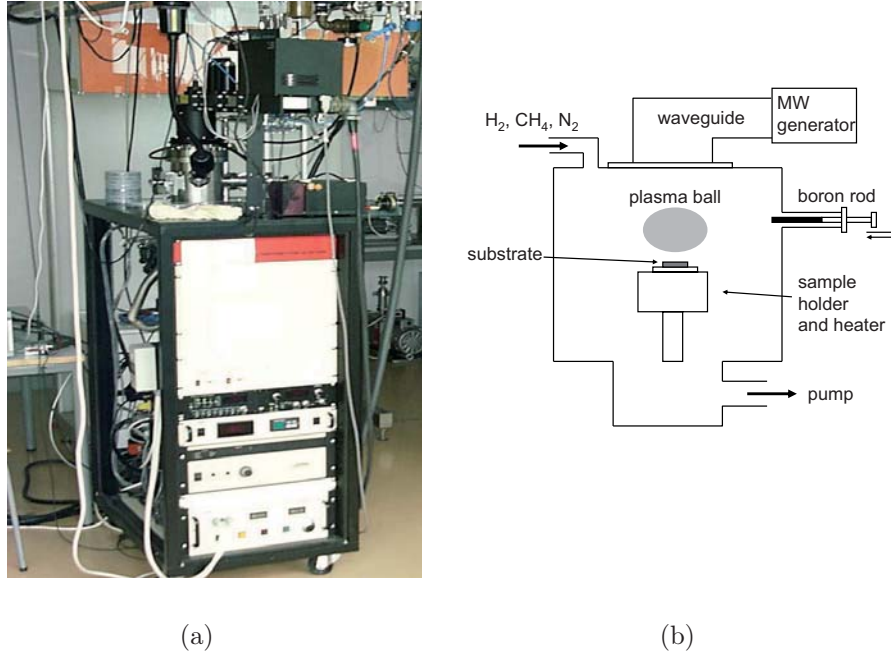
Figure 3.3: (a): photograph of the MWCVD reactor, (b): sketch [39]

3.2 Doping of diamond

One important and critical aspect is the doping of diamond, since there are no shallow donors or acceptors. The standard acceptor in diamond is boron, which has an activation energy of $E_a = 0.37$ eV for low doping concentrations. This activation energy is still much higher than the thermal energy at room temperature. However, the activation energy of boron acceptors in diamond is dependent on the concentration, as shown in Fig. 3.4. For $N_A > 1 \times 10^{20}$ cm^{-3}, the activation energy becomes very low, leading to full activation of the acceptors at room temperature [40, 41, 42]. Therefore, diamond electrodes are usually highly boron-doped. In addition, oxygen termination of diamond leads to a depletion layer on the surface, which might block any signal current across the interface. Therefore, a high dopíng concentration in the range of 10^{20} cm^{-3} or above is needed to provide significant tunnelling across this depletion layer, since the depletion layer thickness decreases into the range of a few nanometer. In the case of a metal-semiconductor junction, the tunnelling current is dependent on the doping concentration according to the following equations [43]:

$$J \propto \exp\left(\frac{-q\phi_B}{E_0}\right) \tag{3.1}$$

$$E_0 = \frac{qh}{4\pi} \times \sqrt{\frac{N_A}{\epsilon_0 \epsilon_r m^*}} \tag{3.2}$$

In these equations, q is the elementary charge, ϕ_B the barrier height, N_A the doping concentration, m^* the effective mass, $h = 4.14 \times 10^{15}$ eVs the Planck constant, ϵ_0 the dielectric constant and ϵ_r the permittivity of diamond. The equations show that the tunnelling current increases exponentially with $\sqrt{N_A}$.
However, the high doping concentration might lead to mechanical stress and the formation of boron clusters. In the case of nanocrystalline diamond, boron is accumulated at grain boundaries [44], which leads to non-uniform doping and might also limit the chemical stability of the electrodes. For FET strucures, the required high doping concentration also leads to another challenge: For a significant modulation of the channel, the thickness of the boron-doped layer should be approx. 2 nm or below (δ-profiles) [4].
N-type doping in diamond is even more complex than p-type doping. Phosphorous with an activation energy $E_a = 0.62$ eV and nitrogen with $E_a = 1.7$ eV are deep donors [45], with an activation energy which is not significantly reduced with higher doping concentration. This is the reason why n-doped diamond electrodes are only rarely investigated.
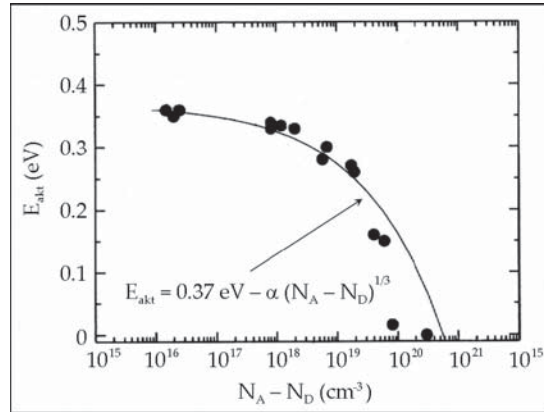
Figure 3.4: Activation energy of boron in diamond as a function of the effective acceptor concentration [42]. The experímental data are from [40, 41]

3.3 Surface terminations of diamond

Hydrogen termination

One important aspect of diamond is its surface termination. Directly after growth, the diamond surface is hydrogen-terminated due to a hydrogen-rich atmosphere in the growth reactor. The hydrogen termination can be converted into oxygen- , chlorine- or fluorine termination by chemical, plasma or thermal treatments. All these surface terminations have different characteristics. Therefore, the control of the surface termination is an essential aspect.

Hydrogen-terminated diamond is used for the fabrication of diamond-based FETs [3, 46], since it can avoid the problem of the lack of shallow donors. When the hydrogen-terminated diamond surface is exposed to air (or to electrolytes), a hole channel with a carrier density in the range of 10^{13} cm^{-2} is formed close to the surface even for undoped diamond. Besides, hydrogen termination results in an unpinned surface potential, which makes ohmic as well as Schottky contacts possible, depending on the work function of the contact metal. The presence of the hole channel close to the surface has been explained by the C-H dipoles at the diamond surface, which lead to a negative electron affinity, and by a charge transfer between diamond and molecules adsorbed from the atmosphere or from electrolytes [47]. However, there are still open questions concerning the mechanism of the hydrogen-induced surface conductivity. For example, the hole channel seems to be not located directly on the diamond surface, but a few nanometers underneath, as extracted from the analysis of FET structures [48]. The structure might therefore resemble the case of an AlGaN/GaN heterostructure.

One of the main drawbacks of hydrogen-terminated diamond based electronic or electrochemical devices is that the channel close to the surface vanishes when the hydrogen termination is converted into e.g. oxygen termination, thus limiting the stability of these devices. One solution in the FET technology could be a gentil surface passivation, e.g. by atomic layer deposition of aluminum oxide, which does not destroy the surface conductivity [48]. For electrochemical applications, the use of hydrogen-terminated diamond is limited to low potentials and non-oxidizing media.

Oxygen termination

On the other hand, the oxygen termination of diamond is thermally and chemically very stable. Therefore, the fabrication of electronic devices on oxygen-terminated diamond using δ-profiles could be also promising for high-power applications [49]. In the case of oxygen terminated diamond, the Fermi level at the surface is mostly pinned at approx 1.7 eV above the top of the valence band [50, 51], leading to a depletion of the surface for boron-doped diamond.

Here it is important to note that there is a variety of possible carbon-oxygen groups on oxygen-terminated diamond, which will result in different bond strengths and therefore to different electronic and electrochemical properties. The analysis of this issue is one main part of this work.

Fluorine and other terminations

Other possible surface terminations of diamond are the fluorine and the chlorine termination, where fluorine-terminated diamond could be very useful for some electro- or biochemical applications [52, 53]. Fluorine-terminated diamond seems to be much more stable against oxidation than hydrogen-terminated diamond. However, the characteristics of these surfaces are still under research. E.g., data about the surface band bending on fully fluorine-terminated diamond are still missing. One problem is here that most fluorine-terminated electrodes investigated in literature still contain a significant amount of oxygen on the surface [52, 54], which might mask the characteristics of the fluorine termination.

Chapter 4

Electrochemical Surface Analysis

4.1 The semiconductor-electrolyte interface

4.1.1 The electrochemical potential scale

In electrochemistry, electrode potentials are usually referred to the potential of a reference electrode, since the potential difference between the electrode under test and the bulk electrolyte cannot be directly measured. The electrode which has been chosen to be the reference point of the electrochemical potential scale is the normal hydrogen electrode NHE (also standard hydrogen electrode, SHE). This electrode consists of a platinum sheet which is immersed into an acidic solution with the proton concentration of 1 mol/l (pH = 0), which is purged with hydrogen gas of $p = 1$ atm. The potential-determining reaction is the hydrogen evolution reaction $2H^+ + 2e^- \rightleftharpoons H_2$. The potential is linked to the test electrolyte via a porous frit [7].
However, the standard hydrogen electrode is rarely used in practical cases, because it requires e.g. a defined gas supply. Instead, other reference electrodes are used. All electrochemical measurements shown in this work were performed using a saturated calomel electrode (SCE), which is based on the reduction of mercury ions to elemental mercury in a saturated potassium chloride electrolyte [7]. The SCE has an electrode potential of $+242$ mV vs. NHE (see fig. 4.1).
The electrochemical potential scale can be related to the physical energy scale, as shown in fig. 4.1. In the electronic energy scale, the vacuum level is used as the reference. The vacuum level in the electronic energy scale corresponds to an electrode potential of -4.44 V vs. NHE [5, 47, 55]. Besides, a shift to more positive energies in the electronic scale correlates with a negative shift in the electrochemical potential scale and vice versa. For a p-type semiconductor like boron-doped diamond, negative (cathodic) potentials correspond to depletion and positive (anodic) potentials to accumulation at the surface. For a n-type semiconductor like Si-doped GaN, the opposite trend applies.
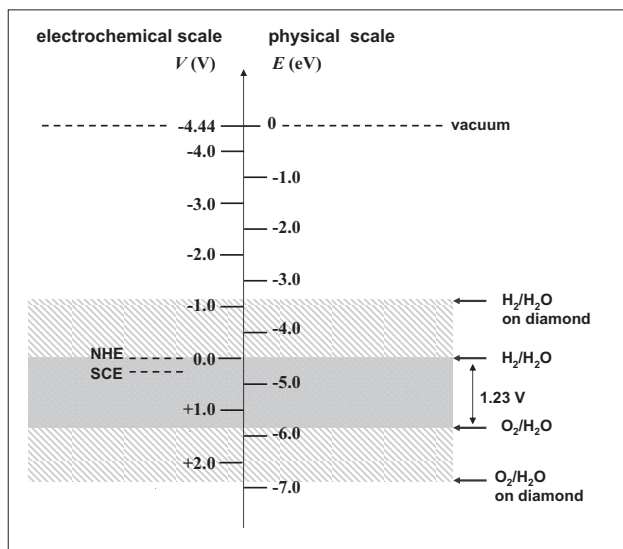
Figure 4.1: Electrochemical potential scale versus electronic energy scale

4.1.2   The electrochemical double layer

The junction between a metal or semiconductor and an electrolyte generally does not form an ohmic contact. The reason is that the electrolyte is an ionic conductor and the metal or semiconductor an electron (or hole) conductor. In the absence of charge transfer reactions, the interface will have blocking characteristics.

When a metal or a semiconductor is in contact with an aqueous electrolyte, the Fermi level in the semiconductor and the electrochemical potential in electrolyte will tend to align. In the case of oxygen-terminated diamond, this will give rise to a depletion layer in the semiconductor, similar to the case of metal Schottky contacts on the same material. The countercharge corresponding to the charge within the depletion layer (and the charge of ionized electronic surface states) will be formed by solvated ions from the electrolyte, which will be attracted to the surface by electrostatic forces (non-specific adsorption) and approach the surface to a distance of half their diameter (see fig. 4.2), which is approx. 0.3 nm [56]. The layer between the electrode surface and the plane of adsorbed ions is called electrochemical double layer or Helmholtz layer, the plane through the centers of these ions is the outer Helmholtz plane (OHP). It can be modeled by an additional plate capacitor in series to the depletion layer capacitance, where the "plates" of the double layer capacitance are formed by the electrode surface and the plane across the charge centers of the adsorbed solvated ions. The corresponding value for the capacitance can be calculated if the dielectric constant of the interfacial water layer is known. While the permittivity of water is usually in the range of
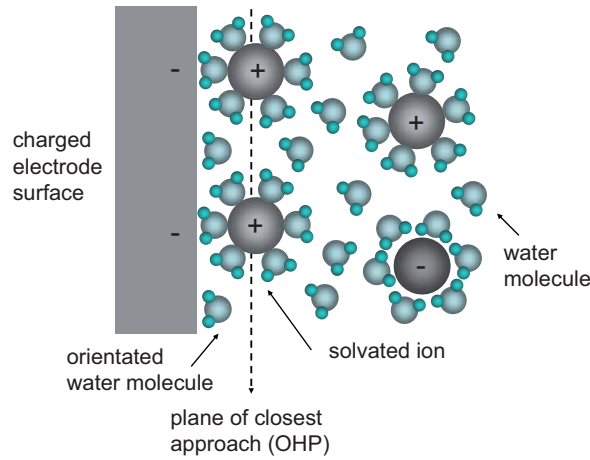
Figure 4.2: Sketch of the electrochemical double layer, assuming no specific adsorption

80, the value within the electrochemical double layer is much smaller, typically in the range of 5-10 [56]. The reason is that the water dipoles are preferentially orientated due to the high electric field within the double layer, thus loosing a degree of freedom. Typical values for the double layer capacitances of oxygen-terminated diamond electrodes are in the range of 10-20 $\mu F/cm^2$ [57, 58]. Here it should be noted that the extraction of the double layer capacitance is often difficult because the depletion layer capacitance usually dominates the impedance characteristics of the interface.

Apart from non-specific adsorption, ions with weakly bounded solvation shells (especially halide ions like Cl^{2-}) may become de-solvated and chemically adsorbed (specific adsorption) to the surface. The plane across the centers of these ions is called the inner Helmholtz plane. This can lead to a potential "overshooting" since more charge is accumulated at the surface than required by electrostatics [56]. Such effects will however not be discussed in this work since they were not detected or studied in detail.

4.1.3 The pH sensitivity of oxygen-terminated diamond

As already mentioned in chapter 2, the carbon-oxygen surface groups of oxygen-terminated diamond are sensitive to the pH value of the electrolyte. This sensitivity results in a parallel shift of the transfer characteristics of ISFET devices (see fig. 2.2(b)). The same shift can also be observed in open circuit potential measurements and in the flatband potential extracted from Mott-Schottky plots, as

it will be shown later. The pH sensitivity is usually explained by the site-binding model, in analogy with metal oxides or oxidized GaN surfaces [59, 60, 61]. This model is based on the amphoteric character of surface hydroxyl groups. The hydroxyl groups can attach or release protons:

$$C - OH + H_3O^+ \rightarrow C - OH_2^+ + H_2O \tag{4.1}$$

$$C - OH + OH^- \rightarrow C - O^- + H_2O \tag{4.2}$$
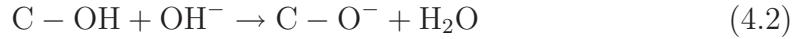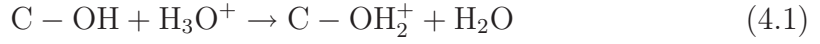
The net surface charge and the surface potential are dependent on the concentration of H_3O^+ and OH^- ions and therefore on the pH value of the electrolyte. However, the pH sensitivity is not limited to the presence of hydroxyl groups on the surface. As it will be shown in chapter 5, there are also ether, carbonyl and other carbon-oxygen groups present on the diamond surface. It is most likely that also these functionalities contribute to the pH sensitivity.

The theoretical value of the pH sensitivity is given by the Nernst equation [7]

$$\Delta V_s = -\frac{k_B T}{q} \ln\left(\frac{c_{H_3O^+}}{c_0}\right) = 2.303 \frac{k_B T}{q} \times pH \tag{4.3}$$

where $c_{H_3O^+}$ is the concentration of hydrogen (hydronium) ions, c_0 the reference hydrogen concentration 1 M, q the elemental charge, k_B the Boltzmann constant and T the temperature. This gives a maximum pH sensitivity of the surface potential of 59.2 mV/pH at 300 K.

4.1.4 Charge-transfer reactions on diamond electrodes

The occurence of charge transfer reactions on diamond electrodes depends on the characteristics of the diamond bulk and the electrochemical surface characterisitcs. As discussed in section 3.2, the oxygen-termination of diamond leads to a depletion layer on its surface, which might supress any charge transfer across the semiconductor-electrolyte interface. This can be prevented by a high boron doping concentration, which ensures tunnelling across the depletion layer.

On the electrolyte side, the charge transfer can also be described by a potential barrier, which is related to the difference in the solvation shells of the reduced and oxidized ions [7]. By applying an external potential to the electrode, this barrier can be lowered or increased, leading to a net cathodic or anodic current. This leads to an exponential dependence of the current on the electrode potential. The current-potential characterisitcs for a simple electron-transfer process without specific adsorption can be expressed by the Butler-Volmer equation [7]

$$J = J_0 \times \left[\exp\left(\frac{(1-\alpha)zF}{R_gT}(V - V_0) \right) - \exp\left(\frac{-\alpha zF}{R_gT}(V - V_0) \right) \right] \qquad (4.4)$$

where J_0 is the exchange current density which is a measure of the reaction kinetics, $\alpha = 0...1$ the transfer coefficient, z the number of exchanged electrons, F = 96485 C/mol the Faraday constant, R_g the gas constant, and V_0 the equilibrium potential of the reaction, where the net current is zero. For overpotentials $(V - V_0)$ » 26 mV, one of the exponential terms dominates, which leads to a characteristic similar to that of a diode in forward direction.

4.2 Electrode preparation and experimental setup

The diamond films for the electrode measurements were grown by MWCVD (single-crystal diamond) or HFCVD (nanocrystalline diamond), as shown in chapter 3. After growth, the samples were exposed to surface oxidation treatments, which will be discussed in detail in the following chapter.

Figure 4.3: Photographs of NCD electrodes after contacting with silver paste (down) and after passivation with a Teflon-based adhesive tape (top)

The diamond samples were mounted on a conductive copper holder and contacted with silver paste. Then, the samples were passivated using a Teflon-based adhesive tape with a perforated opening of typically 1 mm in diameter. This opening determined the active electrode area in contact to the electrolyte. After the measurements, the tape could be removed and the sample cleaned. Therefore, this measurement method was non-destructive. Fig. 4.3 shows two nanocrystalline diamond electrodes.
The electrochemical measurements were performed in a three-electrode glass cell which is shown by the photograph in Fig. 4.4(a). Three different electrolytes

(a)   (b)
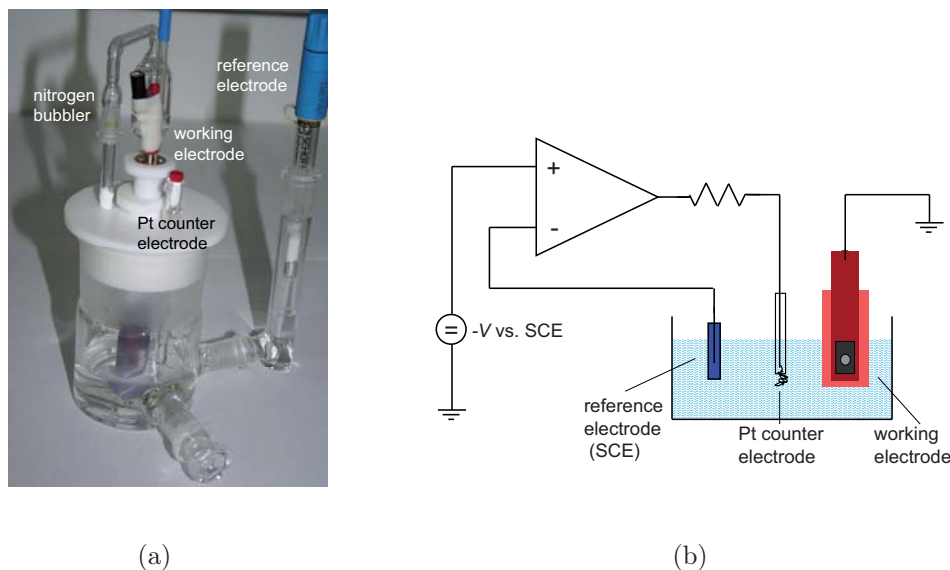
Figure 4.4: (a)Three-electrode glass cell, (b) schematic realization of the potentiostat used for the measurements.

were used: 0.1 M H_2SO_4 (pH $\approx$ 1), 0.1 M KCl (pH $\approx$ 7), and 0.1 M KOH (pH $\approx$ 13).

In the electrochemical measurements, the current across the surface of the electrode under test (the working electrode) or the impedance of the electrode-electrolyte interface is measured as a function of the electrode potential by applying an external voltage versus a platinum counter electrode. As described above, the electrode potentials are recorded against an electrode used as reference, e.g. a saturated calomel electrode. In a simple two-electrode setup consisting of working and counter electrode, the potential of the electrode under test would not be known since there is also a potential drop across the interface of the platinum electrode and the electrolyte. This potential drop may change during the measurement, when a current flows across the interface of the counter electrode. Therefore, three-electrode systems controlled by a potentiostat are usually used for electrochemical measurements. The simplified realization of a potentiostat is shown in fig. 4.4(b). The operational amplifier ensures that the potential between the electrode under test (working electrode) and the reference electrode is equal to the required value and that there is no current across the reference electrode. All electrochemical experiments were performed in a Faraday cage in the dark. The electrolyte was typically purged with nitrogen gas prior to the measurements to remove dissolved oxygen from the solution.

4.3   Characterization in simple electrolytes

In the following section, the electrochemical characterization techniques used in this work are presented. Typically, the first step was to measure the open-circuit potential of the diamond electrode. Then, cyclic voltammetry measurements in simple electrolytes without redox systems were performed to determine the potential window of water dissociation, the background current within the window, possible adsorption processes and the hydrogen- and oxygen evolution characteristics. This technique was also used to study electrochemical reactions on diamond electrodes, like the oxidation of ethanol (see chapter 7).

Electrochemical impedance spectroscopy measurements were used to extract an equivalent electrical circuit modeling the electrode-electrolyte interface. The boron doping concentration, the flatband potential in contact to the electrolyte and therefore the electronic surface barrier could be extracted from impedance measurements at various potentials or by capacitance-voltage measurements in electrolyte.

4.3.1   Open circuit potential measurements
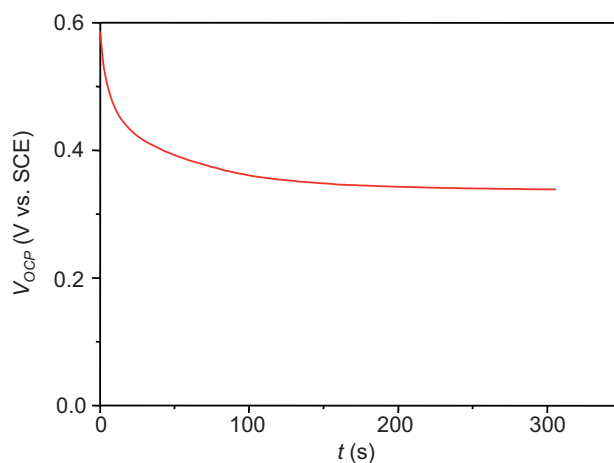
Figure 4.5: Typical OCP measurement of a diamond electrode in 0.1 M H_2SO_4

The open circuit potential (OCP) measurement determines the electrode potential measured versus the reference electrode. Therefore, it gives the position of the Fermi level in the diamond material in contact to the electrolyte. The open-circuit potential can be measured with a voltmeter with a high internal resistance, which was provided by the used potentiostat.

The open-circuit potential of an electrode is dependent on the electrolyte. In the case of oxygen-terminated diamond, the OCP value in simple electrolytes without any redox couples is determined by the equilibrium between the the hydrogen and oxygen evolution reactions (see fig. 4.1). The potentials corresponding to these reactions and therefore also the values for the open circuit potential depend on the pH of the electrolyte.

After immersing the electrode into the electrolyte, it took typically up to approx. 15 minutes to reach a constant value for the open-circuit potential. As an example, fig. 4.5 shows an OCP measurement of a diamond electrode in 0.1 M H_2SO_4. In addition, previously taken measurements under non-equilibrium conditions (e.g. impedance spectroscopy at a fixed electrode potential or cyclic voltammetry) could influence this measurement and lead to an incorrect OCP value. Because of this, open circuit potential measurements were usually recorded before all other experiments were an external potential was applied to the electrode.

4.3.2   Cyclic voltammetry measurements

Cyclic voltammetry measurements are current-potential measurements of the electrode-electrolyte interface, where the electrode potential is continuously changed between two vertex potentials with a constant scan rate s $= \mathrm{d}V/\mathrm{d}t$, as shown in the insert of fig. 4.6. Usually, the vertex potentials are chosen to be close to the onsets of hydrogen- and oxygen evolution.

Cyclic voltammetry is a standard method in electrochemistry to study adsorption or charge transfer reactions on well-known and ideal electrodes, e.g. high-quality gold or platinum electrodes [56]. However, this measurement technique can also be used to characterize the electrode in a well-known and simple electrolyte. In this work, cyclic voltammetry measurements were mostly performed in aqueous electrolytes without any redox couples to investigate the characteristics of the diamond electrodes in terms of potential window, background current and oxygen evolution characteristics.

A typical cyclic voltammetry measurement of a diamond electrode in 0.1 M H_2SO_4 ($pH \approx 1$) is shown in Fig. 4.6. The arrows and the figure in the insert show the scan direction. All cyclic voltammetry measurements shown in this work were performed at a scan rate of 50 mV/s and after several previous cycles (to reach a steady state), if not noted differently. The voltamogram is shown here in the $\mu A/cm^2$-range to resolve also features at low currents.

As mentioned before, one advantage of using diamond for electrochemical applications is the wide potential window of approx. 3 V (for currents in the $\mu A/cm^2$-range) between the hydrogen oxygen evolutions, which is significantly larger than the potential window of 1.23-1.5 V for metal electrodes. As mentioned before, the origin of this wide potential window is most likely associated with the weak interaction of intermediate products and the diamond surface due to the low density of active sites [5, 8]. The onset potentials for the hydrogen- and oxygen
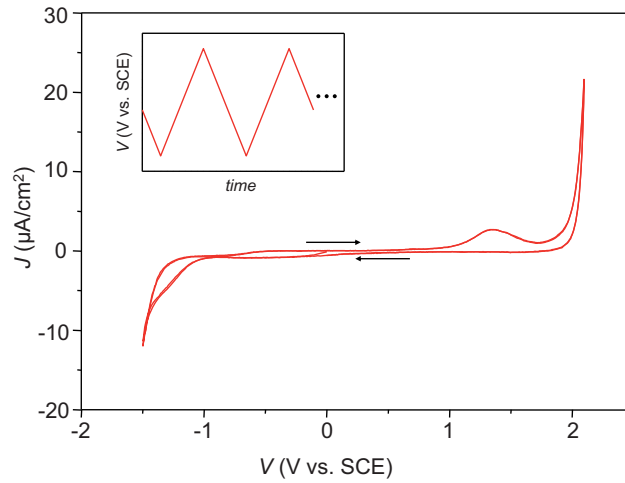
Figure 4.6: Typical cyclic voltammetry plot of a boron-doped diamond electrode in 0.1 M H_2SO_4

evolution in pH = 1 and the theoretical values are also shown in Fig. 4.1. For higher pH values, the potentials are shifted with 59 mV/pH to more negative values. Therefore, the cyclic voltammetry plots of diamond in electrolytes with different pH are in the ideal case shifted compared to pH = 1.

Within the potential window of water dissociation, the current is dominated by charging and de-charging the electrode-electrolyte interface capacitances. However, diamond electrodes of low quality can show an increased current due to some parasitic activity, which can be induced by grain boundaries, defects or non-diamond components [13].

Besides, highly boron-doped diamond electrodes typically show a small current peak prior to the onset of the oxygen evolution (see Fig. 4.6), which might be ascribed to the adsorption or desorption of ions which are accumulated on the surface during the hydrogen- and oxygen evolution reaction. This aspect will be analyzed in chapter 6 in detail.

4.3.3   Electrochemical impedance spectroscopy

In impedance spectroscopy measurements, the frequency-dependent impedance of the electrode-electrolyte interface is measured at a constant electrode potential. This is done by the superimposition of the DC potential with an AC small-signal (amplitude typically 10-20 mV) of variable frequency. Using the measured data, the diamond-electrolyte interface can be characterized by an equivalent electronic
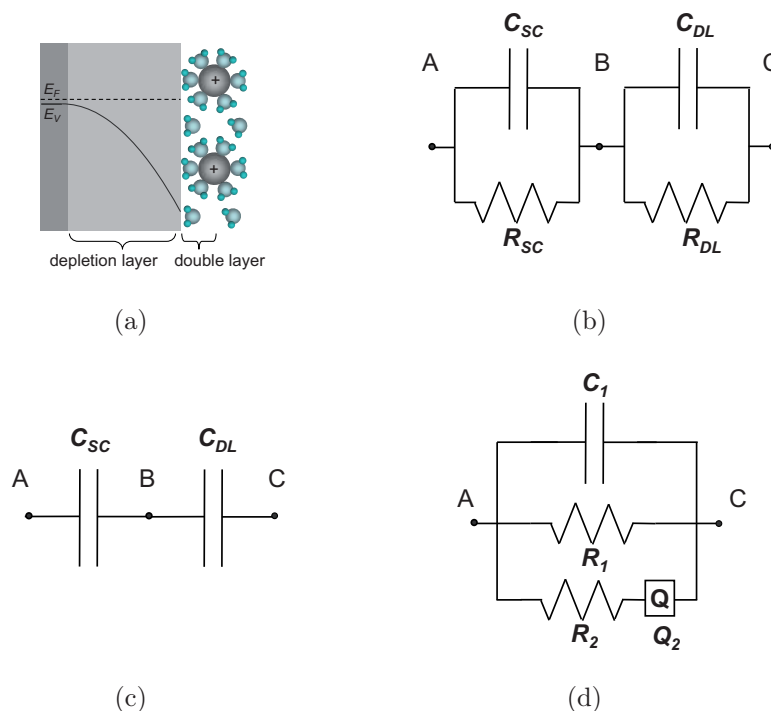
Figure 4.7: (a) Schematic structure of the electrode-electrolyte interface, (b) Equivalent circuit with depletion and double layer capacitances, (c) simplified circuit in the absence of charge transfer or adsorption processes, (d) equivalent circuit in the range of adsorption. C_{SC} and R_{SC} denote capacitance and resistance of the depletion (space charge) layer, C_{DL} and R_{DL} correspond to the double layer. C_1, R_1, R_2 could be a combination of elements related to depletion- and double layer, R_2 and Q_2 are related to adsorption processes.

circuit where the single elements can in the ideal case be ascribed to double- or depletion layer, charge transfer reactions, or adsorption processes.

As shown in section 4.1.2, the diamond-electrolyte interface can be described by the depletion layer in the semiconductor and the double layer in the electrolyte. Therefore, a plausible equivalent circuit contains two RC-circuits related to depletion- and double layer, respectively (plus a series resistance related to the ohmic contacts and the electrolyte), as shown in Fig. 4.7(b). The resistances in parallel to the capacitances describe a possible charge-transfer across the interface. In the case of simple electrolytes without any charge transfer reactions within the potential window, the parallel resistances can typically be neglected, leading to the simplified equivalent circuit in fig. 4.7(c).

However, the depletion- and double layer capacitances are often non-ideal and therefore frequency-dependent due to slow processes within the depletion- and double layer or due to surface inhomogeneities [58, 62, 63]. In this case, the ca-

pacitance is replaced by a constant phase element (CPE). The impedance of a constant phase element is given by

$$Z_Q = \frac{1}{(j\omega)^n \cdot Q_0} \tag{4.5}$$

where $\omega = 2\pi f$ is the circular frequency and Q_0 and n are parameters. For $n = 1$, the CPE is equal to an ideal capacitance with $C = Q_0$, which is often called the nominal capacitance. For $n = 0$, the CPE would be a resistor with $R = 1/Q_0$. Typical measured values of n related to the depletion- or double layer capacitance were between 0.93 and 0.99 (see chapter 6). A low value of n can give additional information about the electrode characterisitcs, as it will be shown in chapter 6 e.g. for the case of plasma treatments.

In the case of charge transfer reactions or adsorption processes on the electrode surface, the simplified equivalent circuit shown in fig. 4.7(c) is not valid any more. An example is the potential range prior to the onset of the oxygen evolution reaction, where an adsorption peak can be observed in cyclic voltammetry measurements (see fig. 4.6). Such processes can be usually not described by a RQ parallel resistance alone, but by more complex eqivalent circuits. A model which was often used in this case (see discussion in chapter 6) is shown in fig. 4.7(d). The capacitance C_1 could be ascribed to the depletion layer, the double layer, or a series connection of both elements. The n-value of the CPE Q_2 was typically around 0.6, which close to the ideal value of a Warburg element ($n = 0.5$). A Warburg impedance characterizes diffusion-limited processes [64]. The equivalent circuit in fig. 4.7(d) with the CPE replaced by a Warburg element can also often be used to study redox reactions on diamond electrodes [65].

There are different ways to display and to analyze the data of impedance spectroscopy measurements. The most common representations are Bode plots (absolute value and phase of the impedance vs. frequency), Nyqvist plots (imaginary vs. real part of the impedance) and capacitance plots (imaginary vs. real part of the complex capacitance or complex dielectric constant [64]). The complex capacitance $\underline{C}$ is defined in analogy to the impedance of a "real" capacitance:

$$\underline{C} = \frac{1}{(j\omega \cdot \underline{Z})} \tag{4.6}$$

The capacitance plot is often useful because it is sensitive at small frequencies. The Nyqvist plot is often used when redox couples are investigated, because a Warburg element can be detected in this plot by a 45° slope at low frequencies [64].

A method similar to impedance spectroscopy are capacitance-voltage measurements. In capacitance-voltage measurements, the potential-dependent

interface capacitance is measured at a constant frequency. To be more exact, this measurement also records a complex impedance, from which the capacitance can be calculated using an equivalent circuit. This equivalent circuit could be e.g. extracted from previous impedance spectroscopy measurements. Capacitance-voltage measurements have been widely used to extract the doping concentration, doping profile, and flatband potentials of diamond electrodes [23, 58, 63, 66, 67, 68]. However, in many studies no detailed analysis by impedance spectroscopy measurements was performed. This is often necessary when the same equivalent circuit is not valid for the total potential range to distinguish between depletion- and double layer capacitance, adsorption-related contributions, or charge-transfer reactions. An alternative is therefore to perform impedance spectroscopy measurements at various potentials, which was done in this work.

4.4   Evaluation of the electronic surface barrier

(a)   (b)
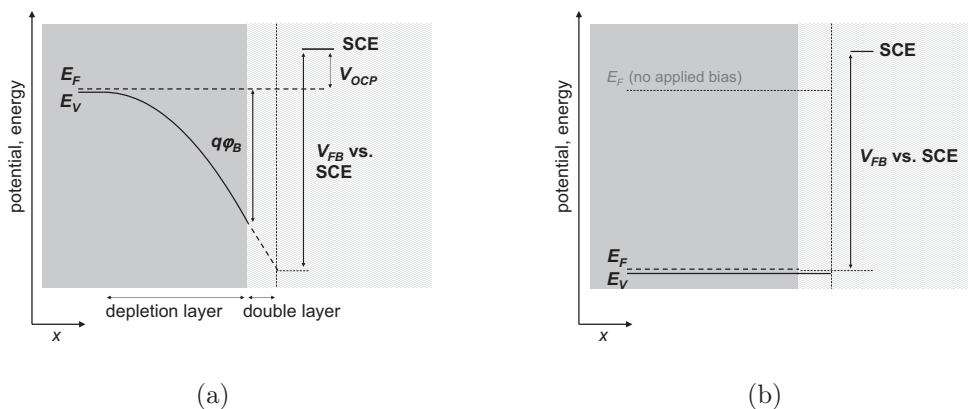
Figure 4.8: Band diagram of the diamond-electrolyte interface. (a) no applied bias, (b) at flatband conditions

Fig. 4.8(a) and 4.8(b) show schematic band diagrams of the diamond-electrolyte interface under no bias and at flatband conditions, respectively. The surface barrier $q\phi_B$ could be extracted from capacitance-voltage or impedance spectroscopy measurements at various potentials, and from OCP measurements. The corresponding evaluation method will be shown in the following. The impedance measurements were mostly recorded at potentials within the window of water dissoziation, where the simplified equivalent circuit shown in fig. 4.7(c) can fit the experimental data.

The applied potential with respect to the flatband potential partially drops across the depletion (nodes A-B in fig. 4.7(b) and 4.7(c)) and the double layer (B-C). For potentials within the potential window, it is very difficult to resolve depletion- and double layer capacitance seperately and often only the total capacitance can be extracted. However, the double-layer capacitance can be taken to potential-independent in first approximation. The value of the double-layer capacitance can be extracted from the saturation value for the total capacitance at high anodic potentials corresponding to flatband conditions.

For a p-type semiconductor, the depletion layer (space-charge layer) capacitance C_{SC} can be calculated to [43]:

$$C_{SC} = \frac{q\varepsilon_0\varepsilon_r N_A}{\sqrt{\left[2 \times \left(\Phi_{SC} + \frac{k_B T}{q}\right)\right]}} \tag{4.7}$$

where Φ_{SC} is the potential drop across the depletion layer, ε_0 the dielectric constant, ε_r the permittivity of diamond, N_A the acceptor concentration and $k_B T/q$ the thermal voltage of 26 mV at room temperature. To fit the measured capacitance data for the overall capacitance and to extract the electronic surface barrier, a MOS-like model was applied. For a constant double-layer capacitance, the Mott-Schottky plot ($1/C^2$ vs. the potential) showing the *overall* capacitance and the *overall* potential drop is still linear with a slope corresponding to the doping concentration, but an extrapolated intercept with the V-axis which is shifted to higher potentials [69], similar to MOS-contacts at depletion. The total capacitance C of the diamond-electrolyte interface can be calculated when the double-layer capacitance C_{DL} is known:

$$C = \frac{C_{SC} \times C_{DL}}{C_{SC} + C_{DL}} \tag{4.8}$$

The applied potential difference with respect to flatband conditions partially drops across the electrochemical double layer (Φ_{DL}). Therefore, the electrode potential V measured versus the reference electrode is:

$$V = V_{FB} - \Phi_{SC} - \Phi_{DL} = V_{FB} - \Phi_{SC} \times \left(1 + \frac{C_{SC}}{C_{DL}}\right) \tag{4.9}$$

The extraction of the surface barrier with no applied bias was done by fitting the measured data with the equations 4.7 to 4.9, where N_A and V_{FB} are the fit parameters. The electronic surface barrier under no applied bias is the potential drop across the depletion layer which corresponds to an electrode potential equal to the measured value of the open-circuit potential V_{OCP}:

$$q\varphi_B = \Phi_{SC} \mid_{V=V_{OCP}} \tag{4.10}$$

The analysis was done for measurements in all three different electrolytes (0.1 M H_2SO_4, 0.1 M KCl, 0.1 M KOH). For a pinned surface potential which should be expected for oxygen-terminated diamond, measurements in electrolytes with different pH-values should result in the same electronic surface barrier, although the values for the open-circuit potential and the flatband potential (or the intercept of the Mott-Schottky plot with the V-axis) are pH-dependent.

4.5   Redox reactions on electrodes

In the previous discussion of cyclic voltammetry measurements only simple electrolytes without any redox systems within the potential window of water dissociation were considered. In this case, the (capacitive) background current, depending on the scan rate, is very small.
This situation changes in the presence of redox couples. Well-known examples are the $Fe^{2+/3+}$ and the $Fe(CN)_6^{3-/4-}$ redox couples, which involve the transfer of one electron between the ions in the electrolyte and the electrode.
In the following, redox reactions on two types of electrode surfaces will be considered. The typical case is a large-area (planar) electrode without any surface structures. However, it will be shown that microelectrodes have attractive characteristics which are useful for electrochemical analysis. The fabrication and characterization of a microelectrode array embedded into a large-area passive electrode will be shown in chapter 7.

4.5.1   Linear diffusion on planar (large-area) electrodes

Fig. 4.9 shows a typical cyclic voltammetry measurement of a planar diamond electrode in an electrolyte containing the $Fe(CN)_6^{3-/4-}$ redox couple, which is often used to study the characteristics of diamond electrodes because of its sensitivity to the surface termination [5]. In the following, the oxidation peak (anodic currents) will be discussed. The oxidation of the reduced species close to the electrode surface starts at a potential of approx. $+0.14$ V vs. SCE, which is the reversible potential of the $Fe(CN)_6^{3-/4-}$ redox couple. At low overpotentials, the reaction current increases exponentially according to the Butler-Volmer equation (see section 4.1.4). However, the oxidation leads to a decrease of the concentration of reduced ions at the electrode surface. Therefore, the diffusion of reduced ions from the bulk solution to the electrode surface becomes rate-determining, which leads to saturation and a subsequent decrease of the current with time and therefore with overpotential (since potential and time are correlated by the scan rate). The decrease of the current can be understood like in the following:
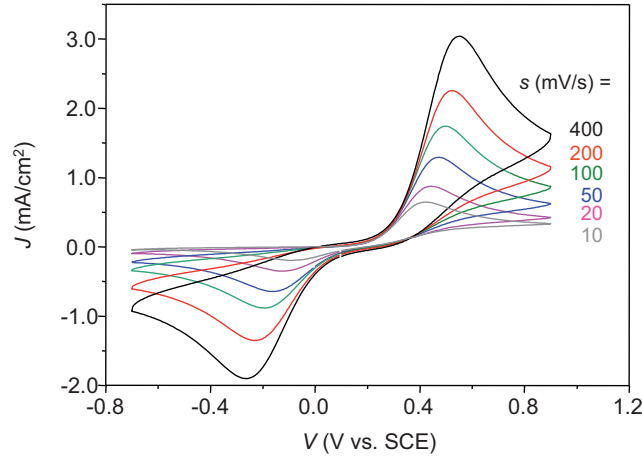
Figure 4.9: Typical cyclic voltammetry measurement for an oxygen-terminated diamond electrode in 0.1 M KCl containing 10 mM $K_4Fe(CN)_6$

For a fast reaction, the concentration of reduced species at the electrode surface will be zero, since all reduced ions will be directly oxidized. The time-dependent concentration profile (for the case of a switch-on potential step) can be calculated to [7]:

$$c(x, t) = c_b \times \text{erf}\left(\frac{x}{\sqrt{4Dt}}\right) \tag{4.11}$$

The calculated profiles after time scales between 1 ms and 10 s for a diffusion constant of the ions $D = 6.1 \times 10^{-6}$ cm^2/s and a bulk concentration of $c_b = 10$ mM are shown in fig. 4.10. It can be clearly seen that the diffusion layer (the layer which is depleted from reduced ions) penetrates into bulk electrolyte and that the concentration gradient at the surface, which dominates the diffusion-limited current, decreases with time. The time-dependent current density can be calculated to [7]

$$j = nFc_b \times \sqrt{\frac{D}{\pi \cdot t}} \tag{4.12}$$

This equation also implies that the peak current related to a redox reaction on a planar electrode is scan-rate dependent, because a faster scan rate correlates with a smaller measurement time:
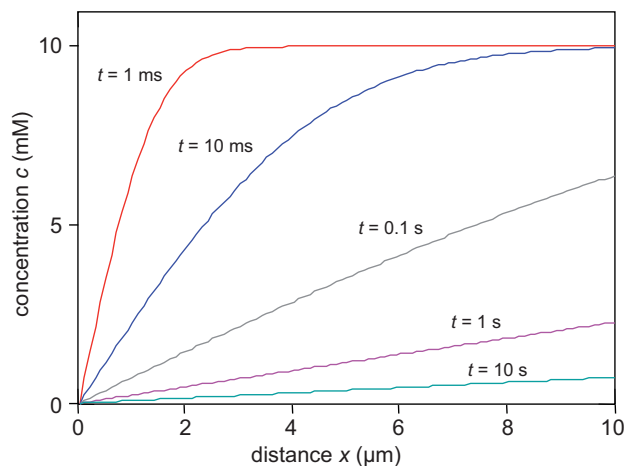
Figure 4.10: Calculated profiles for linear diffusion after different times between 1 ms and 10 s.

$$j_{peak} \propto \sqrt{s} \tag{4.13}$$

The scan rate dependence can be seen in fig. 4.9.

The diffusion limitation on planar electrodes leads to several disadvantages: It limits the signal current density, makes static measurements difficult, and makes it necessary to measure at the peak potential, which might be shifted with scan rate and ion concentration. These disadvantages lead to the idea of microelectrodes.

4.5.2 Hemispherical diffusion on microelectrodes

If the geometry of a single microelectrode is in the same range or smaller than the extension of the diffusion layer, the diffusion planes become hemispherical. In this case, the outer parts of the diffusion layer are depleted more slowly compared to the case of planar diffusion, resulting in a concentration gradient at the surface which does not decrease significantly with time. By solving the diffusion equation in spherical coordinates [7], the time-dependent diffusion profile can be calculated to:

$$c(r,t) = c_b \times \left[1 - \frac{r_0}{r} \operatorname{erfc} \left(\frac{r - r_0}{\sqrt{4Dt}} \right) \right] \tag{4.14}$$
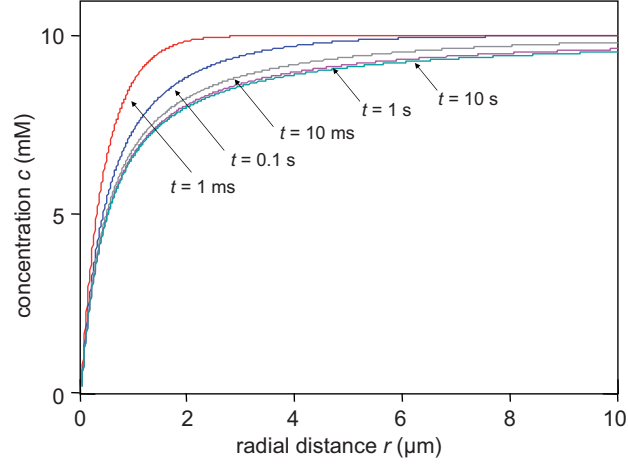
Figure 4.11: Calculated profiles for hemispherical diffusion after different times between 1 ms and 10 s. The chosen parameters are the same like in fig. 4.10.

where r is the radial distance from the center of the microelectrode, r_0 the radius of the microelectrode, and D again the diffusion constant. The concentration profile after elapsed times between 1 ms and 10 s are shown in fig. 4.11. The calculation was performed for $r_0 = 0.25 \ \mu$m (which is the value for the fabricated sub-microelectrode array shown in chapter 7) with the same value for bulk concentration and diffusion constant as for the case of the planar electrode (see fig. 4.11). The current density calculated by the concentration gradient at $r = r_0$ becomes:

$$j = nFDc_b \times \left(\frac{1}{\sqrt{\pi Dt}} + \frac{1}{r_0} \right) \qquad (4.15)$$
.

The first term in the bracket in equation 4.15 is related to the plamar contribution, the second one to the spherical contribution. In these equations, r_0 is the radius of a single microelectrode with spherical shape and r is the radial distance from its center. For large r_0 corresponding to a planar electrode, the current density is again proportional to $1/\sqrt{t}$. For small r_0, the current density becomes time-independent:

$$j = \frac{nFDc_0}{r_0} \qquad (4.16)$$

This shows that high signal current densities can be reached when the dimensions of the microelectrode are reduced below $\sqrt{\pi D t}$, which is the diffusion length of the redox system. Typically, the dimensions of a single microelectrode must be below 20-50 μm [70]. However, further decreasing leads to an improved current density, which makes the fabrication of sub- microelectrodes or nanoelectrodes attractive. In such cases, it is possible to increase the current density compared to planar electrodes by more than one order of magnitude.

4.5.3   Microelectrode arrays

(a)   (b)
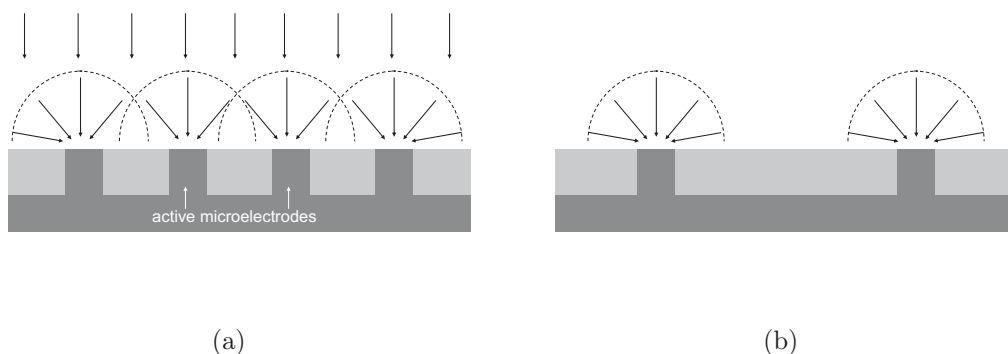
Figure 4.12: Microelectrode arrays with two different distances between adjacent microelectrodes. (a) small distance: overlapping of the diffusion planes and linear diffusion, (b): sufficiently large distance and microelectrode behavior.

One disadvantage of using a single microelectrode is the small absolute current due to the small active surface area. To increase the active surface area, arrays of microelectrodes are used. However, care must be taken when designing the microelectrode array dimensions. This can be understood by fig. 4.12(a) and 4.12(b), where two arrays with different distances between two adjacent microelectrodes are shown. If the distance between two microelectrodes is sufficiently large, there is no interaction between the diffusion planes of the adjacent microelectrodes, and hemispherical diffusion dominates. However, if the distance between two microelectrodes is in the same range as the extension of the diffusion layer, the diffusion layers overlap, which results again in planar diffusion. The minimum distance between two adjacent microelectrodes to maintain spherical diffusion has been calculated e.g. in ref. [70] to be at least 10-15 times higher than the diameter of a single microelectrode.

Chapter 5

Surface Oxidation of Diamond

Directly after growth, the diamond surface is usually hydrogen-terminated, since the samples are grown in a hydrogen-rich atmosphere. Although also hydrogen-terminated diamond is used in electrochemistry, harsh environment applications like waste water treatment or pH sensing in strong bases and acids require an oxygen-terminated surface. There is a variety of possible carbon-oxygen groups which are possible on the diamond surface, like hydroxyl (C-OH), carbonyl (C=O), or ether (C-O-C) groups. These oxygen functionalities differ in the bond strength and are therefore expected to differ also in electronic and electrochemical characteristics.

A way to control the carbon-oxygen functional groups is the choice of the surface oxidation treatment. In this work, four different oxidation methods are investigated: Wet-chemical oxidation in $H_2SO_4:H_2O_2$, anodic oxidation in KOH, RF oxygen plasma, and argon/oxygen plasma. The latter treatment is not preferentially used for the oxygen termination of diamond, but is used as an etching process in diamond technology. These four surface treatments will be discussed in detail in the following section. Other possible oxidation methods are thermal treatment in oxygen atmosphere [51] or UV irradiation in air [71].

The different oxidation treatments will be analyzed by atomic force microscopy to determine the effect of the oxidation on the surface roughness and by X-ray photoemission spectroscopy to identify the carbon-oxygen groups and the amount of defects induced by the plasma process.

5.1 Surface oxidation treatments

5.1.1 Wet-chemical oxidation

The wet-chemical oxidation treatment used in this work consists of two steps: First, the diamond samples are subjected to chrome sulfuric acid ($H_2SO_4 : CrO_3$) at a temperature of approx. 80 °C. This treatment is used to remove all graphitic

components from the surface [24, 63]. Alternative methods could be treatments in $H_2SO_4 : KNO_3$ [72] or $H_2SO_4 : NaNO_3$ [58]. After the treatment in chrome sulfuric acid, the diamond samples were cleaned in de-ionized water to remove possible chromic components from the surface and subjected to $H_2SO_4 : H_2O_2$ at approx. 100 °C for a complete oxygen termination.

This oxidation treatment is very useful for electrodes or other applications where a complete diamond surface has to be oxidized. In addition, this surface treatment does not require a conducting surface or any ohmic contacts, like in the case of anodic oxidation. However, it is difficult to apply this method for the local oxidation of diamond surfaces because this requires a mask which is stable in such acidic solutions.

5.1.2 Anodic oxidation

Anodic oxidation is an electrochemical process, where the surface is oxidized by oxygen radicals generated from hydroxyl ions by an externally applied potential. The applied potential corresponds to the range of the oxygen evolution reaction. In this work, the anodic oxidation was performed in 0.1 M KOH electrolyte at a constant potential of +1.8 or +2.0 V vs. SCE, which is above the onset of the oxygen evolution reaction in this solution (see insert of fig. 5.1). The initial current density was typically in the range of 1 mA/cm^2 and decreased until a constant value related to the oxygen evolution reaction was reached. This decrease of the current can be explained by a reorganization of the carbon-oxygen surface groups and the formation of a chemisorbed surface layer, which will be shown in section 5.3 by the X-ray photoemission spectroscopy (XPS) measurements. An example for the anodic oxidation is shown in fig. 5.1. The amount of transferred charge during oxidation after a process time of approx. two minutes was typically approx. 20 mC/cm^2, corresponding to 10^{17} electrons/cm^2. Taking into account the number of surface bonds of approx. 10^{15} cm^{-2}, the complete surface is expected to be oxidized, which was verified by XPS analysis (see below). Here it should be noted that a significant amount of the transferred charge is related to the oxygen evolution and not the surface oxidation. After such oxidation process, a further anodic treatment with similar parameters did not induce any additional changes in the electrochemical characteristics. There was also no difference between wet-chemically oxidized and "as-grown" (hydrogen-terminated) electrodes after they were subjected to the anodic oxidation process.

As shown for NCD electrodes, the anodic oxidation also removes graphitic components from the surface, similar to the wet-chemical oxidation treatment [73, 74]. It is therefore an attractive oxidation method for diamond electrodes.

However, the anodic oxidation process requires ohmic contacts to the surface to be oxidized. It can therefore not be used for the oxidation of non-conducting surfaces. Another disadvantage is that local oxidation is difficult, since it requires local ohmic contacts as well as a stable mask.
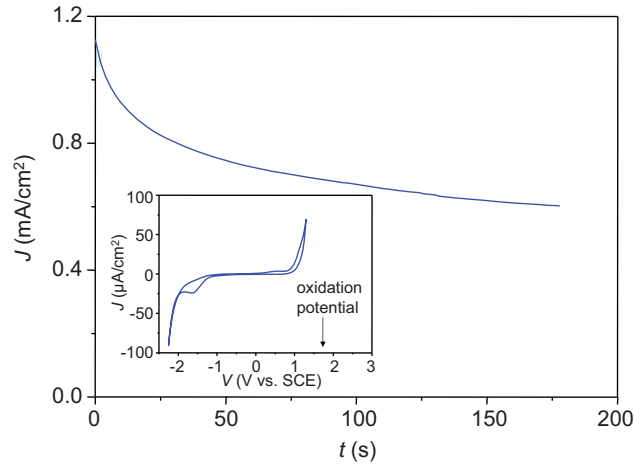
Figure 5.1: Current-time characteristics of an anodic oxidation treatment. Oxidation parameters: $V = +1.8$ V vs. SCE, $Q/q \approx 2 \times 10^{17}$ cm^{-2}

5.1.3 Oxidation by plasma treatments

Plasma treatments are widely used in diamond technology, because they do not require a special sample preparation (e. g. the deposition of ohmic contacts like in the case of anodic oxidation), and local treatment is possible using masks fabricated by lithography. In the case of the plasma treatments discussed here, a photoresist mask was sufficiently stable for process times at least up to 30 minutes. Plasma treatments are also widely used for the functionalization of diamond electrodes by oxygen, fluorine, or chlorine [52, 75, 73]. This section will focus on two different oxygen plasma processes.

In principle, two cases of oxygen plasma treatments can be distinguished: A plasma process in pure oxygen atmosphere without any DC bias, resulting in first approximation in a pure chemical treatment, and an etching process like in argon/oxygen plasma, which includes physical etching (sputtering).

In a plasma process, the process gases are dissociated by a high-frequency electric field applied between two electrodes, resulting in a plasma containing free electrons, positively charged ions and active radicals. The AC signal is coupled into the plasma reactor via one of the electrodes, while the second electrode is grounded. During the plasma process, the electrode which is not grounded will be negatively charged due to the bombardment with electrons during the positive half-wave of the AC signal, resulting in a DC self-bias up to the kV-range [76]. If the sample is mounted on this negatively charged electrode, it will be bombarded with the positively charged ions.

RF oxygen plasma

Fig. 5.2 shows a sketch of the barrel reactor for the oxygen plasma process. In this process, the diamond samples were placed on the grounded electrodes, while the RF power was coupled into the chamber via the opposite electrode. Therefore, the diamond sample was in first approximation exposed only to a chemical treatment by oxygen radicals diffusing to the surface, but not to physical bombardment by oxygen ions. The RF oxygen plasma process was performed for two minutes at a
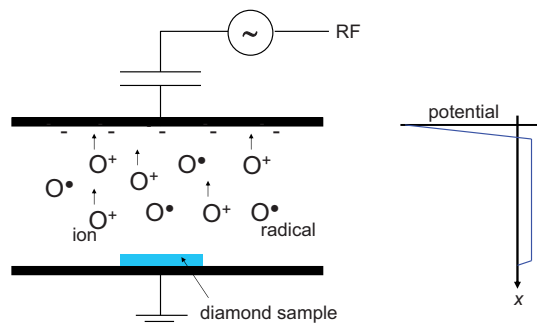
Figure 5.2: Sketch of the barrel reactor for oxygen plasma

pressure of 100 mTorr and a RF power of 100 W at room temperature. The gas flux of oxygen was 7.5 sccm. This process results in a low etching rate of approx. 0.2 nm/min.

The RF plasma oxidation was usually performed on diamond electrodes which had been previously oxidized by wet-chemical or anodic treatment. Diamond electrodes which were exposed to the plasma process directly after growth showed very similar characteristics.

Reactive ion etching in argon/oxygen plasma

The second plasma process investigated was reactive ion etching (RIE) in argon-oxygen plasma. This process involved chemical etching as well as physical sputtering, the latter mainly due to the argon content in the process gas. This plasma treatment has been used in the FET technology [49] as well as for the fabrication of microelectrode array structures [77].

The setup is schematically shown in fig. 5.3. In this case, the sample was mounted on the charged electrode. The process was performed at 50 mTorr, 25 W, and with gas fluxes for argon and oxygen of 17.6 sccm and 1.76 sccm, respectively.
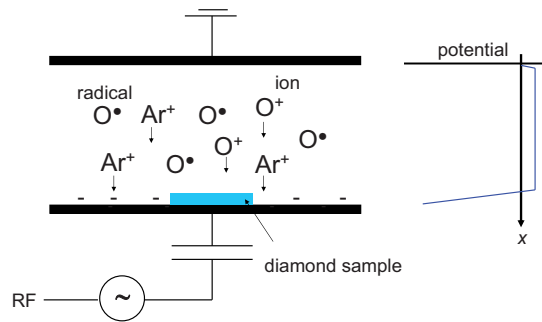
Figure 5.3: Sketch of the reactor for reactive ion-etching in argon/oxygen plasma

The measured etching rate was approx. 2.5 nm/min. Therefore, any previous surface termination will be replaced by this treatment.

After the etching process, the samples were exposed to the wet-chemical treatment described above to remove graphitic components created by the ion bombardment. The main characteristics of the electrodes exposed to the argon/oxygen plasma were not significantly affected by this post-treatment.

5.2 Surface profiling by AFM

Single-crystal (100)-orientated diamond samples with a surface roughness below 1 nm RMS (root mean square value) were characterized after each oxidation treatment by atomic force microscopy (AFM) measurements. The results are shown in fig. 5.4(a)-5.4(c). The treatment by RF oxygen plasma had a small effect on the surface topology. The RMS value increased slightly from 0.4 nm to 0.46 nm, which becomes more noticable in the cross-sections in fig. 5.4(d) and 5.4(e). On the other hand, a stronger increase of the surface roughness could be expected for the argon/oxygen plasma treatment, which has an etching rate of approximately 2.5 nm/min. However, the opposite trend was found: The RMS value slightly decreased to approx. 0.3 nm. Besides, no preferential etching at some local points was observed. In summary, the plasma treatments have only a minor effect on the surface roughness of the diamond films.

AFM measurements of nanocrystalline diamond films were also recorded. They showed again no significant difference in the surface roughness and no preferential etching, e.g. of grain boundaries. However, the surface roughness was in the range of 30-50 nm (RMS), which would make the detection of small changes after the relative short plasma processes impossible.
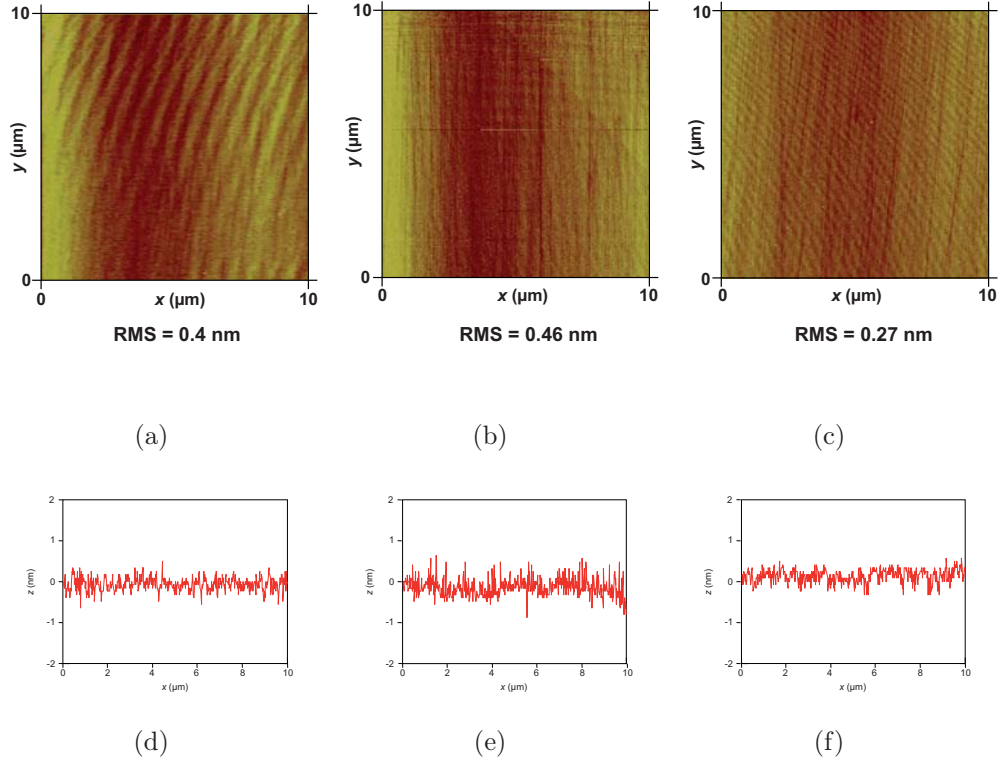
Figure 5.4: AFM images of a SCD sample after (a, d) wet-chemical, (b, e) RF oxygen plasma and (c, f) argon/oxygen plasma treatment

5.3 Surface analysis by angle-resolved XPS

5.3.1 Introduction

The carbon-oxygen surface functional groups induced by the different oxidation treatments were analyzed by X-ray photoemission spectroscopy (XPS). XPS spectra are recorded by irradiating the surface of the material under test with X-rays and by the analysis of the kinetic energy of the photoelectrons, which are released from the inner atom shells of the material (see fig. 5.5). From the measured kinetic energies, the binding energies E_b can be calculated:

$$E_b = h\nu - E_{kin} - \Phi_{det} \tag{5.1}$$

where $h\nu$ is the photon energy and Φ_{det} the work function of the detector. The binding energy spectrum gives information about the chemical composition close
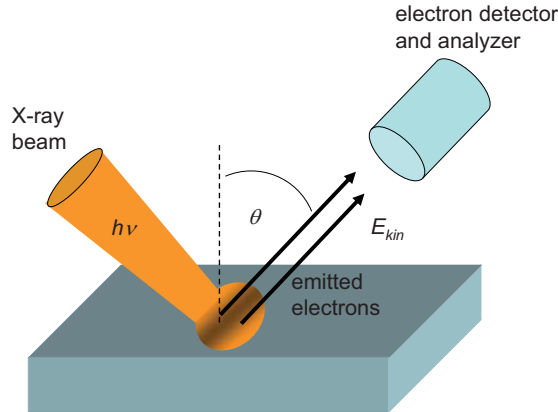
Figure 5.5: Sketch of the setup for XPS measurements

to the surface of the sample under test. The material parameter which determines the depth which can be analyzed is the escape length λ of the photoelectrons, which is approx. 2.2 nm for diamond and the Al Kα radiation source. In first approximation, the top layer with a thickness of approx. 3λ contributes to the detected signal.

A typical XPS survey scan for oxygen-terminated diamond is shown in fig. 5.6. It shows two peaks which are located at approx. 284.0 eV and 532 eV binding energy. These two peaks can be attributed to the C1s and the O1s core level, respectively. Both peaks contain signals from the surafce and the surface-near bulk region. Using high-resolution XPS, these two peaks can be deconvoluted into several peaks located at slightly different binding energies corresponding to different carbon-oxygen groups and (in the case of the C1s peak) to sp^2 and sp^3 phases. The reason is that the binding energy of the inner-shell electrons depends also slightly on the binding state of the valence electrons in the outer shell (chemical shift).

To distinguish signals from the surface and from the (surface-near) bulk, angle-resolved XPS measurements can be used. For a low detection angle, the layer of approx. 3λ contributes to the signal. For higher detection angles (see fig. 5.5), this information depth is reduced by a factor of $\cos\theta$. In the case of a substrate covered by a fractional overlayer, the signals I_A from the overlayer and I_B the bulk B can be calculated by the following [78]:

$$I_A = \beta_A I_{A0} \times \left[1 - \exp\left(-\frac{d_A}{\lambda \cos\theta} \right) \right] \qquad (5.2)$$
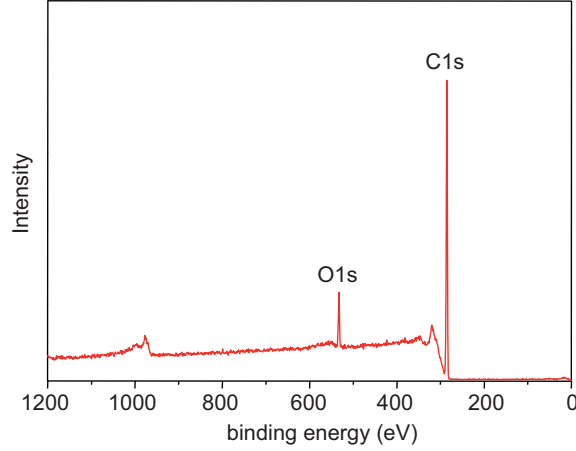
Figure 5.6: XPS spectrum of oxygen-terminated diamond (survey scan)

$$I_B = I_{B0} \times \left[1 - \beta_A + \beta_A \exp\left(-\frac{d_A}{\lambda \cos \theta} \right) \right] \tag{5.3}$$

where I_{A0} and I_{B0} are the maximum intensities at $\theta = 0°$, d_A the thickness of the overlayer, and β_A the coverage of the surface with A. For the case of oxygen-terminated diamond, the bulk signal is expected to originate from sp^3 bonds, while the surface layer is composed of carbon-oxygen groups and possibly sp^2-like defects. The maximum intensities I_{A0} and I_{B0} are in this case the same since both layers consist of a carbon material.

The photoelectron spectroscopy measurements shown in this work were performed and analyzed by A. Romanyuk (Inst. of Physics, University of Basel) and A. Denisenko (Inst. of Electron Devices and Circuits, University of Ulm). The measurements were done with a VG ESCALAB 210 system equipped with a monochromatic Al Kα (1486.6 eV) source at a base pressure of 1×10^{-9} mbar. The XPS measurements of the C1s and the O1s core level were performed at different detection angles between 0° (perpendicular to the surface) and 80° to determine the surface coverage with carbon-oxygen functionalities and the thickness of the modified surface layer. The resolution was approx. 0.2 eV. All XPS measurements were done on single-crystal (100)-orientated diamond samples.

5.3.2 Wet-chemically oxidized surface

The C1s (fig. 5.7(a)) core level spectrum after wet-chemical oxidation could be deconvoluted into three different peaks. The main peak at 284.0 eV is related to the sp^3 bulk signal. The peak at 284.9 eV can be associated with hydroxyl (C-OH) or ether (C-O-C) groups, which are hard to be distinguished in the C1s core level spectrum because they correspond to almost the same binding energy. The small signal at lower binding energy (282.6 eV) could be related to a slight amount of sp^2-like components which are still present on the surface. However, the contribution of this signal was with approx. 1 % within the range of the detection limit. In the O1s core level spectrum, peaks at 530.8 eV, 532.2

(a)   (b)
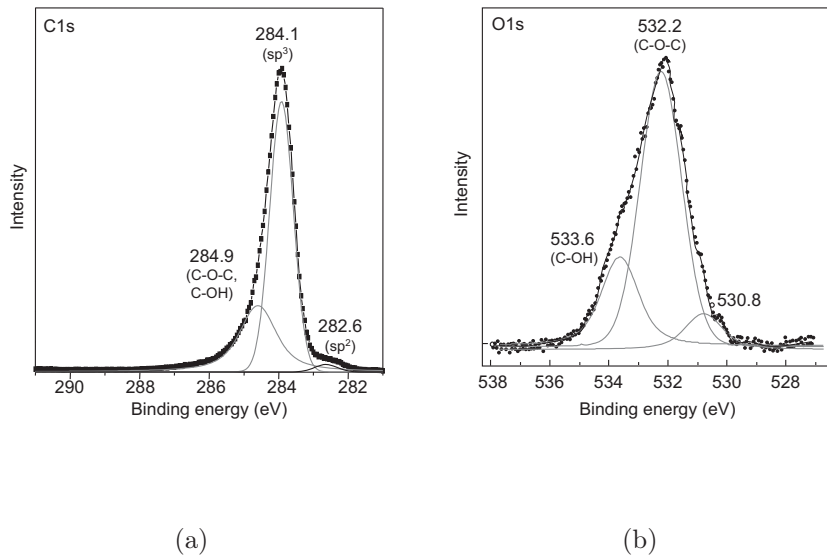
Figure 5.7: (a) C1s and (b) O1s core level spectra of single-crystal diamond after wet-chemical oxidation

eV and 533.6 eV were detected. The peak at 533.6 eV can be related to C-OH functionalities, the peak at 532.2 eV binding energy to ether (C-O-C) groups. The origin of the third peak remains unclear yet. Analyzing the C1s data measured at different scan angles (see fig. 5.8) with equations 5.2 and 5.3, the surface coverage with carbon-oxygen groups was calculated to be close to 100 % or slightly lower. The calculated thickness of this modified layer was 0.22 nm, compared to 0.356 nm for the lattice constant of diamond [79] and approx. 0.1 nm for the carbon layer separation in (100) direction. Therefore, it can be concluded that one or nearly one monolayer has been oxidized by the wet-chemical treatment.
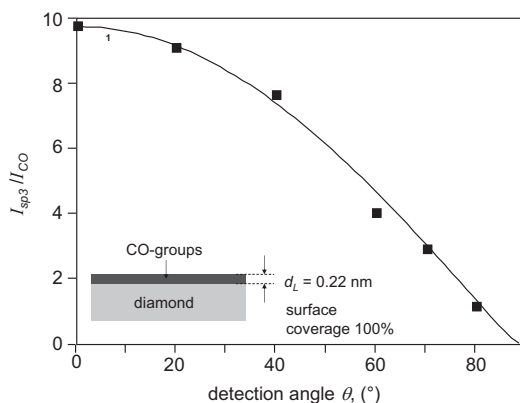
Figure 5.8: Analysis of the C1s peak for the case of wet-chemical oxidation at different detection angles. I_{sp3} is the intensity of the sp^3 bulk signal, I_{CO} the sum of the signals related to the different carbon-oxygen groups.

5.3.3 Anodically oxidized surface

The C1s and O1s core level spectra after anodic oxidation (fig. 5.9(a) and 5.9(b)) differed significantly from that after wet-chemical treatment. The intensity of component at 284.9 eV, which was ascribed to a combination of C-OH and C-O-C groups, was increased compared to the case of wet-chemical oxidation. On the other hand, the signal in the O1s spectrum at 533.6 eV vanished nearly completely. Since this component was related to C-OH groups, it can be concluded that the anodic oxidation leads to an increased amount of C-O-C groups, but not to C-OH functionalities. The anodic oxidation generated also more complex carbon-oxygen groups (denoted by "C-O-X"), possibly polycarbonate groups, as detected in the C1s spectrum by the additional peak at approx. 288 eV. However, more detailed information about these functionalities could not be resolved. The anodic treatment performed in this work did not induce a significant amount of carbonyl groups (C=O). Such carbonyl groups have been detected on single-crystal diamond films oxidized by anodic treatment in H$_2$SO$_4$ and especially oxygen plasma [65, 73]. Like in the case of wet-chemical oxidation, the sp^2 content was in the range of the detection limit. The results of the angle-resolved XPS measurements are shown in fig. 5.10 in comparison with the case of wet-chemical oxidation. They revealed a surface coverage with carbon-oxygen groups of 100 % and a thickness of the oxidized layer of 0.98 nm, which is a significantly higher value compared to the case of wet-chemical oxidation. However, bulk oxidation of diamond can be excluded. Therefore, the increased thickness of the surface layer may be attributed to a stable film of ions chemisorbed on the surface formed during the anodic oxidation process.

(a)   (b)
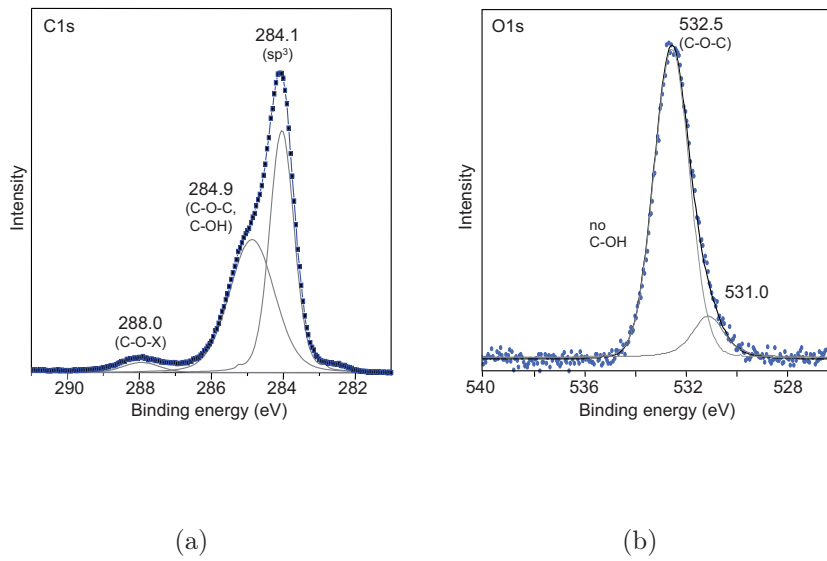
Figure 5.9: (a) C1s and (b) O1s core level spectra of single-crystal diamond after anodic oxidation
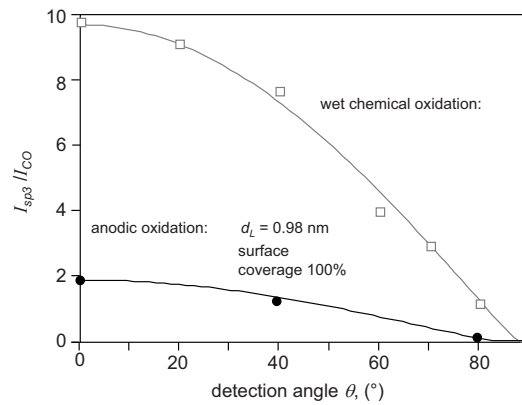
Figure 5.10: Analysis of the C1s peak for the case of anodic oxidation at different detection angles, in comparison with wet-chemical oxidation. I_{sp3} is the intensity of the sp^3 bulk signal, I_{CO} the sum of the signals related to the different carbon-oxygen groups.

5.3.4   Surface oxidized by RF oxygen plasma

Compared to anodic oxidation, the XPS measurements of the diamond surface after the oxygen plasma process showed the presence of an additional component (see fig. 5.11(a) and 5.11(b)). The corresponding peak was located at approx.

(a)   (b)
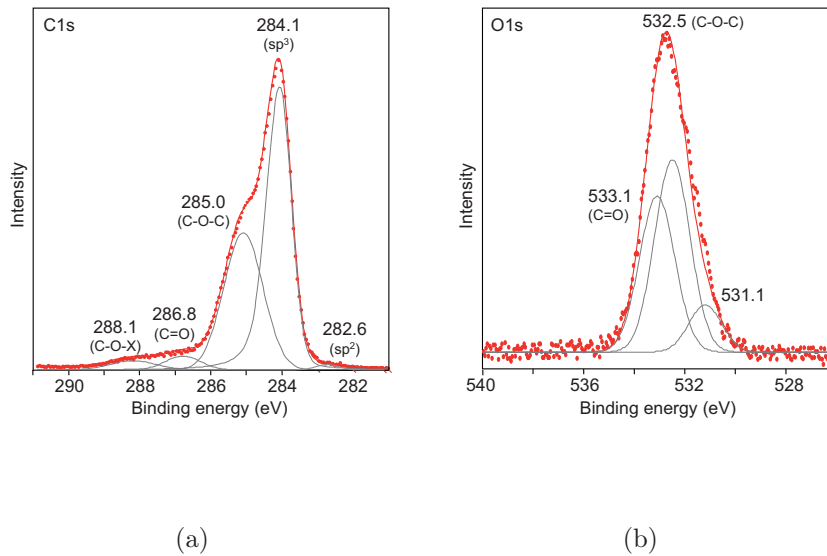
Figure 5.11: XPS spectra of single-crystal diamond after RF oxygen plasma

286.8 eV in the C1s and at 533.1 eV in the O1s spectrum, respectively. This indicates that the RF oxygen plasma generates a significant amount of carbonyl (C=O) functionalities on the diamond surface. This result is in accordance with studies shown in the references [65, 73], which compare the surface functionalities induced by oxygen plasma and anodic oxidation. Here it should be noted that some references report the opposite trend [5]. The reason is that these studies also included a treatment with DNPH (dinitro-phenyl hydrazine), which forms covalent bonds with carbonyl groups. By analyzing the amount of DNPH molecules bonded to the surface, a lower amount of carbonyl groups after oxygen plasma was recorded. This apparent discrepancy has been explained by disordering effects of the oxygen plasma, which prevent a bonding of the DNPH molecules to the surface [73].

One important aspect of each plasma process is the amount of generated defects, like non-diamond phases. The C1s spectrum after RF oxygen plasma showed a small component at approx. 282.6 eV, which can be ascribed to sp^2-like components. However, this signal was again in the range of the detection limit. This
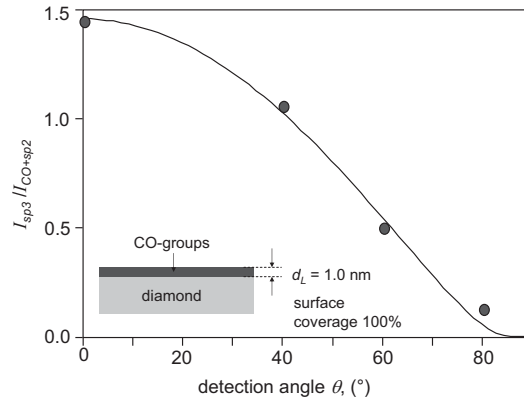
Figure 5.12: Analysis of the C1s peak for the case of RF oxygen plasma at different detection angles. I_{sp3} is the intensity of the sp^3 bulk signal, I_{CO+sp2} the sum of the signals related to the different carbon-oxygen groups and the sp^2-signal.

shows that the RF oxygen plasma is a relative soft plasma process which does not lead to a high degree of surface damage, which is a clear difference compared to the Ar/O$_2$ plasma process described below. However, even a small amount sp^2-components might affect the surface properties of the diamond electrodes.

By analyzing the measurements of the C1s peak at different detection angles (see fig. 5.12), a surface coverage of 100 % and a thickness of the carbon-oxygen layer of $d_L = 1.0$ nm were extracted, similar to the case of anodic oxidation.

5.3.5 Surface after argon/oxygen plasma etching (RIE)

The XPS measurements of the diamond electrode exposed to 30 s argon/oxygen plasma showed the effects of surface damage. The C1s spectra (fig. 5.13(a) and 5.13(b)) showed a large increase of the peak related to the sp^2-components, and a shift of the peaks related to the sp^2 and sp^3-components to higher energies. It is known that such a shift can be caused by irradiation of the surface with high-energetic ions, like in the case of ion implantation [80, 81]. Therefore, the peak at approx. 284.4 eV was ascribed to the sp^2-components and not the sp^3 bulk, which was also confirmed by the angle-dependence of this signal. The peak of the sp^3 bulk was shifted by approx. 1.3 eV to higher binding energies. The C1s core level spectrum revealed again the presence of carbonyl and more complex carbon-oxygen functional groups.

More information could be obtained from angle-resolved XPS measurements (fig. 5.14 and the comparison of fig. 5.13(a) and 5.13(b)). The XPS data could not
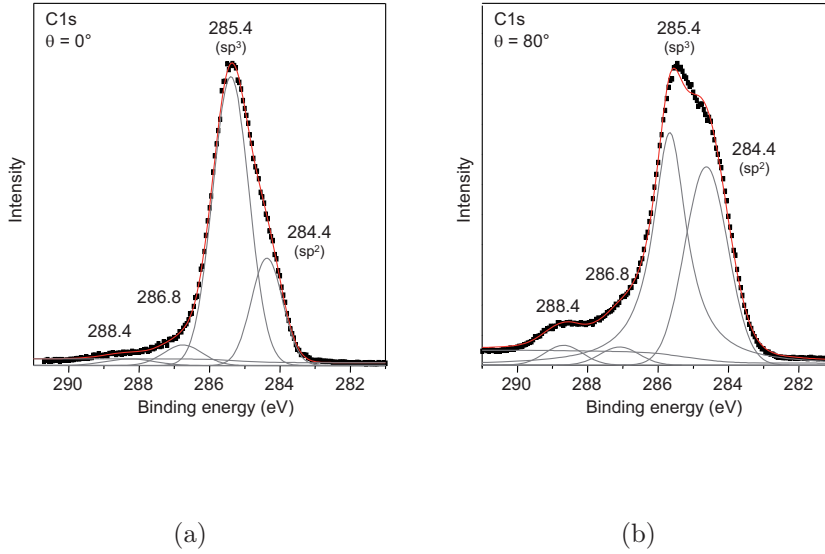
Figure 5.13: C1s core level spectra after argon/oxygen plasma (RIE): (a) 0°, (b) 80°

be fitted using the equations 5.2 and 5.3, assuming a sp³-bulk and a surface layer containing carbon-oxygen groups and sp²-phases. This indicates that the sp²-components were not limited to the surface. It is known that irradiation with high-energetic argon ions with a dose of 5×10^{14} cm^{-2} can lead to an amorphization of diamond [82]. The XPS analysis indicates that even a relative short argon/oxygen plasma treatment leads to such an amorphization of the diamond surface. Therefore, a three-layer model according to fig. 5.14(b) was used to fit the data from the angle-resolved XPS measurements. The top layer represents one monolayer of carbon-oxygen groups on the surface. Beneath, the plasma etching process induces a thin layer of α-carbon with inhomogeneous thickness, which was represented by two different thicknesses $d_{\alpha C1}$ and $d_{\alpha C2}$ with the corresponding coverages $\beta_{\alpha C1}$ and $\beta_{\alpha C2}$. The third layer consists of diamond material with irradiation defects, however below the amorphization limit. In this case, the measured intensities were fitted by the following equations: The intensity related to the carbon-oxygen layer on the top can be calculated using equation 5.2, where $d_A = d_{CO}$ is the thickness of this layer, which was set to 0.4 nm (approx. one monolayer):

$$I_{CO} = I_0 \times \left[1 - \exp\left(-\frac{d_{CO}}{\lambda \cos \theta} \right) \right] \tag{5.4}$$

(a) (b)
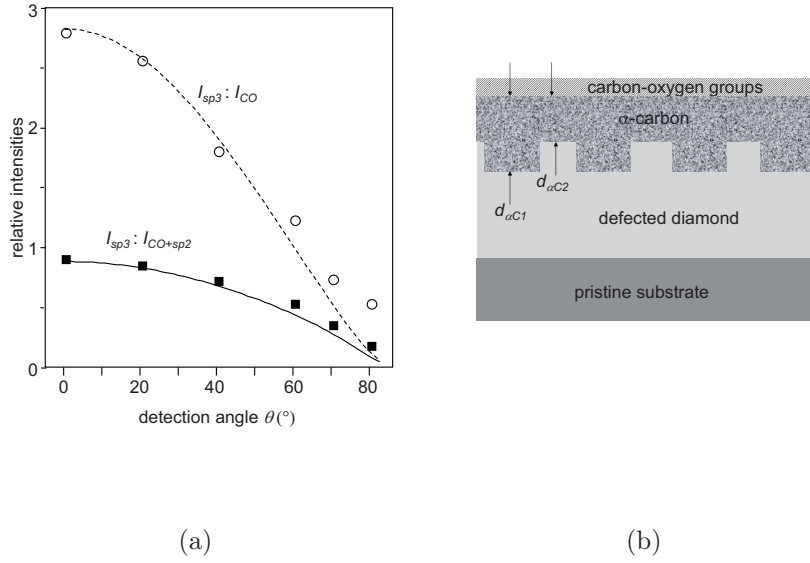
Figure 5.14: (a): Results of angle-resolved XPS measurements (C1s peak) after argon/oxygen plasma (see text), (b): surface-near structure of the diamond electrode after the plasma process.

The intensities related to the α-carbon layer with the thicknesses $d_{\alpha C1}$ and $d_{\alpha C2}$ were calculated by

$$I_{\alpha C1} = \beta_{\alpha C1} I_0 \left[1 - \exp\left(-\frac{-d_{\alpha C1}}{\lambda \cos\theta} \right) \right] \times \exp\left(\frac{-d_{CO}}{\lambda \cos\theta} \right) \qquad (5.5)$$

$$I_{\alpha C2} = \beta_{\alpha C2} I_0 \left[1 - \exp\left(-\frac{-d_{\alpha C2}}{\lambda \cos\theta} \right) \right] \times \exp\left(\frac{-d_{CO}}{\lambda \cos\theta} \right) \qquad (5.6)$$

These equations are similar to eq. 5.2 except an attenuation factor related to the carbon-oxygen layer beneath. The signal from the defective sp^3-bulk was fitted using

$$I_{sp3} = I_0 \left[\beta_{\alpha C1} \times \exp\left(-\frac{d_{\alpha C1} + d_{CO}}{\lambda \cos\theta} \right) + \beta_{\alpha C2} \times \exp\left(-\frac{d_{\alpha C2} + d_{CO}}{\lambda \cos\theta} \right) \right] \qquad (5.7)$$
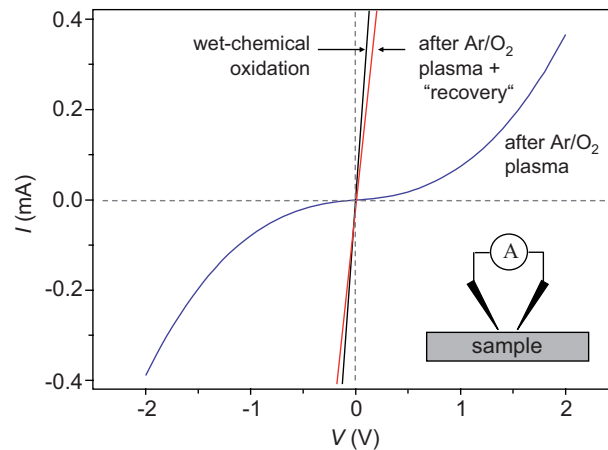
Figure 5.15: Current-voltage measurements on the surface of a highly boron-doped single-crystal diamond electrode before argon/oxygen plasma, after argon/oxygen plasma, and after subsequent annealing in hydrogen plasma and wet-chemical oxidation ("recovery treatment")

With these equations, the angle-dependent intensities related to the sp^3, the sp^2 and the CO-components could be well fitted (see fig. 5.14). The extracted maximum thickness of the α-carbon layer was approx. 4 nm. The presence of such a dielectric α-carbon layer was also clearly observed by electrical measurements. Fig. 5.15 shows the results of current-voltage measurements on a boron-doped single-crystal diamond electrode before and after the plasma process. Although these values do not allow a quantitative analysis of the conductivity (no defined resistor structure), the measurement clearly shows a large decrease of the conductivity. This is expected to limit the performance of diamond electrodes treated by the argon/oxygen plasma process, because the α-carbon layer could supress any signals from charge-transfer reactions. In some cases, the argon-oxygen plasma process could also lead to completely insulating surfaces, although the boron-doped layer was not completely etched. This shows that the argon/oxygen plasma etching process was not completely reproducible.

5.3.6   Effect of annealing in hydrogen plasma after RIE

The XPS analysis of the diamond films exposed to argon/oxygen plasma have shown that this process induces a large amount of defects and a thin amorphous layer on the diamond surface. This layer is expected to degrade the performance of diamond electrodes or electronic devices exposed to such process. An example

for this will be shown in chapter 7. A possible solution for this problem could be a surface post-treatment that restores the initial surface characteristics.
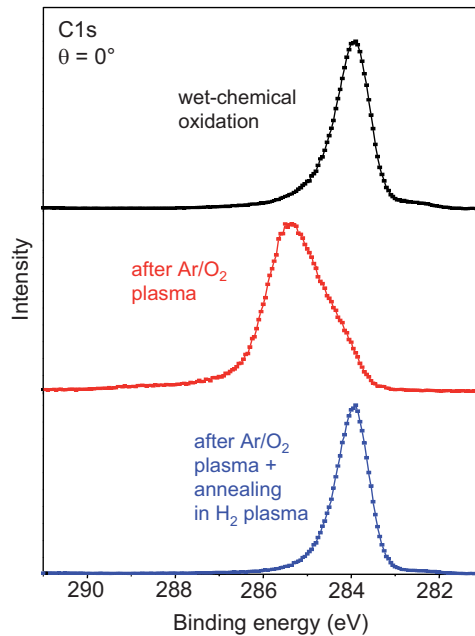
Figure 5.16: C1s spectrum after argon/oxygen plasma and annealing treatment in hydrogen plasma in comparison with wet-chemical oxidation and argon/oxygen plasma without annealing

 Such post-treatment could be an annealing process at high temperature. However, the effect of an annealing process in vacuum depends on the amount of defects induced by the plasma process. If this defect density was below the amorphization limit, the diamond films can be completely restored [81, 82]. In the other case, the annealing process converts the α-carbon layer into graphite. Such effect could be expected in the case of the RIE process. Therefore, a hydrogen plasma treatment at high temperature (650 °C - 700 °C) was used as the post-treatment, since the hydrogen plasma is expected to etch the graphite layer. The process time was approx. 10 minutes.

After the hydrogen plasma process, the diamond surface was again oxygen-terminated by wet-chemical oxidation. Fig. 5.16 shows the C1s spectrum after this recovery treatment in comparison with the data before the annealing in hydrogen plasma (plus subsequent wet-chemical oxidation) and for the wet-chemically oxidized surface (see also previous sections). The XPS spectra clearly

show that the initial surface conditions could be restored by the annealing treatment in hydrogen plasma. The treatment was therefore also included into the fabrication process of the microelectrode array shown in chapter 7.
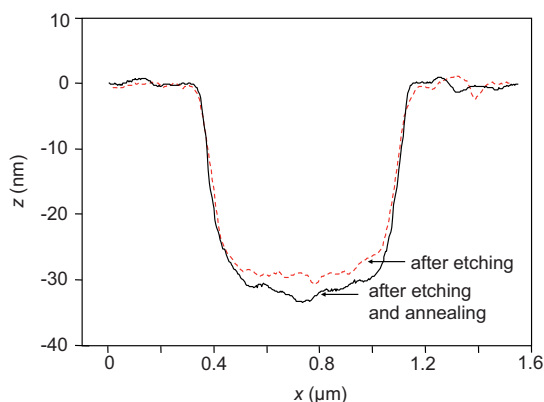
Figure 5.17: AFM images of a hole etched by argon/oxygen plasma before and after subsequent annealing in hydrogen plasma

Fig. 5.17 shows the high-resolution AFM images of one etched hole with approx. 500 nm in diameter directly after the etching in argon/oxygen plasma and after subsequent annealing. It can be seen that the depth of the holes after this post-treatment slightly increased by 3 nm, which is close to the depth of the α-carbon layer as estimated by angle-resolved XPS measurements. This verifies that the effect of the post-treatment is an etching of the α-carbon top layer. Before the electrochemical characterization of the electrode, the effect of this "recovery" treatment on the conductivity was determined (see fig. 5.15). It can be seen that the initial conductivity was almost completely restored.

5.4   Summary

The XPS analysis has shown that different surface oxidation treatments induce various carbon-oxygen functionalities at the diamond surface. Wet-chemical oxidation converts the hydrogen termination of the as-grown surface into oxygen termination with a surface coverage of approx. 100 %, where the thickness of the oxidized layer corresponds to one monolayer. The surface functionalities are mainly hydroxyl- and ether groups. Anodic oxidation in alkaline electrolyte is a very effective method for the surface oxidation of diamond electrodes, since it leads to a fully oxidized surface and removes all non-diamond components. Besides, the XPS measurements indicate the presence of more complex carbon-oxygen groups, e.g. polycarbonate groups.

The RF oxygen plasma process without any DC bias induces additional surface carbonyl groups. The XPS measurements did not show a significant increase in the sp^2-content. Like in the case of wet-chemical and anodic oxidation, the contribution of the corresponding signal was below the detection limit.

On the other hand, a reactive ion etching process in argon/oxygen plasma induces even at relative low power (25 W) a significant amount of defects. In addition, the diamond surface is converted into a non-diamond, probably an α-carbon film. However, the initial surface characterisitcs can be almost restored by hydrogen plasma at about 700 °C. The effect of this post-treatment treatment could be a conversion of the α-carbon layer into graphite, which is then etched by the hydrogen plasma. This treatment will be very useful for the fabrication of microelectrode arrays, as shown in chapter 7.

The results of the XPS measurements are summarized in table 5.1.

	wet-chemical	anodic	RF O$_2$ plasma	Ar/O$_2$ plasma
hydroxyl (C-OH)	yes	no	no	?
ether (C-O-C)	yes	high	high	?
carbonyl (C=O)	no	no	yes	yes
C-O-X	no	small	small	small
sp^2	-	-	—	20-30%
d_L [nm]	0.22	0.98	1.0	1.8

Table 5.1: Results of XPS analysis

Chapter 6

Electrochemical Characterization of Oxygen-terminated Diamond Electrodes

In the previous chapter, it has been shown that the carbon-oxygen functional groups and the amount of non-sp^3 phases can be controlled by the choice of the oxidation treatment. In this chapter, the effect of the different oxidation treatments on the electrochemical characteristics of diamond will be discussed and correlated to the XPS results. In addition, the cases of single-crystal and nanocrystalline diamond will be compared.

One main aspect of the electrochemical characterization will be the evaluation of the electronic surface barrier in contact with the electrolyte, which can be determined from the measured flatband potential. Usually, it is assumed that the electronic surface barrier on oxygen-terminated diamond is approx. 1.7 eV, as observed e.g. by Kelvin force microscopy [51]. Similar surface barriers in the range between 1.5 eV and 2.0 eV have been observed for metal-diamond Schottky diodes [83, 84, 85]. Electrochemical measurements of the flatband potential in electrolytes have performed in several previous studies [58, 62, 63, 66, 86, 87]. The results showed that the flatband potential of diamond electrodes can be changed by anodic polarization (when a Faradaic current flows through the diamond electrode), by plasma treatments, or by annealing under oxygen atmosphere. However, in most cases it was only distinguished between hydrogen- and oxygen termination. Besides, the analysis was limited to capacitance-voltage measurements in the electrolyte. As it will be shown in the following sections, it might be important to perform complete impedance measurements to extract exact values for the electronic surface barrier.

6.1   Single-crystal diamond electrodes

6.1.1   Wet-chemical oxidation

The single-crystal diamond electrodes oxidized by wet-chemical treatment showed a typical wide potential window of water dissociation of approx. 3 V for current densities in the $\mu A/cm^2$-range and very low background currents below $1\ \mu A/cm^2$, as shown in fig. 6.1. The measurement was recorded after several previous cycles, as mentioned in chapter 4. The diamond electrode showed a small activity
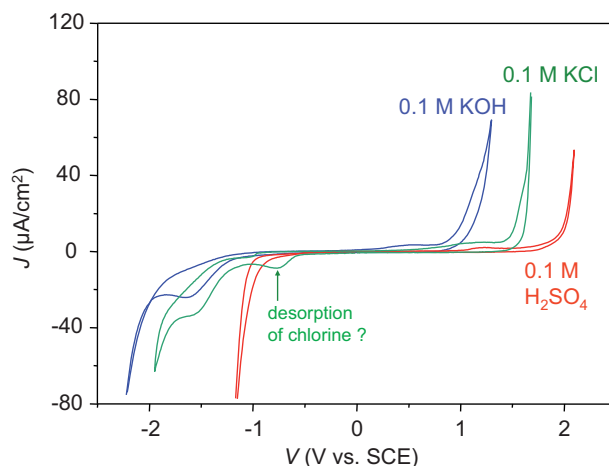
Figure 6.1: Cyclic voltammetry plots at $s = 50$ mV/s for single-crystal diamond electrode after wet-chemical oxidation

prior to the onset of the oxygen evolution in all three electrolytes (0.1 M H_2SO_4, 0.1 M KCl, 0.1 M KOH). The corresponding peak current was in the range of $4\ \mu A/cm^2$. Similar peaks with different intensities have also been observed on hydrogen-terminated diamond and been ascribed to an oxidation of the surface [13, 65, 88]. However, the electrodes used in this work had already been oxidized. In addition, the anodic current did not decrease with the number of cycles, as it would be expected for a surface oxidation process. Therefore, the anodic current prior to the onset of the oxygen evolution reaction is most probably related to adsorption and desorption processes. Additionally, especially the voltammograms in 0.1 M KCl and 0.1 M KOH showed cathodic current peaks in the range of -1.5 V to -2.0 V vs. SCE prior to the onset of the hydrogen evolution. This behavior was again also identified for the other oxidation treatments and can be ascribed to adsorption processes. Such effects will be discussed more in detail for anodic oxidation, since the anodic current peak was much more pronounced in that case. In 0.1 M KCl (pH ≈ 7), the additional cathodic peak at approx. -0.75 V vs. SCE
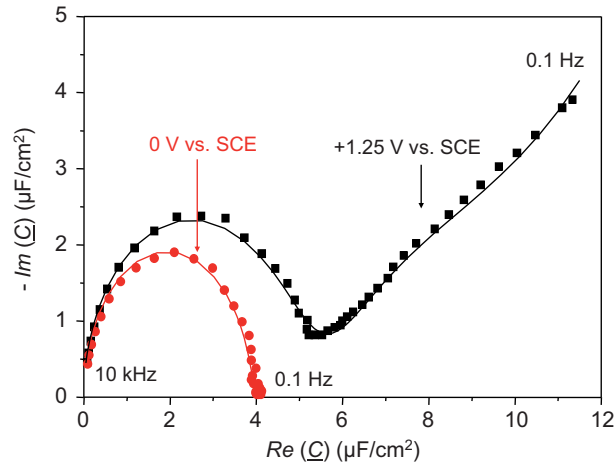
Figure 6.2: Impedance spectroscopy measurements (capacitance plots) at two different potentials in 0.1 M H_2SO_4 electrolyte. For the fitting, the equivalent circuits from fig. 4.7(c) and 4.7(d) were used (see text)

might be associated to the reduction of chlorine, which can be formed during the anodic scan as a side-product of the oxygen evolution [88] or with the desorption of chloride ions. Here it should be noted that there are many reports in literature which describe the electrochemical characteristics of diamond electrodes in acidic electrolytes, but nearly none which show corresponding measurements in alkaline solutions. This might be explained by the more complex behavior of diamond electrodes in KOH or other bases, which will also influence the impedance charaterisitcs shown below.

Typical impedance spectroscopy measurements in 0.1 M H_2SO_4 at two different potentials are shown in fig. 6.2. At 0 V vs. SCE, the data could be fitted by a single RQ-circuit with a small series resistance. The parallel resistance was in the $M\Omega$ cm^2-range and could therefore be neglected. This corresponds to the simple case of fig. 4.7(c). On the other hand, the adsorption process in the anodic region had a significant effect on the impedance spectrum at +1.25 V vs. SCE. In this potential range, the data could only be fitted by the equivalent circuit shown in fig. 4.7(d), which includes an additional RQ-series connection in parallel to the depletion- or double layer capacitance. The fitting parameters are shown in table 6.1. Since the n-factor of the constant phase element Q_1 corresponding to depletion- and double layer was between 0.99 and 1.0, it could be simplified to an ideal capacitance C_1. Taking impedance spectroscopy measurements at different potentials, the Mott-Schottky plots shown in fig. 6.3 could be extracted. For anodic potentials where the equivalent circuit contained the additional elements

V (V vs. SCE)	R_1 (MΩcm^2)	C_1 ($\mu F/cm^2$)	R_2 (kΩcm^2)	Q_2 (μS $\cdot$ s^n/cm^2)	n_2 (of Q_2)
0.00	>50	4.16	-	-	-
+1.25	1.53	7.7	46.0	4.0	0.70

Table 6.1: Fit parameters for the impedance measurements shown in fig. 6.2, using the equivalent ciruict from fig. 4.7(d). At $V = 0$ V vs. SCE, C_1 can be considered as a series connection of C_{SC} and C_{DL}, according to fig. 4.7(c)
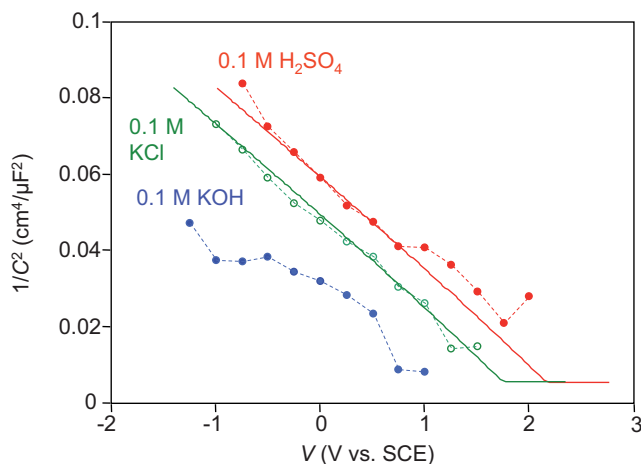
Figure 6.3: Mott-Schottky plots for single-crystal diamond electrode after wet-chemical oxidation. The solid lines show the fits for the cases of H$_2$SO$_4$ and KCl.

Q_2 and R_2, only the value of the capacitance C_1 was considered. The data were fitted using the model described in chapter 4, using the equations 4.8 and 4.9. The deviation from the measured values at potentials in the range of the adsorption peak might be explained by the more complicated equiavlent circuit at these potentials.

As expected, the curves showed a pH-dependent shift due to the pH sensitivity of the oxygen-terminated surface. For the analysis of the wet-chemically oxidized diamond surface, it was difficult to extract the exact value of the electronic surface barrier, since the value of the double-layer capacitance could not be clearly resolved. Taking a typical value of C_{DL} = 15-20 μF/cm^2 yielded an electronic surface barrier after wet-chemical oxidation of approx. 1.4 eV for measurements in H$_2$SO$_4$ (pH = 1) and KCl (pH $\approx$ 7) electrolyte. However, the extraction of the electronic surface barrier from the data for 0.1 M KOH (pH = 13) was more diffi-

pH	V_{FB} (V vs. SCE)	V_{OCP} (V vs. SCE)	$q\phi_B$ (eV)
1	+2.2	$\approx$ +0.4	1.4
7	+1.75	+0.12	1.3
13	$\leq$ 1.0	-0.14	0.9 - 1.2

Table 6.2: Extracted surface barriers of single-crystal diamond after wet-chemical oxidation

cult and could lead to a lower value. Besides, the slope of the Mott-Schottky plot appeared to be different compared to the measurements in the other two solutions, although the doping concentration is the same. Assuming a not completely pinned surface potential, the electronic surface barrier might be pH-dependent. However, the values extracted from the measurements in pH = 1 and pH = 7 do not show a significant pH dependence, which points to a fixed electronic surface barrier. A possible explanation for the different results in pH = 13 could be therefore the slightly increased background current, which was also observed in cyclic voltammetry measurements. The correct equivalent circuit in pH = 13 might contain additional elements related to e.g. adsorption and desorption processes, which cannot be clearly resolved in the limited frequency range and which are therefore contributing to the overall capacitance. A similar effect was also recorded for other surface oxidation treatments, as shown below. Therefore, the results from the measurements in pH = 1 and pH = 7 electrolytes were taken as the electronic surface barrier.

When characterizing diamond electrodes oxidized by wet-chemical treatment and comparing the results to the case of anodic oxidation, one has to take into account that cycling between the onset potentials of hydrogen- and oxygen evolution corresponds to a weak anodic treatment. Therefore, one has to ensure that the transferred charge during the cyclic voltammetry measurements is at least low compared to that during the anodic treatment. This was the case for the following measurements: The transferred charge during the measurements was less than 1 mC/cm^2 or below, compared to 20 mC/cm^2 for the anodic oxidation process discussed in the next section.

6.1.2 Anodic oxidation

Fig. 6.4 shows the cyclic voltammetry plots of a single-crystal boron-doped diamond electrode in 0.1 M H$_2$SO$_4$ (pH = 1) and 0.1 M KOH (pH = 13) after anodic oxidation. There were no significant differences between initially hydrogen-terminated and wet-chemically oxidized electrodes after they were subjected to the anodic treatment, as mentioned before. The cyclic voltammetry measurement in 0.1 M KCl electrolyte did not show any additional effects and is therefore not shown for simplicity. In pH = 1, the onset potentials of hydrogen and oxygen

evolution (taken at a value of 20 $\mu A/cm^2$) were approx. -1.35 V vs. SCE and +2.1 V vs. SCE, respectively, corresponding to a potential window of approx. 3.5 V. In pH = 13, the observed potential window was smaller by 0.4 V, since the oxygen evolution started already at +1.0 V vs. SCE.
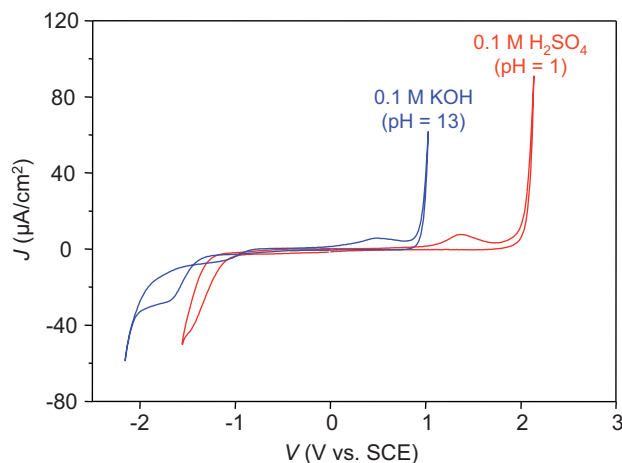
Figure 6.4: Cyclic voltammetry plots for single-crystal diamond electrode after anodic oxidation

 A comparison with the cyclic voltammetry results for wet-chemical oxidation (in pH = 1) might suggest that the onset of the hydrogen evolution has been shifted to higher cathodic potentials after the anodic treatment. In fig. 6.5, the cyclic voltammetry plots for wet-chemical and for anodic oxidation are shown in semilogarithmic scale. It can be seen that the slope for the hydrogen evolution has also changed. This difference can be ascribed to a higher electronic surface barrier (see below), since cathodic potentials correspond to a depletion of the diamond surface, or to a change in the carbon/oxygen surface groups, as revealed from the XPS analysis. The onset potential for the oxygen evolution was not significantly changed by the anodic oxidation process.

Fig. 6.4 and 6.5 show also a current peak prior to the onset of the oxygen evolution reaction, which has already been observed for the case of wet-chemical oxidation, however with less intensity. Besides, the semilogarithmic plot shows a significant difference in the current levels before and after the hydrogen- and oxygen evolution reaction, respectively. The change of the current with the electrode potential within the potential window was much higher than it would be expected for a purely capacitive current. These effects were more pronounced for anodic compared to wet-chemical oxidation.
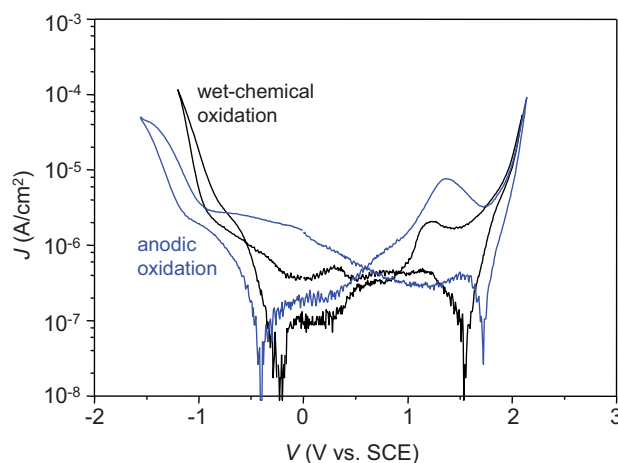
Figure 6.5: Cyclic voltammetry plots in 0.1 M H_2SO_4 electrolyte for wet-chemical and anodic oxidation in semilogarithmic scale. The onset potential for the hydrogen evolution is similar for both cases.

The origin of these effects becomes more clear in fig. 6.6(a) and 6.6(b). Fig. 6.6(a) shows the anodic current peak prior to the oxygen evolution when the cathodic potentials during the cyclic voltammetry scans were limited to different values. All shown measurements were recorded after several previous scans and were reproducible. Fig. 6.6(a) shows that the anodic current peak becomes much less pronounced when the electrode potential is not extended to the range of the hydrogen evolution reaction. The current peaks corresponded to a charge of approx. 1.2×10^{14} q/cm^2, 2.8×10^{14} q/cm^2 and 5.5×10^{14} q/cm^2 for the three shown cases, respectively. This corresponds to approx. 10 %, 30 % and 60 % of one monolayer, respectively. In a similar way, the hysteresis-like cathodic current in the reverse scan becomes lower when the potential is not extended to potentials corresponding to the anodic adsorption peak, as shown in fig. 6.6(b). Extending the potential to the range of the oxygen evolution did not lead to any additional increase in this cathodic current.

From these results, it can be concluded that the anodic current peak prior to the onset of the oxygen evolution and the hysteresis-like cathodic current after scanning to the hydrogen evolution are most likely related to slow adsorption and desorption processes. Since these effects were observed in all three electrolytes (H_2SO_4, KCl, KOH), it is most likely related to adsorption or desorption of oxygen or hydrogen and not of sulphate or chloride ions. Similar adsorption effects are also observed on Pt or Au electrodes [12, 56]. This shows that the diamond surface is not completely inactive within the potential window of water dissozia-
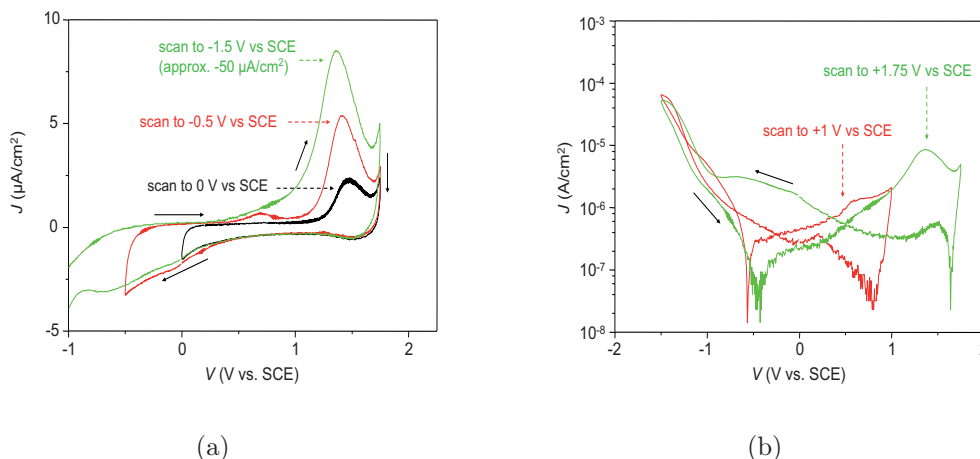
Figure 6.6: Cyclic voltammetry measurements in 0.1 H_2SO_4 electrolyte at 50 mV/s. (a): Anodic peak current after scanning to different cathodic potentials, (b): Cathodic current after cycling to different anodic potentials. The arrows show the scan direction.

tion, although the corresponding adsorption- and desorption currents are approx. two orders of magnitude lower compared to metal electrodes (see fig. 2.1).

However, a small anodic current peak prior to the onset of the oxygen evolution reaction was visible even when the potential was limited in the cathodic direction to 0 V vs. SCE, which is above the equilibrium potential of the hydrogen evolution reaction, which is approx. -0.3 V vs. SCE in pH = 1 (see fig. 4.1). Therefore, this peak is probably related not only to adsorption and desorption processes. However, the second effect is not completely clear yet.

The background current in the range of no activity was in the range of 0.3 $\mu A/cm^2$, taking the lower values before the hydrogen reaction into account. Assuming an average interface capacitance of 3-4 $\mu F/cm^2$ (see fig. 6.7 and table 6.3), the capacitive current at the scan rate of 50 mV/s should be 0.15 to 0.2 $\mu A/cm^2$, which is close to the measured value. This shows that this background current is dominated by charging and de-charging of the interface capacitances. Fig. 6.7 shows the results of impedance spectroscopy measurements in 0.1 H_2SO_4 (pH = 1) electrolyte at two different electrode potentials: At $V = 0$ V vs. SCE, the measurement revealed the presence of just one RC-circuit and a series resistance, where the parallel resistance was in the range of 10 $M\Omega cm^2$ and could therefore be neglected. The capacitance C_1 was again replaced by a constant phase element with an n-factor close to one. This is in accordance with the cyclic voltammetry measurements which show no activity in this potential range. On the other hand, the impedance measurement at $V = +1.25$ V vs. SCE revealed the presence of an adsorption process, which can be described by an additional series connection of a resistor and a CPE (R_2Q_2) in parallel to the simple RC-circuit (see fig. 4.7(d).
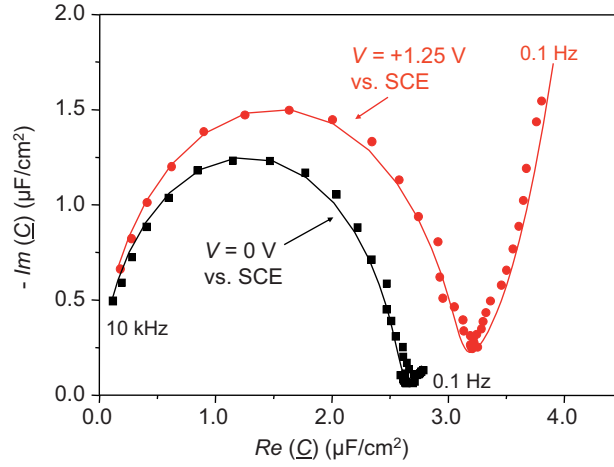
Figure 6.7: Capacitance plots for impedance spectroscopy measurements in 0.1 H_2SO_4 at 0 V vs. SCE and +1.25 V vs. SCE for the case of anodic oxidation. Symbols: measured data, lines: fits

These results were very similar to the case of wet-chemical oxidation. The fitting values for the shown impedance measurements are shown in table 6.3.

V (V vs. SCE)	R_1 ($M\Omega cm^2$)	C_1 ($\mu F/cm^2$)	R_2 ($M\Omega cm^2$)	Q_2 ($\mu S \cdot s^n/cm^2$)	n_2
0.0	16.0	2.76	-	-	-
+1.25	1.1	3.3	0.14	0.77	0.54

Table 6.3: Fit parameters for the impedance measurements in fig. 6.7, taking the equivalent circuit fróm fig. 4.7(d). R_1 and C_1 are related to a combination of depletion- and double layer, R_2 and Q_2 to adsorption.

Fig. 6.8 shows the Mott-Schottky plots obtained from impedance spectroscopy measurements in 0.1 M H_2SO_4, 0.1 M KCl and 0.1 M KOH, and a fit according to the MOS-like model for the case of KCl. The slope corresponded to a doping concentration of $N_A = 5.5 \times 10^{20}$cm^{-3}. The value of the double layer capacitance was taken to approx. 18 $\mu F/cm^2$ in all electrolytes and independent on any applied potential. In 0.1 H_2SO_4 and 0.1 M KCl, the measurements yielded in a similar electronic surface barrier of approx. 1.7 eV. This value is by approx. 300 mV higher compared to the case of wet-chemical oxidation. The extracted surface barrier in pH = 13 could be in the range of 1.4 eV. Like in the case of wet-chemical oxidation, this lower extracted value is most likely not due to a
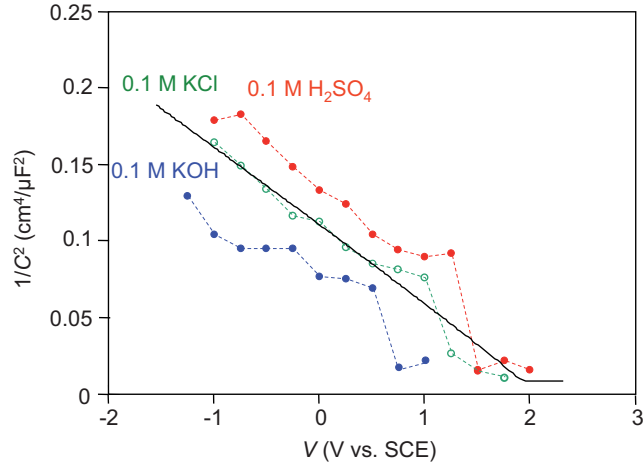
Figure 6.8: Mott-Schottky plots for single-crystal diamond electrode after anodic oxidation. The solid line shows the fit for 0.1 M KCl.

pH	V_{FB} (V vs. SCE)	V_{OCP} (V vs. SCE)	$q\phi_B$ (eV)
1	+2.5	+0.44	1.75
7	+2.0	+0.04	1.67
13	+1.3-1.5	-0.10	1.2 - 1.5

Table 6.4: Extracted surface barriers of single-crystal diamond after anodic oxidation

lower surface barrier, but related to additional parasitic elements in the equivalent circuit (which can not be resolved within the measurement frequency range). Additional anodic or cathodic treatments did not induce any significant further shift of the Mott-Schottky plots to higher anodic potentials, even if the amount of transferred charge was increased. This shows the electrochemical stability of this surface termination, which is important for applications under high potentials, e.g. for the oxidation of organic compounds.

The results for anodic oxidation are summarized in table 6.4. Anodic oxidation results in a significantly higher surface barrier compared to the case of wet-chemical oxidation. This can be explained by the induced carbon-oxygen surface functionalities and the chemisorbed surface layer (see results from XPS). Besides, the anodic oxidation treatment leads to a very stable surface termination, which can be modified only by plasma treatments. Anodic oxidation is therefore very attractive for electrode and ISFET applications, especially for the operation at high anodic or cathodic potentials.

6.1.3 RF oxygen plasma

The results of the cyclic voltammetry measurements of the single-crystal diamond electrode oxidized by RF oxygen plasma are shown in fig. 6.9. The background
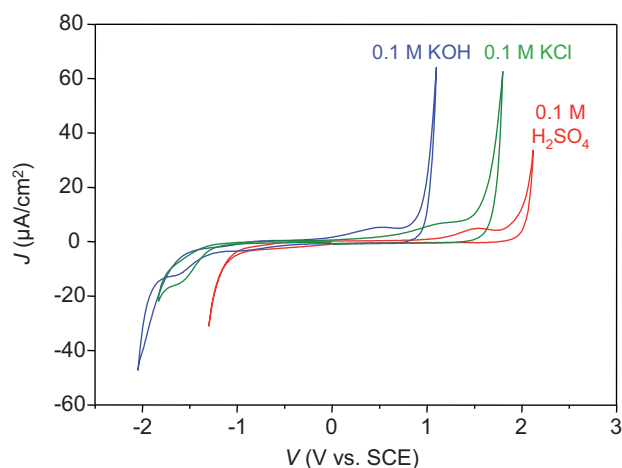
Figure 6.9: Cyclic voltammetry of single-crystal diamond oxidized by RF oxygen plasma

current within the most part of the potential window and the onset potentials for the oxygen evolution were not significantly changed compared to anodic oxidation. The onset of the hydrogen evolution reaction was slightly shifted to lower potentials compared to the case of anodic oxidation, which could be related to a lower electronic surface barrier (see analysis below). The electrode oxidized by the plasma treatment also showed slightly modified adsorption characteristics at potentials prior to the onset of the oxygen evolution, compared to the case of anodic oxidation. This effect was more pronounced in 0.1 M KCl and 0.1 M KOH compared to 0.1 M H_2SO_4. The adsorption peak in the anodic regime was broadened by the oxygen plasma treatment, while the peak current did not change significantly. The change in the adsorption characteristics could be ascribed to the increased amount of carbonyl groups on the diamond surface induced by the plasma treatment.

The slightly increased surface activity of the diamond electrode treated by RF oxygen plasma became more dominant in the impedance spectroscopy measurements in 0.1 M KCl (pH = 7) and KOH electrolyte. A typical capacitance plot is shown in Fig. 6.10. The measurement was performed at an electrode potential of +0.5 V vs. SCE. The increased surface activity of the plasma-oxidized electrode compared to the case of anodic oxidation resulted in a decreased parallel resistance R_{DL} of the double layer. Therefore, the data could not be
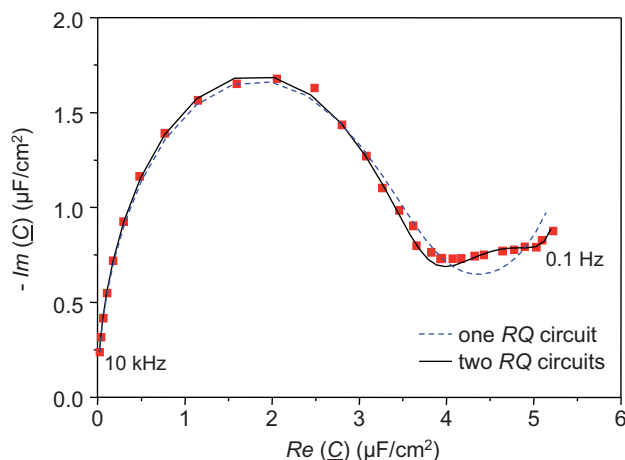
Figure 6.10: Results of impedance spectroscopy at $V = +0.5$ V vs. SCE in 0.1 M KCl electrolyte. The lines show the fits with one (dashed) and with two (full line) RQ-circuits.

fitted with the simplified model from fig. 4.7(c). Instead, it was possible to resolve the two RQ-circuits corresponding to depletion- and double layer (see circuit in fig. 4.7(b)). At the electrode potential of $V = +0.5$ V vs. SCE, the fitting values were $Q_{SC} = 5.35$ μF/cm^2, $R_{SC} = 1.8$ MΩcm^2, $Q_{DL} \approx 25$ μF/cm^2 (nominal capacitance) and $R_{DL} = 9$ kΩcm^2. Similar results were obtained for other electrode potentials in pH $= 7$. On the other hand, only one RQ-circuit could be extracted from impedance measurements in pH $= 1$, since the resistance corresponding to the double layer close to the MΩcm^2 -range.

The results of the Mott-Schottky plots for pH $= 1$ and pH $= 7$ are presented in fig. 6.11. Both curves were fitted using a doping concentration of $N_A = 5.5$ $\times 10^{20}$cm^{-3} and a double-layer capacitance of $C_{DL} = 18$ μF/cm^2. The deviations from the fits at higher anodic potentials can be again explained by the effect of adsorption processes. For pH $= 1$, the total capacitance is plotted versus the total electrode potential, according to the equations 4.8 and 4.9. However, for pH $= 7$, the extracted depletion layer capacitance according to equation 4.7 and not the total capacitance is plotted versus the total electrode potential, since it was not possible to fit the data adequately with only one RQ-circuit. This explains the slightly different slopes, although the doping concentration is the same. The deviations between measurement results and fits for potentials above 1.0 V vs. SCE (pH $= 1$) and approx. $+0.5$ V vs. SCE (pH $= 7$) can again be explained by the adsorption peaks revealed in cyclic voltammetry (see fig. 6.9). The results are summarized in table 6.5. The results for pH $= 13$ are not shown
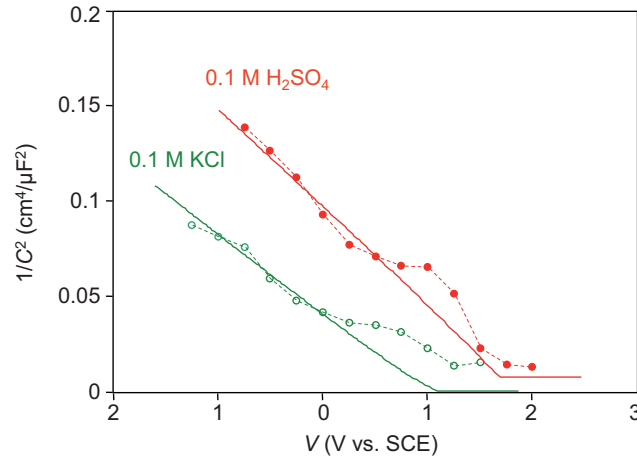
Figure 6.11: Mott-Schottky plots for single-crystal diamond electrode oxidized by RF oxygen plasma. For 0.1 M KCl, the depletion layer capacitance and not the overall capacitance is displayed (see text). The deviations between measurements and fit are also adressed in the text.

pH	V_{FB} (V vs. SCE)	V_{OCP} (V vs. SCE)	$q\phi_B$ (eV)
1	+1.70	+0.36	1.05
7	+1.1	+0.05	0.9-1.0

Table 6.5: Extracted surface barriers of single-crystal diamond after RF oxygen plasma

since they lead again to a low value of the surface barrier, similar to the cases of anodic and wet-chemical oxidation. The measurements revealed a reduced surface barrier of $q\phi_B \approx 1.0$ eV after oxygen plasma treatment in H_2SO_4 and KCl electrolyte, compared to approx. 1.7 eV after anodic oxidation. The reduced surface barrier could be explained by the carbonyl groups induced by the plasma process, or by a slight amount of plasma-induced defects creating new electronic surface states. Here it must be noted that the XPS measurements did not resolve a significant amount of sp^2 components. However, even a low amount (in the range of the resolution limit of the XPS measurements) could affect the characterisitcs of the diamond electrodes. This explanation may be also supported by the results for the argon/oxygen plasma treatment (see below), which show similar trends (parasitic elements in the equivalent circuit and low extracted surface barrier), but significantly more pronounced.

The characteristics of the diamond electrodes oxidized by RF oxygen plasma were also very stable and not significantly changed by anodic or cathodic treatments.

6.1.4   Argon/oxygen plasma (RIE)

As revealed by XPS measurements, the Ar/O_2 plasma process leads to a strong modification of the diamond surface. It could therefore be expected that also the electrochemical characteristics of the electrode will change due to such a surface treatment. Fig. 6.12 shows typical cyclic voltammetry plots of a highly-boron-doped SCD electrode in 0.1 M H_2SO_4 and 0.1 M KOH after 45 s argon/oxygen plasma. The plasma etching treatment leads to an increase of the background
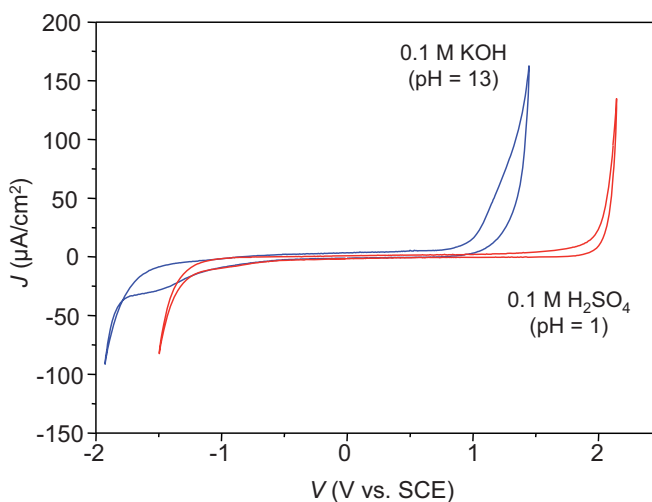
Figure 6.12: Cyclic voltammetry plots of a single-crystal diamond electrode after 60 s argon/oxygen plasma etching.

compared to anodic oxidation, especially for low cathodic potentials. This is also shown in fig. 6.13, which shows the cyclic voltammetry curves of argon/oxygen plasma and anodic oxidation in pH = 1 in semilogarithmic scale. The increased background current can be attributed to an increase in the interface capacitance (see below), and to an increase of the parasitic surface activity (e.g. due to defects). The onset potentials of hydrogen- and oxygen evolution were not significantly changed by the plasma treatment. However, the adsorption peak prior to the oxygen evolution was now nearly completely smoothed, which might be explained by the surface layer. The significantly modified surface induced by the plasma etching treatment was also visible in electrochemical impedance spectroscopy measurements. As an example, the capacitance plot for $V = 0$ V vs.
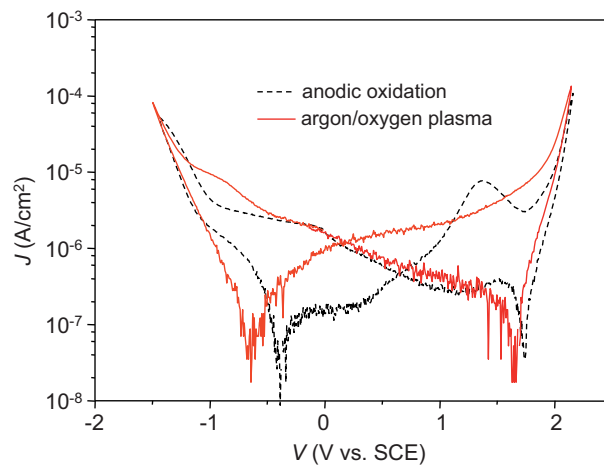
Figure 6.13: Cyclic voltammetry plots in 0.1 H_2SO_4 of single-crystal diamond electrodes exposed to argon/oxygen plasma compared to the case of anodic oxidation.
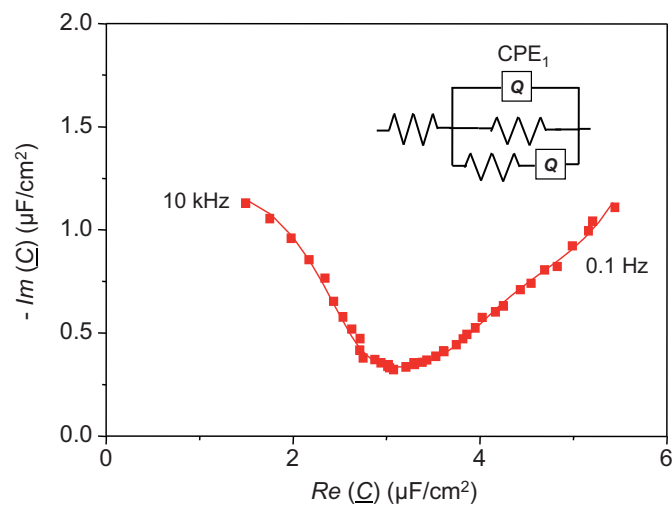
Figure 6.14: Capacitance plot of a single-crystal diamond electrode after 60 s argon/oxygen plasma etching in pH $= 1$ electrolyte at $V = 0$ V vs. SCE. The equivalent circuit is shown in the insert.
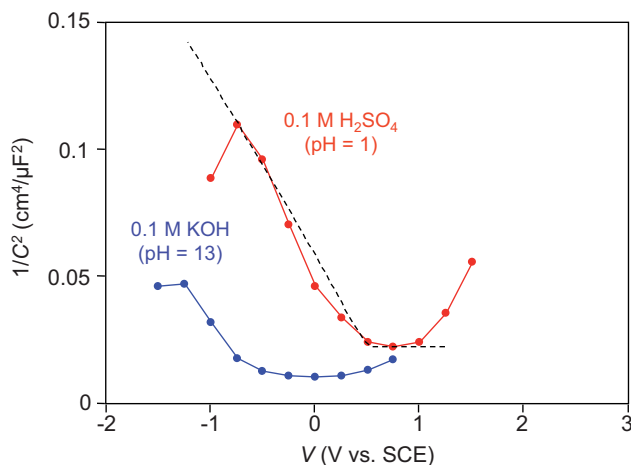
Figure 6.15: Mott-Schottky plots of the single-crystal diamond electrode after 60 s argon/oxygen plasma etching

SCE in 0.1 H_2SO_4 electrolyte is shown in fig. 6.14. In the case of wet-chemical and anodic oxidation, the data at this potential could be fitted by a single RC-circuit with a high value for R, as seen in fig. 6.7. However, the more complicated equivalent circuit according to fig. 4.7(d) was in this case required for an appropriate fit. Such equivalent circuit was used in the cases of wet-chemical and anodic oxidation only in the potential region of adsorption prior to the oxygen evolution reaction. Besides, the n-factor of the CPE Q_1 corresponding to depletion- or double layer was in the range of 0.93, which is relative low compared to the cases of anodic, wet chemical or RF oxygen plasma oxidation. These effects might be explained by the inhomogeneous α-carbon layer and the defected diamond layer underneath, as revealed by XPS measurements.

As to be expected, the argon/oxygen plasma had also a significant effect on the Mott-Schottky plots, as shown in fig. 6.15. Within the potential window of water dissociation, the Mott-Schottky plot was shifted to lower anodic potentials compared to the cases of wet-chemical and anodic oxidation, which corresponds to a low flatband potential. Besides, the maximum value of the capacitance at high anodic potentials was decreased from 10-12 $\mu F/cm^2$ for anodic oxidation to approx. 7 $\mu F/cm^2$ after the plasma treatment. The latter effect could be either explained by a decrease of the double-layer capacitance, or by an additional dielectric layer. This layer could be associated with the α-carbon film on the electrode surface, which was resolved by the XPS characterization. However, a homogenous dielectric layer would result in a even lower capacitance than observed, taking a thickness of 2-4 nm and a low dielectric constant of $\varepsilon_{a-C} \approx$

3.0 [89] into account. For potentials above flatband, the value of $1/C^2$ increased again. In this case, the measured capacitance is most likely significantly affected by adsorption and desorpton processes.

Fig. 6.15 shows that a fit for the Mott-Schottky plot leads to much lower flatband potentials than for wet-chemical, anodic, and RF oxygen plasma oxidation. For the case of argon/oxygen plasma, it was difficult to give an exact value for the surface barrier due to the significant influence of parasitic elements to the total impedance (see results from impedance spectroscopy). However, fig. 6.15 indicates that the electronic surface barrier should be very low, which can be ascribed to surface states due to the high amount of plasma-induced defects. Fitting the Mott-Schottky plot with the equations 4.8 and 4.9 (solid line in Fig. 6.15) yields in a surface barrier in the range of 0.5 eV.

As already mentioned before, the argon/oxygen plasma process could also lead to completely insulating surfaces. The transition from the state described above to the insulating state occurred within a few seconds of process time. When the diamond surfaces were completely insulating, no electrochemical measurements were possible.

6.1.5 Surface annealing in hydrogen plasma

The previous section has shown that the defects induced by the argon/oxygen plasma process change the electrode characteristics significantly. As shown by the XPS analysis, the exposure of the diamond films to hydrogen plasma at 650 °C can almost restore the initial surface morphology as well as the conductivity of the film measured by needles. An important question is now whether this "recovery" treatment can also restore the electrochemical characteristics of the diamond electrode.

 This question is answered by fig. 6.16 and 6.17, which show the cyclic voltammetry and the Mott-Schottky plot after reactive ion etching and the surface annealing treatment in hydrogen plasma. The cyclic voltammetry plot in 0.1 M H_2SO_4 is very similar to that for wet-chemical oxidation (see fig. 6.1), which becomes visible especially in the adsorption characteristics prior to the oxygen evolution reaction. Using the results of impedance spectroscopy measurements, the Mott-Schottky plot was taken and compared to that of anodic oxidation, as shown in fig. 6.17. The two curves are almost identical in most of the potential range and differ clearly from the case of argon/oxygen plasma without subsequent annealing ("recovery") treatment (see fig. 6.15). This measurement shows that the electrochemical characteristics of diamond electrodes exposed to argon/oxygen plasma can be restored by a hydrogen plasma post-treatment at high temperature and subsequent wet-chemical or anodic oxidation. It should be noted that the initial electrode characterisitcs could be restored even if the diamond surface was completely insulating after the argon/oxygen plasma process. The effect of the hydrogen plasma treatment could be a conversion of the α-carbon layer into
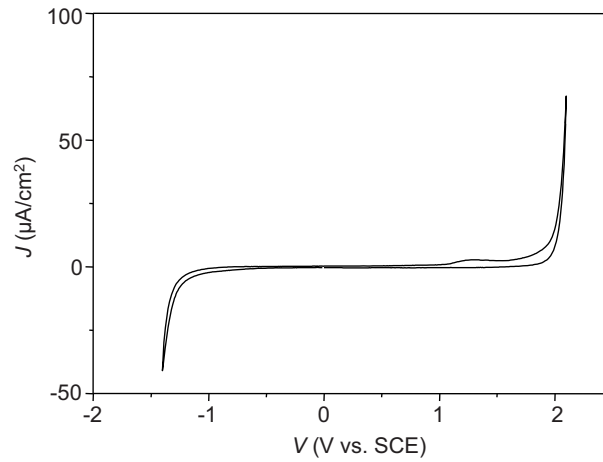
Figure 6.16: Cyclic voltammetry measurement of the diamond electrode after argon/oxygen plasma and subsequent annealing in hydrogen plasma. The measurement was taken in 0.1 H_2SO_4.
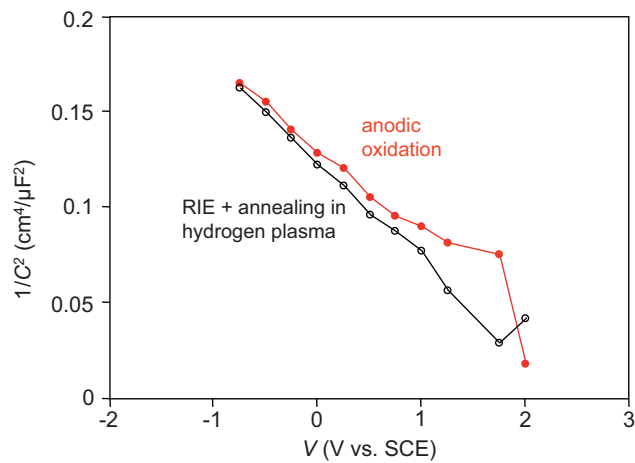
Figure 6.17: Mott-Schottky plots of single-crystal diamond after after argon/oxygen plasma (RIE) and hydrogen plasma treatment in comparison with the case of anodic oxidation

graphite with a subsequent etching of the graphite layer in the hydrogen plasma. In addition, also the defect-rich diamond layer beneath the α-carbon layer is almost completely recovered, as it was shown by XPS measurements.

6.2   Nanocrystalline diamond electrodes

The same analysis as for the single-crystal diamond electrodes was applied to nanocrystalline (NCD) electrodes after different oxidation treatments. Nanocrystalline diamond consists of diamond grains and a grain boundary network. While the grains are expected to have similar characteristics like single-crystal diamond, the grain boundary defects could have sp^2-like characteristics. The grain boundaries could provide a parasitic channel for the current transport, while the interface capacitance is dominated by the grains because they cover most of the surface area. Therefore, it might be necessary to apply a heterogenous model for the analysis of the nanocrystalline diamond electrodes.

In the following, the cases of anodic oxidation (high electronic surface barrier for single-crystal diamond) and RF oxygen plasma (relative low electronic surface barrier) will be investigated. The results will be compared with those on single-crystal diamond electrodes.

6.2.1   Anodic oxidation
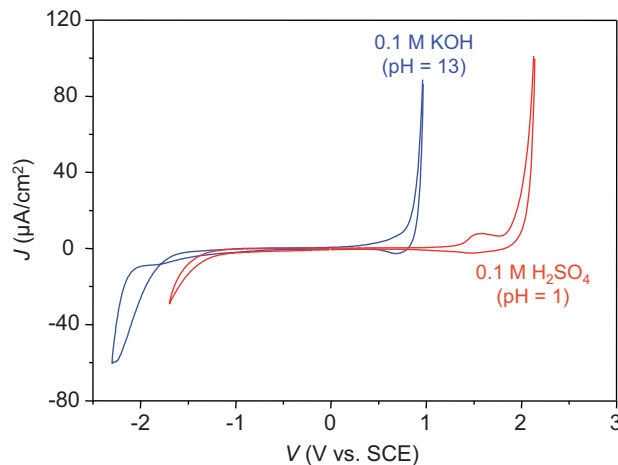
Figure 6.18: Cyclic voltammetry plots of the NCD electrode after anodic oxidation

Fig. 6.18 shows the cyclic voltammetry plots of a typical NCD electrode in 0.1 H_2SO_4 and 0.1 M KOH electrolyte. The measurement showed similar results compared to the single-crystal diamond electrodes. The potential window in the $\mu A/cm^2$ range in pH = 1 electrolyte was approx. 3.5 V with a background current below 1 $\mu A/cm^2$. Again, an adsorption peak with a maximum at +1.5 V vs. SCE was observed. The cyclic voltammetry measurements imply that the grain boundaries provide no parasitic path for the current transport.

Impedance spectroscopy measurements also showed similar results compared to single-crystal diamond. Outside the adsorption peak prior to the onset of the oxygen evolution, the impedance data could well be fitted by a single *RQ*-circuit and a small series resistance. The resistance in parallel to the CPE was again in the range of 10 MΩcm^2 and could therefore be neglected. Fig. 6.19 shows the Mott-Schottky plots in H$_2$SO$_4$, KCl and KOH electrolyte. The solid line shows again the fit corresponding to the model described in section 4.4. The
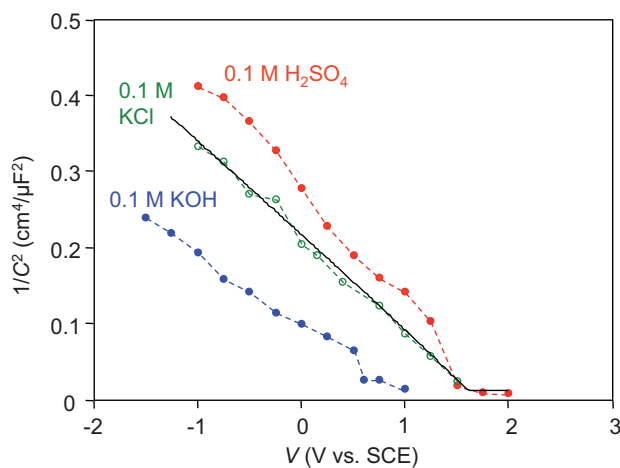
Figure 6.19: Mott-Schottky plots of the NCD electrode after anodic oxidation. The slightly different slopes of the Mott-Schottky plots are discussed in the text.

extracted doping concentration was approx. $N_A = 2.2 \times 10^{20}$cm^{-3}. Comparing the Mott-Schottky plots with those of single-crystal diamond exposed to anodic oxidation, the extrapolated flatband potential for nanocrystalline diamond was slightly smaller. Using the same analysis as above, the measurements in 0.1 H$_2$SO$_4$ and 0.1 M KCl electrolyte yielded an electronic surface barrier of approx. 1.4 eV, compared to 1.7 eV for single-crystal diamond. A possible explanation is the influence of the grain boundary defects, which might induce additional electronic surface states within the bandgap of diamond. However, especially the measurement in 0.1 H$_2$SO$_4$ showed that the slope of the Mott-Schottky plot was not absolutely constant over the whole potential range, although the doping concentration should be constant. This difference compared to single-crystal diamond electrodes might be explained by additional elements of the equivalent circuit, which could not be resolved by the impedance spectroscopy measurements and were therefore attributed to the capacitance. Such additional elements could be ascribed to the grain boundary defects. Therefore, the exact

value of the surface barrier of the NCD electrodes in H_2SO_4 has still some uncertainty.

6.2.2 RF oxygen plasma

The cyclic voltammetry characteristics of the nanocrystalline diamond electrode were significantly changed after the oxygen plasma treatment. Comparing the
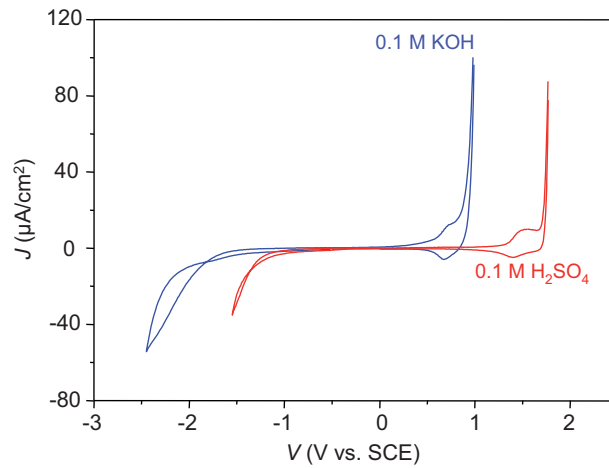
Figure 6.20: Cyclic voltammetry measurements of the nanocrystalline diamond electrode exposed to RF oxygen plasma

results after exposure to oxygen plasma (fig. 6.20) with those for anodic oxidation (fig. 6.18) or with single-crystal diamond (fig. 6.9), the onset of the anodic current was shifted to lower anodic potentials. Taking a value of 40 $\mu A/cm^2$, the corresponding potentials in 0.1 H_2SO_4 were approx. +2.1 V vs. SCE for anodic and +1.7 V vs. SCE for plasma oxidation, respectively. Similar effects were also observed in 0.1 M KOH (see fig. 6.20) and 0.1 M KCl. The origin of this effect can be understood when extending the measurement to higher anodic currents. Fig. 6.21 shows the anodic region of a measurement taken to the mA/cm^2-range of the plasma-oxidized electrode in 0.1 H_2SO_4 electrolyte. One can see that the anodic current starting at +1.7 V vs. SCE saturates at current densities above 100 $\mu A/cm^2$. For higher anodic potentials, the current density is comparable to that of a NCD electrode after anodic oxidation. Similar characteristics have been observed for single-crystal diamond electrodes modified by active metal nanoclusters [90]. This means that local defects with a limited surface area, most likely the grain boundary intercept points, are probably responsible for the an-
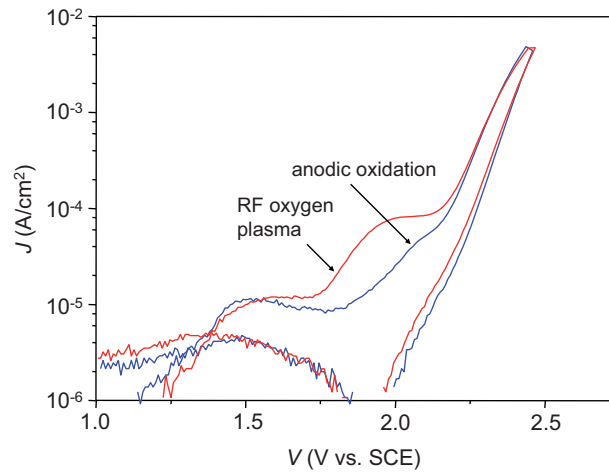
Figure 6.21: Semilogarithmic plots of the cyclic voltammetry measurements for anodic oxidation and oxygen plasma (anodic region)

odic current at $+1.7$ V vs. SCE. The oxygen plasma treatment could therefore activate the grain boundary defects.

Like in the case of single-crystal diamond, the impedance spectroscopy measurements in 0.1 M KCl revealed two separate RC-circuits, which could be ascribed to depletion- and double layer. In 0.1 H_2SO_4, these two circuits could not be clearly resolved due to the high parallel resistances. Therefore, the Mott-Schottky plots in fig. 6.23 show again the complete capacitance for 0.1 H_2SO_4 and only the depletion layer capacitance for 0.1 M KCl. The slope of the MS plot yielded a doping concentration of approx. $3 \times 10^{20} \text{cm}^{-3}$. The Mott-Schottky plot in 0.1 M KOH electrolyte is not shown since it did not allow an accurate extraction of the surface barrier. The evaluated surface barrier potential extracted from the MS plots (fig. 6.23) was approx. 1.0 eV for the NCD surface after the oxygen plasma treatment (with V_{OCP} $+0.4$ V vs. SCE for pH $= 1$), similar to the corresponding single-crystal electrode. Therefore, the depletion layer capacitance and therefore the electronic surface barrier is dominated by the grains, while the grain boundaries can influence the current across the electrode significantly.
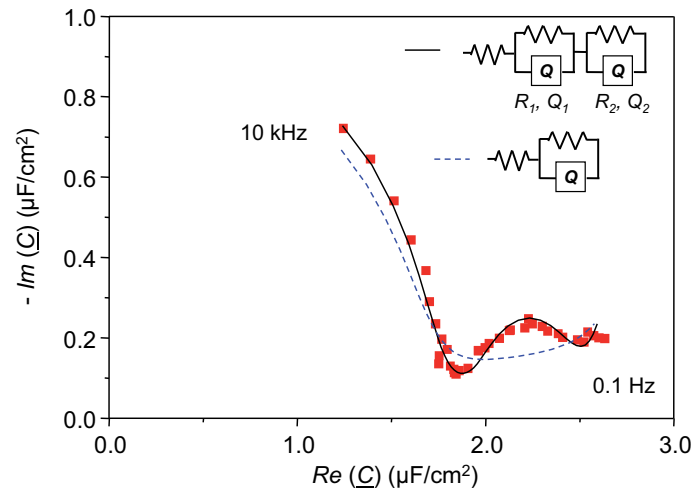
Figure 6.22: Results of impedance spectroscopy of the NCD electrode after oxygen plasma at $V = +0.0$ V vs. SCE in 0.1 M KCl electrolyte. The lines show the fits with one (dashed) and with two (full line) RQ-circuits.
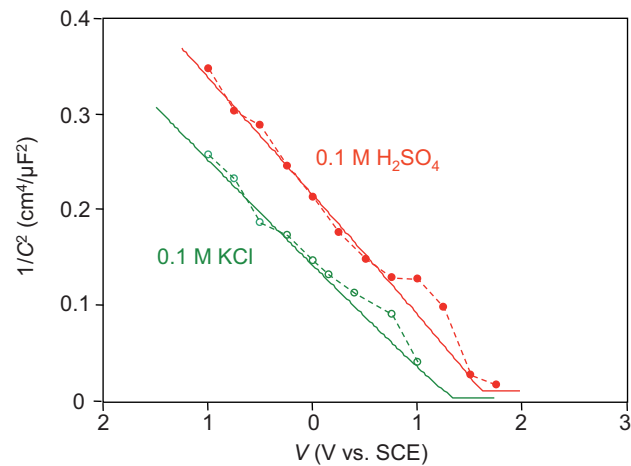
Figure 6.23: Mott-Schottky plots of the NCD electrode oxidized by RF oxygen plasma

6.3   Summary

The analysis has shown that the characteristics of oxygen-terminated diamond are sensitive to the oxidation treatment. Comparing the oxidation treatments

shown above, **anodic oxidation** induces the highest electronic surface barrier of approx. 1.7 eV for highly-doped single-crystal diamond electrodes. After **wet-chemical oxidation**, the barrier is slightly lower, but can be easily converted to the case of anodic oxidation when potentials corresponding to the regime of the oxygen evolution reaction are applied, especially in KOH electrolyte. On the other hand, the surface characteristics after anodic oxidation are extremely stable against cathodic and further anodic treatments. Therefore, anodic oxidation might be the preferred surface treatment especially when high anodic overpotentials are required. One example for such applications is the oxidation of organic compounds (see chapter 7).

The electronic surface barrier after **RF oxygen plasma** is approx. 1.0 eV and therefore significantly lower than for anodic oxidation, which could be related to a small increase of defects by the plasma process, although this increase could not be clearly resolved by the XPS analysis. This plasma treatment can be useful for the fabrication of electronic devices and electrochemical sensors when a localized oxidation is required. However, care must be taken because even a small amount of plasma-induced defects might affect the device characteristics.

An **argon/oxygen plasma** etching process which includes ion bombardment of the surface induces a very low surface barrier in the range of 0.5 eV. However, the electrochemical characteristics can be strongly influenced by the amorphous carbon layer and the defected diamond layer underneath. The damaged diamond surface might limit the performance of diamond electrodes and electronic devices subjected to this treatment. Although such process is not suitable for the surface termination, it can be used for the fabrication of structures like microelectrode arrays. In such a case, the effect of the argon/oxygen plasma etching process can be removed by a hydrogen plasma treatment at high temperature, which almost restores the characteristics of the initial diamond surface.

The characteristics of **nanocrystalline diamond** electrodes are similar to those of single-crystal electrodes. However, the grain boundaries can be activated by the RF oxygen plasma treatment, which results in an additional contribution of the anodic current in cyclic voltammetry measurements. For the case of anodic oxidation, the grain boundaries might lead to a slightly smaller electronic surface barrier compared to the case of single-crystal diamond. However, the onset potentials for the hydrogen and oxygen evolution across the entire surface and the background currents within this window do not differ significantly from the case of single-crystal diamond. Therefore, the NCD electrodes can well approach the performance of single-crystal diamond electrodes and are therefore very attractive for practical applications.

Chapter 7

Applications of Diamond Electrodes

7.1 Diamond electrodes for the ethanol oxidation

One promising field of application of diamond electrodes is the electrochemical oxidation of organic compounds, like phenol [15, 16], carboxyl acids [17], ethanol, or other substances [18, 19]. The electrochemical oxidation process can be used for the detection of these compounds, for the electrochemical synthesis of new compounds, or for waste water treatment, when toxic and non-biodegradable organic pollutants are converted into less problematic substances. The reaction products are strongly dependent on the oxidation potential and the electrode material, since the organic compounds are not always completely oxidized into CO_2. One main problem of traditional metal electrodes like platinum or ruthenium dioxide is their corrosion and the formation of intermediate products at the electrode surface, which leads to a deactivation of the electrode [91, 92, 93]. For diamond electrodes, this poisoning effect can be avoided at potentials in the range of the oxygen evolution reaction. The reason is that the organic compounds are completely oxidized by the generated hydroxyl radicals [15, 16, 17, 18]. This condition therefore requires the stability of the electrode material under anodic potentials, which makes oxygen-terminated diamond an ideal candidate for these applications.

In this chapter, the oxidation of ethanol on diamond electrodes will be discussed. For all experiments shown below, a highly boron-doped ($N_A \approx 3 \times 10^{20} cm^{-3}$) nanocrystalline diamond electrode oxidized by anodic treatment was used, since this surface termination has shown to be very stable under harsh anodic conditions.

Fig. 7.1 shows the results of cyclic voltammetry measurements in 0.1 M H_2SO_4 containing different concentrations of ethanol. The data are shown in the mA/cm^2-range and therefore at much higher current densities compared to the studies in the previous chapter. At potentials near the onset of the oxygen evolution reaction, the current increases with the ethanol concentration, as shown in

the insert. The oxygen evolution reaction itself becomes in this current range visible at potentials above $+2.25$ V vs. SCE. The dependence of the peak current on the ethanol concentration is slightly super-linear, which can be explained by the fact that the peak potential is slightly shifted to higher values with higher ethanol concentration and that the oxygen evolution reaction has therefore a slightly increasing contribution to the total current. For potentials within the window of water stability, no effect of ethanol was found. Therefore it can be concluded that hydroxyl radicals are required for the oxidation of ethanol on diamond.

The stability of the electrode activity is shown in Fig. 7.2. The graph shows the current density at a potential of $+2.25$ V vs. SCE in a solution containing 8 mM of ethanol. No decrease of the ethanol signal was observed after 90 cycles at 50 mV/s. Such measurement could be repeated without any degradation of the diamond electrode, which indicates that the electrode will stand this treatment even longer. The measurement verifies that no organic or oxide passivation layer is formed on the diamond surface during ethanol oxidation.
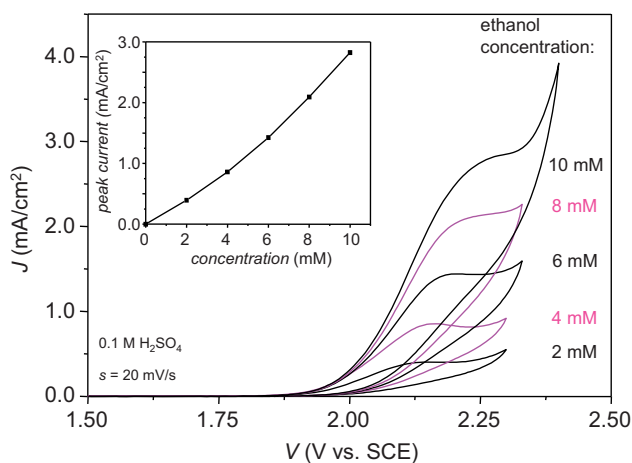
Figure 7.1: Cyclic voltammetry measurements at 20 mV/s in 0.1 M H_2SO_4 containing different ethanol concentrations. The dependence of the peak current on the ethanol concentration is shown in the insert.
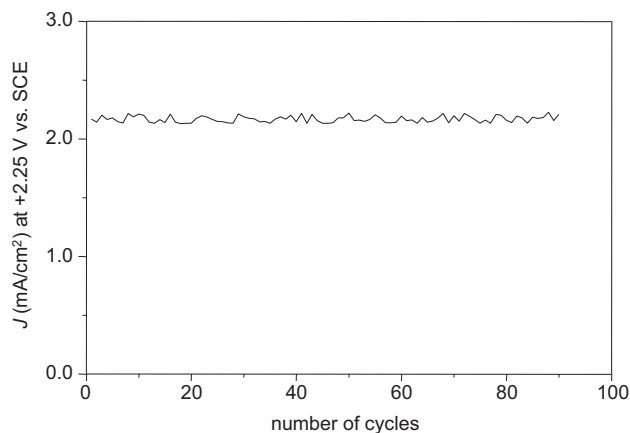
Figure 7.2: Current density of the ethanol oxidation for 90 subsequent scans of cyclic voltammetry at an ethanol concentration of 8 mM.

7.2 Diamond sub-microelectrode array

7.2.1 Introduction

The fabrication and testing of diamond-based microelectrode arrays has become a topic of large interest in diamond electrochemistry, since such structures promise high signal-to-noise ratio, the resolution of very small concentrations, and the possibility to perform static measurements. Many different processing techniques have been used for the fabrication of microelectrode arrays, including local laser ablation of the conductive diamond followed by intrinsic overgrowth and subsequent lapping down to the tops of the conductive pillars [94, 95], NCD growth on silicon or tungsten wires [96], or selective growth of conductive diamond and passivation of the large surface by silicon oxide or polyamide films [97, 98]. However, such non-diamond passivation layers will limit the stability of the microelectrode arrays in harsh electrolytes (especially alkaline solutions) or under anodic conditions, which might inhibit possible applications like the oxidation of organic compounds. In addition, the dimensions of the single microelectrodes are usually in the range of several micrometers or above. However, an optimization of the electrode characteristics requires the fabrication of micro- or nanoelectrodes with smaller dimensions (see equation 4.16).

One possible idea is to overgrow a boron-doped active layer with an insulating diamond cap layer and open the active areas by plasma etching. The active microelectrodes are defined by e-beam lithography, which enables reducing the dimensions into the range of 100 nm or below. Such an all-diamond sub-microelectrode

array is expected to combine high electrochemical stability with high sensitivity and resolution.

In this section, the device concept and the fabrication technology of the sub-microelectrode array are described. One important aspect is the influence of the plasma etching process on the device characteristics. The characteristics of the diamond electrode with cap layer before and after etching of the single sub-microelectrodes are investigated in electrolytes without redox couples and compared to the case of a highly boron-doped electrode. Finally, the fabricated ultra-microelectrode array is characterized by measurements in electrolytes containing redox couples.

7.2.2 Microelectrode array fabrication

The most obvious solution for the passivation layer of the microelectrode array would be a film of intrinsic diamond. An interesting alternative is a nitrogen-doped cap layer, resulting in a pn-junction close to the electrode surface. As mentioned in chapter 3, nitrogen is a deep donor in diamond with the activation energy $E_{D,N} = 1.7$ eV. Therefore, the nitrogen donor will not be activated at room temperature, and the cap layer will be insulating and thus passivating the surface. In addition, the pn-junction close to the surface will form an additional barrier and therefore block any DC current across the large surface. Fig. 7.3(a) schematically shows the band diagram of a boron-doped electrode with n-doped cap layer in contact with an electrolyte. The band bending at the diamond-electrolyte interface is not clear yet, since nitrogen-doped electrodes have been rarely investigated. The Fermi level might be pinned at approx. 1.7 eV above the valence band edge, as indicated by the dashed line. If the cap layer thickness is large enough that is does not limit the width of the depletion layer, the barrier at the pn-junction can reach a value of up to 3.8 eV. The barrier between electrolyte and the boron-doped layer is in this case similar to a camel diode [99, 100]. In the present case, the barrier is lower due to the small cap layer thickness (see below).

Fig. 7.3(b) schenatically shows the fabricated device . The boron-doped active layer and the nitrogen-doped cap layer were grown on the polished surface of a 100-oriented HTHP substrate by MWCVD, similar to the boron-doped single crystal diamond electrodes investigated in chapter 6. The thickness of the boron-doped layer was approx. 50 nm and the boron concentration approx. 4×10^{20} cm^{-3}, which was verified by capacitance-voltage measurements in electrolytes. The nitrogen-doped cap layer with a thickness of approx. 20 nm was grown on top of the boron-doped diamond film by the same method using nitrogen gas as the doping source, where the CVD reactor had been cleaned prior to the n-layer growth to avoid unintentional boron contamination. The doping concentration in the nitrogen-doped cap layer estimated from the growth parameters was in the range of 5×10^{18} cm^{-3} [84]. Taking these values into account, the expected width

(a)   (b)
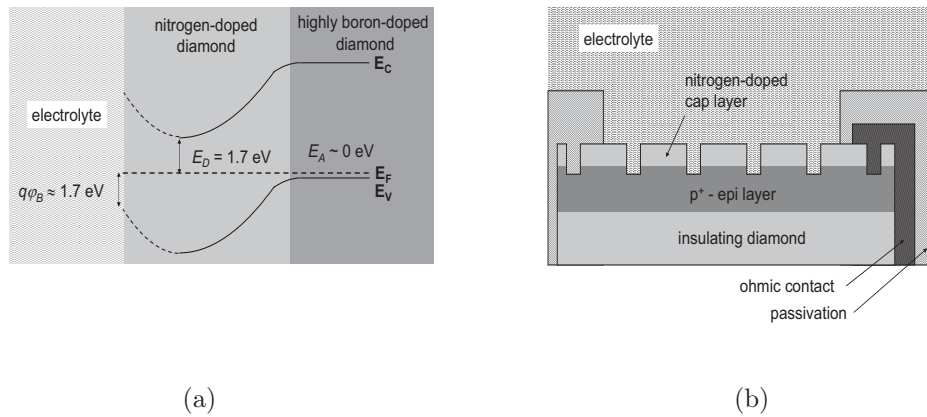
Figure 7.3: (a) schematical band diagram of a pn-junction close to the electrode surface. The Fermi level is assumed to be pinned at 1.7 eV above the valence band edge, as indicated by the dashed line.(b) scheme of the fabricated sub-microelectrode array.

(a)   (b)
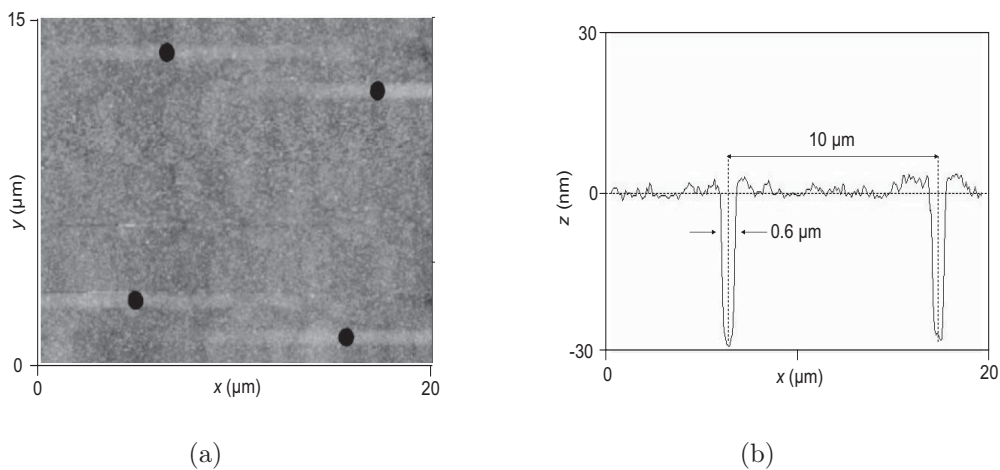
Figure 7.4: AFM image of the fabricated sub-microelectrode array. (a) top view, (b) cross section.

of the depletion layer within the n-doped cap layer would be above 20 nm, which means that the cap layer is completely depleted.

The etching of the individual ultra-microelectrode openings through the nitrogen-doped layer was achieved using a polymethyl methacrylate (PMMA) photoresist mask structured by e-beam lithography. The etching of diamond was performed using the argon/oxygen plasma process described in the previous chapters. It was

shown that the Ar/O_2 plasma process induces a thin amorphous carbon layer of non-diamond phases, which limits the electrode performance. Therefore, the microelectrode array was exposed to the hydrogen plasma treatment at approx. 700 °C after the etching process. Fig. 7.4(a) and 7.4(b) show the results of AFM measurements for the fabricated sub-microelectrode array. The holes in the cap layer were approx. 500 nm in diameter with a periodical distance of 10 μm. This corresponds to a surface coverage of approx. 0.25 %. As shown by the cross-section in Fig. 1b, the depth of the holes was approx. 30 nm, which means that the etching provided a direct contact to the highly-boron doped diamond layer.

7.2.3   Characterization in 0.1 M H_2SO_4

The characteristics of the ultra-microelectrode array were investigated in 0.1 M H_2SO_4 without any redox couples. The results were compared to those for the boron-doped electrode before the growth of the nitrogen-doped cap layer and to the electrode with surface cap layer but before the etching process for the active microelectrodes. The cyclic voltammetry measurements of these three structures are shown in Fig. 7.5(a) and 7.5(b) in linear and semilogarithmic scale for a scan rate of 20 mV/s.
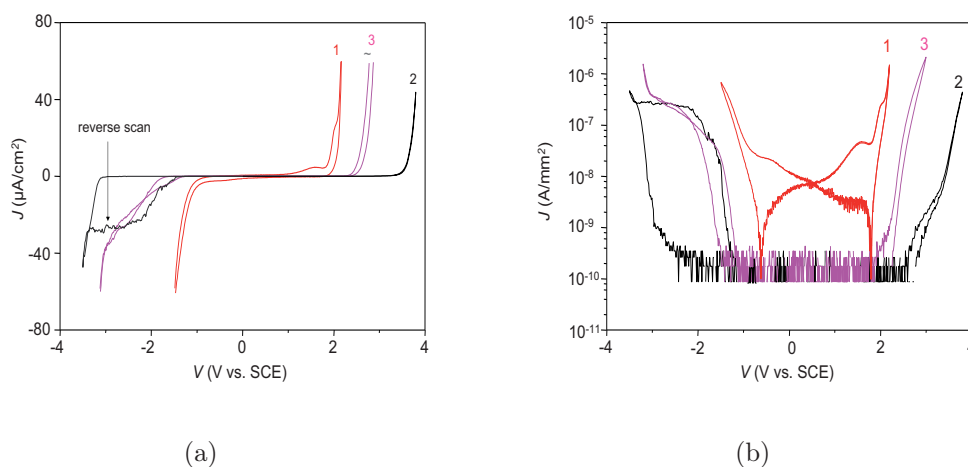
Figure 7.5: Cyclic voltammetry measurements of a highly-boron-doped electrode (curve 1), the electrode overgrown with the nitrogen-doped cap layer (curve 2), and the fabricated sub-microelectrode array (curve 3). (a) linear, (b) semilogarithmic scale.

The boron-doped electrode (curve 1) showed typical characteristics as discussed in chapter 6. The overgrowth with the nitrogen-doped cap layer had two effects: First, the measured (electrical) potential window was enlarged to approx. 7 V. Both the hydrogen- and the oxygen evolution were shifted to higher potentials,

which is a difference compared to electrodes with intrinsic (unintentionally lowly boron-doped) electrodes, where only the onset of the hydrogen evolution is significantly shifted [101, 102]. The shift of the onset potential for the oxygen evolution reaction clearly shows the presence of the pn-junction close to the surface. Here it is important to note that the potential window of 7 V in the $\mu A/cm^2$-range is due to the fact that the potential partially drops across the pn-junction, but not across the diamond-electrolyte interface. Assuming an electric breakdown field for diamond of 10 MV/cm [103] the breakdown voltage for a 20 nm-thick cap layer should be approx. -20 V vs. SCE. Besides, the expected flatband potential for the pn-junction should be approx. +4.2 V vs. SCE, taking the theoretical barrier at the pn-junction of 3.8 eV and the OCP value of approx. +0.4 V vs. SCE into account. Therefore, an even larger measured potential window could have been expected. This means that the energy barrier at the pn-junction is below 3.8 eV, which can be explained by the relative thin nitrogen-doped cap layer. Besides, the anodic and cathodic currents for the pn-electrode could still be dominated by local current paths due to defects in the diamond material.

The second effect of the surface cap layer is a reduction of the background current down to the detection limit of approx. 10 nA/cm^2. This can be explained by the passivation of defects and by the reduction of the interface capacitance. Impedance spectroscopy measurements showed that the interface capacitance was in the range of 0.3 $\mu F/cm^2$, which correlates with a cap layer thickness of approx. 18 nm. This capacitance value corresponds to a capacitive background current of approx. 7 nA/cm^2, which correlates with the results from the measurements. In addition, no current peak prior to the onset of the anodic current was observed for the pn-electrode. However, a strong hysteresis was observed after cycling to the potential range of the hydrogen evolution, which might be related to slow dssorption processes.

After etching of the sub-microelectrode areas, the background current in the inactive region was not significantly changed compared to the value of the cap-layer electrode. This can be related to the low ratio between the areas of the microelectrodes and the total surface. However, the onset of the hydrogen- and the oxygen evolution reactions on the microelectrode areas could be clearly resolved. The semilogarithmic plot shown in Fig. 2b shows that the anodic current in the nA/cm^2 range starts to increase for the sub-microelectrode array at approx. +2.0 V vs. SCE, which is the onset potential for the oxygen evolution on boron-doped diamond electrodes. Besides, the ratio between the anodic currents in the range of the oxygen evolution between the unpassivated boron-doped diamond electrode (curve 1) and the sub-microelectrode array (curve 3) was approx. 1/400 and therefore close to the ratio of the active surfaces.

A more detailed analysis could be obtained from the impedance measurements shown in Fig. 7.6(a) and 7.6(b). In these plots, the values for the interface
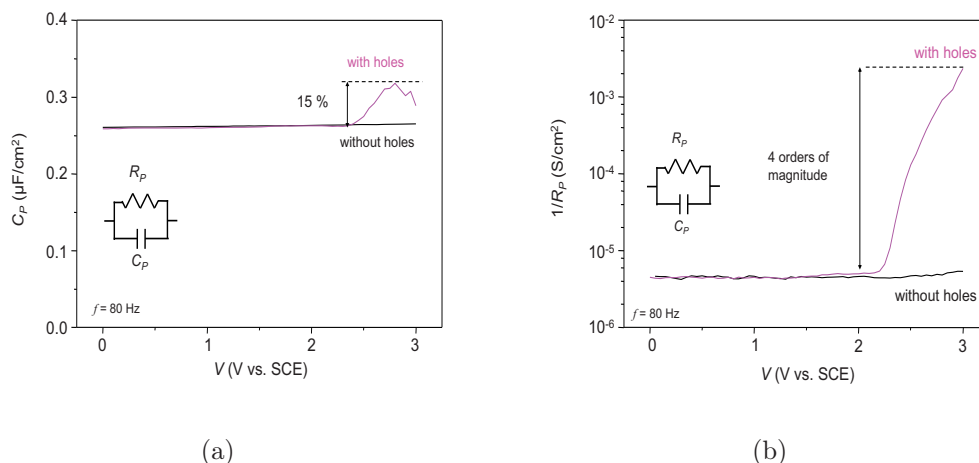
Figure 7.6: Results of the impedance measurements for the electrode with cap layer but without holes (curve 1) and for the sub-microelectrode array (curve 2) in 0.1 M H_2SO_4. (a) capacitance, (b) real part of the admittance. The equivalent circuit used for the analysis is shown in the insert.

capacitance and the parallel admittance are compared for the electrode with n-doped cap layer (without holes) and for the sub-microelectrode array. The equivalent circuit used for this analysis is shown in the insert. The contact resistance of the electrode was determined by impedance spectroscopy measurements and subtracted from the total impedance prior to this analysis. Up to a potential of approx. $+2.0$ V vs. SCE, there is no significant difference between these two electrodes. At higher anodic potentials, the real part of the admittance increases by four orders of magnitude, while the capacitance is only slightly increased by approx. 15%. This clearly shows that the current across the microelectrode array is determined by the local active areas produced by etching, while the interface capacitance is dominated by the large surface. Since this capacitance determines the background current of the sub-microelectrode array in electroanalytical applications, these results promise a high signal-to-noise ratio for the fabricated ultra-microelectrode array.

7.2.4 Response to redox couples

The response of the sub-microelectrode array to the $Fe(CN)_6^{3-/4-}$ redox couple is shown by the cyclic voltammetry plot in Fig. 7.7. The measurement was performed in 0.1 M KCl + 10 mM $K_4Fe(CN)_6^{4-}$ (only the reduced species was apparent at the beginning) at scan rates between 20 mV/s and 1 V/s. In this case,

the absolute values of the current are shown, because there is no homogenous current density across the entire surface. The cyclic voltammetry showed typical
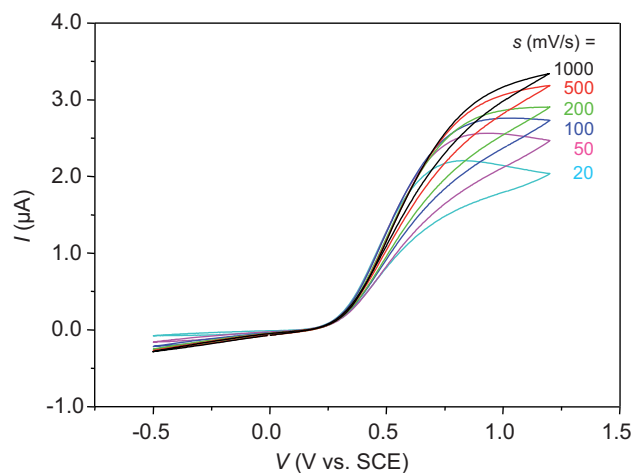
Figure 7.7: Cyclic voltammetry measurements of the sub-microelectrode array in 0.1 M KCl + 10 mM Fe(CN)$_6^{4-}$ at various scan rates.

microelectrode characteristics, although the linear diffusion appeared not to be completely eliminated. The cyclic voltammetry measurements showed a slight scan rate dependence. For an ideal microelectrode array, the current should be scan-rate independent. However, the obtained cyclic voltamogram differs significantly from corresponding results for planar electrodes (see fig. 4.9). The limiting current, which should be in the ideal case scan-rate independent, varied from 2.2 μA for 20 mV/s to 3.3 μA for 1 V/s. This corresponds to a factor of 1.5. However, these variations are still very small compared to that of a planar large-area electrode. In that case, the peak current would be proportional to the square root of the scan rate, resulting in a factor of 7.1 (see also fig. 4.9). Therefore, hemispherical diffusion is dominating the mass transport.

The limiting currents are also in good accordance with the values expected for a microelectrode array structure. Taking equation 4.16 with $c_b = 10$ mM, $D = 6 \times 10^{-6}$ cm^2/s (diffusion constant for Fe(CN)$_6^{3-/4-}$ [104]) and an active surface area of 0.007 cm$^2 \times 0.25$ %, the limiting current should be approx. 4.2 μA, which is close to the value measured for high scan rates. Normalized to the surface of the microelectrode openings, the current density is in the range of 0.2 A/cm^2, which is about two orders of magnitude higher than for a large-area electrode (see fig. 4.9). This means that the signal current is significantly less suppressed than the background current, leading to an improved signal-to-noise ratio.
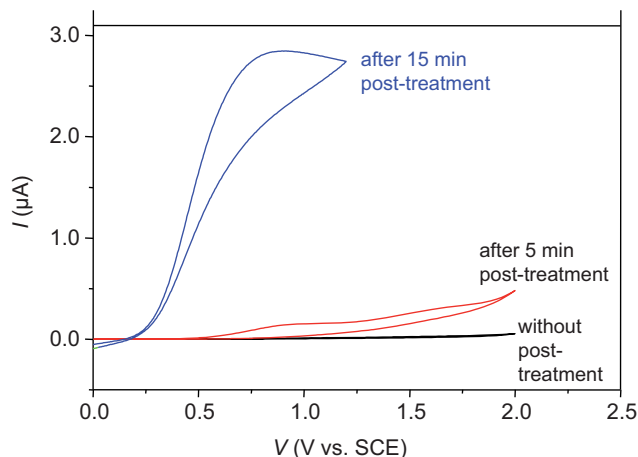
Figure 7.8: Redox characteristics at $s = 100$ mV/s of the sub-MEA without recovery treatment and after 5 and 15 min recovery treatment

Finally, the importance of the recovery treatment after the argon/oxygen plasma process will be shown. In fig. 7.8, the cyclic voltammetry curve at 100 mV/s from fig. 7.7 is compared with corresponding measurements directly after etching and after a short hydrogen plasma treatment at 700 °C. It can be clearly seen that the hydrogen plasma treatment is essential to achieve a good electrode performance. In summary, the sub-microelectrode array has shown attractive characteristics like high signal current density and low scan-rate dependence. Such devices could be very attractive for the electroanalysis in harsh environments or for bio-chemical applications.

7.3 Diamond electrodes with metal particles

7.3.1 Introduction

Boron-doped diamond electrodes can be also a promising support for catalytically active metal particles. Such electrode structures have been already used for different applications like methanol oxidation [74, 105, 106] or the oxygen reduction [107]. Several different techniques for the deposition of such particles have been demonstrated, like electrodeposition in electrolytes [105, 106, 107], microemulsion [74], or local electrical discharge [90].

One important requirement these electrodes is that the diamond substrate must provide a low-resistive path to the metal particles. In the case of a moderately doped electrode, the contact between the metal particles and the diamond can show Schottky diode-like characterisitcs due to the depletion layer

on the oxygen-terminated surface, which is expected to suppress the catalytic activity of these particles. For a highly-doped electrode, this depletion layer is short-cutted due to tunnelling, leading to a very low contact resistance. In addition, the depletion layer on the free surface can penetrate sidewise below the nanoparticles and pinch-off the contact. This effect has been analyzed in detail for single-crystal diamond electrodes [102]. Again, it leads to the conclusion that in the case of single-crytsal diamond electrodes, a high doping concentration is required. On the other hand, a high doping concentration results also in a (for diamond electrodes) relative high background current. This background current from the areas surrounding the metal particles could be reduced by using an intrinsic cap layer on top of a highly doped diamond substrate.

A possible solution for the case of nanocrystalline diamond has been published in [101] and will be shown in the following. The main idea is that the grain boundaries might provide a low-resistive path even across a low-doped cap layer.

7.3.2 Characterization of the electrodes

To analyse this issue, two nanocrystalline diamond electrodes with Au nanopraticles will be compared: One highly boron-doped (p^+) electrode and one highly boron-doped electrode with a low-doped (p^+/p^-) cap layer. The doping concentrations of the highly- and the low-doped cap layer were in the range of 3×10^{20} cm^{-3} and 10^{17} cm^{-3}, respectively.

Both electrodes were oxidized by the wet-chemical treatment. After this, both samples were covered by Au paricles by electrodeposition in a gold galvanic solution (Microfab Au 100 by Enthone B.V.). The electrodeposition on the highly doped electrode was performed at -0.6 V vs. SCE until an amount of transferred charge of approx. 1mC/cm^2 was reached. For the sample with the low-doped cap layer, a potential of approx. -2.0 V vs. SCE was required to acieve a similar surface coverage with Au particles. The corresponding SEM images are shown in fig. 7.9(a) and 7.9(b).

From the SEM images, two aspects can be observed: First, the surface coverage is low (1 % or less) compared to data reported literature [105, 106, 107], which can be explained by different deposition parameters. Second, the Au particles grow preferential at intercept points of grain boundaries, which is important for the discussion below. The average particle size was approx. 100 nm.

The results of cyclic voltammetry measurements before and after the deposition of the nanoparticles are shown in fig. 7.10(a) and 7.10(b). As expected, the low-doped cap layer reduced the background current of the electrode without nanoparticles significantly, similar to the cap layer of the microeelctrode array shown in the previous section. Besides, the onset of the hydrogen evolution was shifted to more negative potentials, which can be explained by the additional series resistance related to the depleted cap layer. The oxygen evolution was only

(a)   (b)
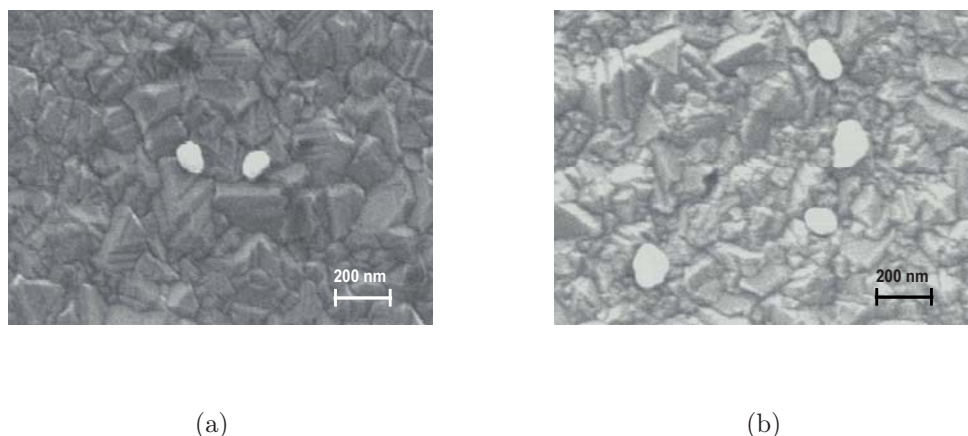
Figure 7.9: SEM images of (a) the p^+ electrode and (b) p^+/p^- electrode with Au nanoclusters

(a)   (b)
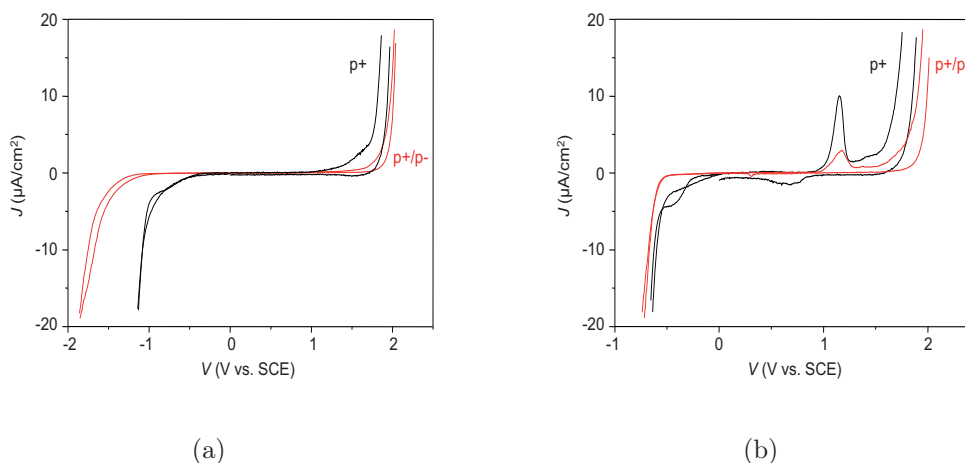
Figure 7.10: Cyclic voltammograms of the p+ and the p+/p- electrode (a) before and (b) after the deposition of the Au nanoparticles. The scan rate was 20 mV/s, the electrolyte 0.1 M H_2SO_4.

slightly affected, which is the main difference compared to the n-doped cap layer of the microelectrode array shown in section 7.2.

After the deposition of the Au pariicles, the electrodes showed a current peak at around +1.15 V vs. SCE which can be ascribed to the formation of gold oxide or the sulphate adsorption [108, 109]. On gold electrodes, similar peaks have been observed at the same potential [108, 109]. For the p^+ electrode, the coincidence

of the peak can be explained by the tunnelling between the diamond and the gold particles. However, tunnelling cannot be expected in the case of the p$^+$/p$^-$ electrode. A reasonable explanation is therefore that the grain boundaries provide the low-resistive path to the metal particles. This idea is supported by the fact that similar experiments on single-crystal diamond showed a shift of the same peak to higher anodic potentials for electrodes with a low-doped cap layer [102].

(a)   (b)
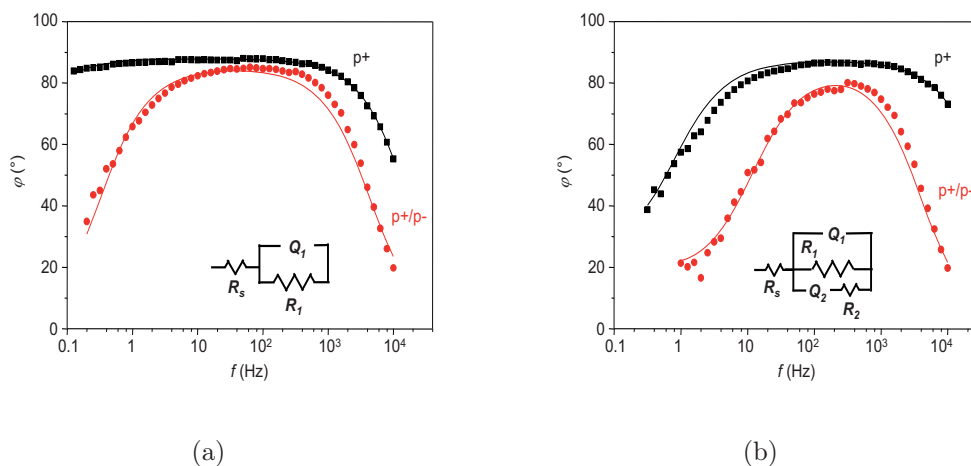
Figure 7.11: Impedance spectroscopy measurements of the p+ and the p+/p-electrode (a) before and (b) after the deposition of the Au nanoparticles at the potential of +1.15 V vs. SCE.

More details on these electrode structures were obtained from impedance spectroscopy measurements at the peak potential of +1.15 V vs. SCE. The Bode (phase) plots of the two electrodes before and after the deposition of the gold particles are shown in fig. 7.11(a) and 7.11(b) and in the data table 7.1. Before the gold deposition, the data could be ftted by a single RQ-element, where the CPE represents the depletion layer and the double layer in series. For the p$^+$/p$^-$ electrode, the value of approx. 80 nF/cm^2 correlates with the expected cap layer thickness of 60 nm. In both cases, the parallel resistance was in the MΩcm^2-range. After the deposition of the Au particles, the impedance data could be fitted by the modified equivalent circuit containing an additional RQ-series connection in parallel to the other two elements (see insert of fig. 7.11(b)). The values of Q_1 and R_1 were not significantly changed by the presence of the metal clusters due to the small surface coverage. The new elements R_2 and Q_2 can be attributed to electrochemical processes on the gold surfaces. This is supported by the value of the corresponding n-factors, which are close to that of a Warburg element. The resistance R_2 represents therefore the charge-transfer resistance of the reaction on the gold particles.

At potentials outside the current peak observed in the cyclic voltammetry, the impedance data were not affected by the Au particles.

	R_1 $(M\Omega cm^2)$	C_1 $(\mu F/cm^2)$	R_2 $(M\Omega cm^2)$	Q_2 $(\mu S \cdot s^n/cm^2)$	n_2
			without Au particles		
p+	5.3	2.62	-	-	-
p+/p-	6.2	0.082	-	-	-
			with Au particles		
p+	5.0	2.32	100	15.1	0.50
p+/p-	5.5	0.083	198	3.2	0.40

Table 7.1: Fit parameters of for the impedance spectroscopy measurements

7.3.3 Equivalent circuit of the electrodes covered by Au nanopraticles

Figure 7.12: Schematic cross-section of an O-terminated NCD electrode with low-doped cap layer and Au particles, including the equivalent circuit of the interface. The key elements are marked in black colour.

A schematic cross-section of the diamond electrode with low-doped cap layer and covered by Au nanoparticles and the corresponding equivalent circuit are

shown in fig. 7.12. On most of the total surface area (where no Au particles are apparent), the equivalent circuit contains elements corresponding to depletion- and double layer, where the parallel resitances can be neglected (see fig. 4.7(b) and 4.7(c)). Since the depletion (cap layer) capacitance is much smaller than the double layer capacitance, the latter one can be also neglected. Therefore, the surface which is not covered by Au nanoprticles can be modelled by a single capacitance representing the low-doped cap layer. Concerning the Au particles, a common equivalent circuit would be a series connection of charge-transfer resistance and Warburg element in parallel to the double-layer capacitance $C_{DL,Au}$ related to the Au surface (see fig. 7.12). Since the surface coverage with the particles is very low, the value $C_{DL,Au}$ can be neglected. As shown by the previous experiments, the resistance R_{GB} corresponding to the grain boundaries is small compared to the chatrge transfer resistance R_{CT}. This results in the equivalent circuit which has been resolved by the impedance spectroscopy measurements, containing the cap layer capacitance C_{cap} (Q_1 in the insert of fig. 7.11(b)), the charge transfer resistance R_{CT} and the Warburg element W related to the activity of the nanoparticles.

The optimiziation of such electrodes is a trade-off between the cap layer thickness (which influences C_{cap} and therefore the background current), the doping and structure of the diamond material (influencing R_{GB}), and the choice of the metal particles (R_{CT}).

Chapter 8

Characterization of III-Nitrides

8.1 Introduction

The III-nitride semiconductors aluminium nitride, gallium nitride and indium nitride are are widely used for electronic and optical applications. Using alloys like AlGaN, AlInN, or InGaN, is is possible to vary the bandgap between approx. 0.7 eV for InN and 6.2 eV for AlN ("bandgap-engineering"). An important characteristic of the III-nitrides is their spontaneous polarization. This arises from the polar gallium- (indium-, aluminum-) nitrogen bonds due to the high electronegativity of nitrogen and from the hexagonal wurzite crystal structure [110]. The lattice parameters of the III-nitride crystal structure differ from the values for the ideal wurzite structure. Therefore, the microscopic dipoles do not compensate each other, which leads to a macroscopic polarization. At the interfaces of heterostructures like AlGaN/GaN, the difference in polarization induces a fixed polarization charge, which is compensated by mobile charge carriers, leading to a two-dimensional channel. This is the concept for heterostructure FETs (high electron mobility transistors, HEMTs) based on III-nitrides for high-power and high-temperature applications. E.g., HEMT structures based on the lattice-matched $In_{0.17}Al_{0.83}N/GaN$ heterostructure have shown high current densities even for thin InAlN-layers and FET operation at 1000 °C in vacuum [111].

The III-nitride semiconductors are also widely investigated for electrochemical applications, especially for pH sensing [112, 113, 114, 115, 116], since they are also considered to be chemically stable. Usually, the surface is covered by a thin oxide layer (which can be the native or a foreign oxide) for pH sensitivity. However, it has been shown that the III-nitrides can be oxidized under harsh anodic conditions [117, 118, 119], leading to a degradation of the devices. This bulk oxidation limits the possible applications to low overpotentials.

In this part, the electrochemical characteristics of gallium nitride and indium nitride and the effect of anodic oxidation on the characterisitcs of electrodes

made of these materials will be shortly discussed and compared to the case of oxygen-terminated and boron-doped diamond.

8.2　Gallium nitride

The results of cyclic voltammetry and impedance spectroscopy measurements 0.1 M H_2SO_4 for the initial and the anodically oxidized GaN electrode are shown in Fig. 8.1 and 8.2, respectively. The GaN film was n-doped by silicon with a doping concentration in the range of $N_D = 7 \times 10^{18}$ cm^{-3}, as verified by the Mott-Schottky plot for the initial GaN electrode. For such doping concentration, the influence of the double layer capacitance could be neglected in first approximation.
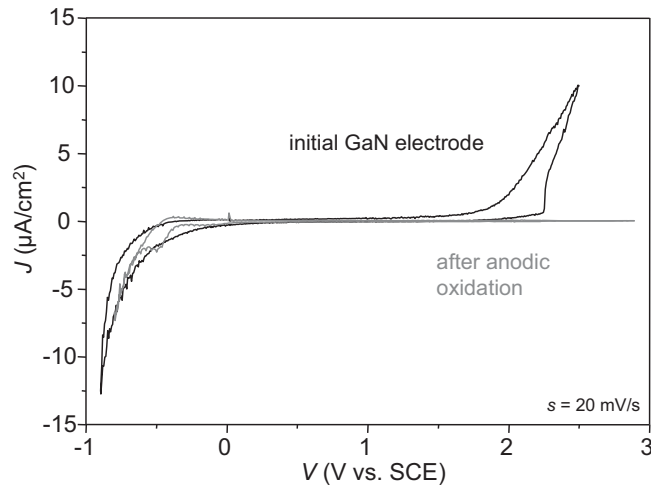
Figure 8.1: Cyclic voltammetry measurements of a n-doped GaN electrode in 0.1MH_2SO_4 before and after anodic oxidation in 0.1 M KOH

Before anodic polarization, the electrode showed a wide potential window of 2.5 - 3.0 V, which is slightly smaller compared to the case of diamond, and low background currents. The Mott-Schottky plot showed a linear slope corresponding to the doping concentration and an intercept with the potential-axis at approx. -0.8 V vs. SCE. The values for the capacitance were obtained from impedance spectroscopy measurements and the data fitting using the equivalent circuit shown in the insert of fig. 8.2. The parallel RQ-branch might be again related to some background activity or to defects in the GaN layer. Here one should mention the positive slope of the Mott-Schottky plot due to the n-type doping, where the p-doped diamond electrodes showed a negative slope in the Mott-Schottky plots.

The n-type doping also implies that for GaN an upwards and not a downwards band bending corresponds to depletion of the surface. The flatband potential of approx. -0.8 V vs. SCE and the measured OCP value of +0.4 V vs. SCE corresponded to an upwards surface band bending of approx. 1.1 eV, estimating that the Fermi level in the GaN bulk is located 100 mV below the conduction band edge. This surface barrier is consistent with values obtained for GaN by Kelvin force microscopy [120, 121].
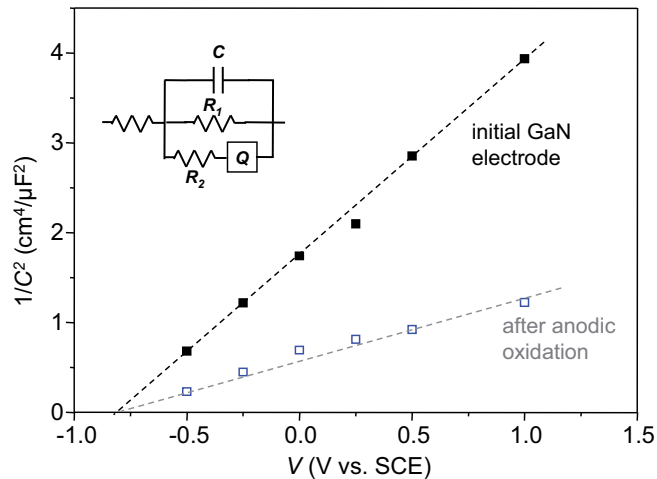
Figure 8.2: Mott-Schottky plots of the n-doped GaN electrode in 0.1 M H_2SO_4 before and after anodic oxidation in 0.1 M KOH

The anodic oxidation process did not induce any changes in the surface morphology, as measured by AFM. However, the electrochemical characteristics of the GaN electrode were drastically changed after anodic oxidation. In the cyclic voltammetry plot, the oxygen evolution reaction was completely suppressed (curve 2 in fig. 8.1). This could be explained by the formation of a thin oxide layer by the anodic treatment, which is consistent to results shown in literature [119, 122]. Here it should be noted that the anodic oxidation discussed in this section was performed without illumination which is often used for photo-electrochemical oxidation or etching of III-Nitrides.

The anodic oxidation also affected the impedance characterisitcs of the GaN-electrolyte interface. Howerver, a detailed analysis of the equivalent circuit was not possible any more, because the single elements could not be clearly ascribed to depletion- and double layer. Taking the capacitance data from the equivalent circuit (analyzed again by impedance spectroscopy) shown in the insert, the Mott-Schottky plot showed a different slope compared to the initial electrode characteristics, although the doping concentration must be constant. The capacitance data were determined from impedance spectroscopy measurements using

the equivalent circuit shown in the insert. These electrode characteristics might be explained by inhomogeneous surface properties due to a preferential oxidation at defects (see also section 8.3).

All changes induced by anodic oxidation were irreversible. The initial characteristics could not be recovered, e.g. by a cathodic treatment.

In summary, these measurements show that GaN electrodes show a large potential window and low background currents similar to diamond electrodes, but they are not stable under harsh anodic conditions. The anodic treatment likely induces a thin oxide layer suppressing the oxygen evolution reaction and therefore also other reactions in the anodic regime. Therefore, GaN electrodes cannot be used for amperometric measurements in the anodic region, e.g. for the detection of organic compounds.

8.3   Indium nitride

The low-bandgap semiconductor indium nitride ($E_g = 0.7$ eV) has attracted much attention due to its electron accumulation layer close to the surface, corresponding to a downwards band bending of 0.6-0.9 eV [123, 124]. The sheet carrier density in this accumulation layer has been estimated to be in the range of 2×10^{13} cm^{-3}. In addition, even nominally undoped InN films have a bulk electron concentration in the range of 10^{18} cm^{-3}. The surface conductive layer may be interesting for chemical sensing applications [125, 126], but has until now inhibited the fabrication of electronic devices on InN, since Schottky contacts on this material are not possible. Electronic devices on InN are expected to be very attractive for high-frequency applications due to the high predicted electron mobility of up to 12000 cm^2/Vs.

The following investigations have already been discussed in detail in [118]. The characterized InN layer was grown (Cornell University, USA) by molecular beam epitaxy (MBE) on a GaN buffer layer on a sapphire substrate with an AlN interlayer (see Fig. 8.3(a)). The layer was n-doped with silicon and a donor concentration of approx. 1×10^{19} cm^{-3}. Fig. 8.3(a) and 8.3(b) show the results of transmission electron microscopy measurements after the anodic oxidation process. The measurement showed that the anodic treatment resulted in an inhomogeneous oxide layer on the InN surface. Although the oxide thickness was significantly higher around thoughts or other defects, the complete surface was covered at least with a thin oxide layer of approx. 5 nm in thickness. The TEM measurements revealed also a pore-like structure of the oxide layer, which was similar to results for oxide layers on GaN by photo-anodic oxidation [119]. According to this investigation, the pores could be ascribed to nitrogen gas formed during the oxidation process, which is trapped into the oxide.

The electrochemical characterization of the InN electrodes were performed in a pH = 7 buffer solution. The reason was that the oxidized InN electrode was

(a)   (b)
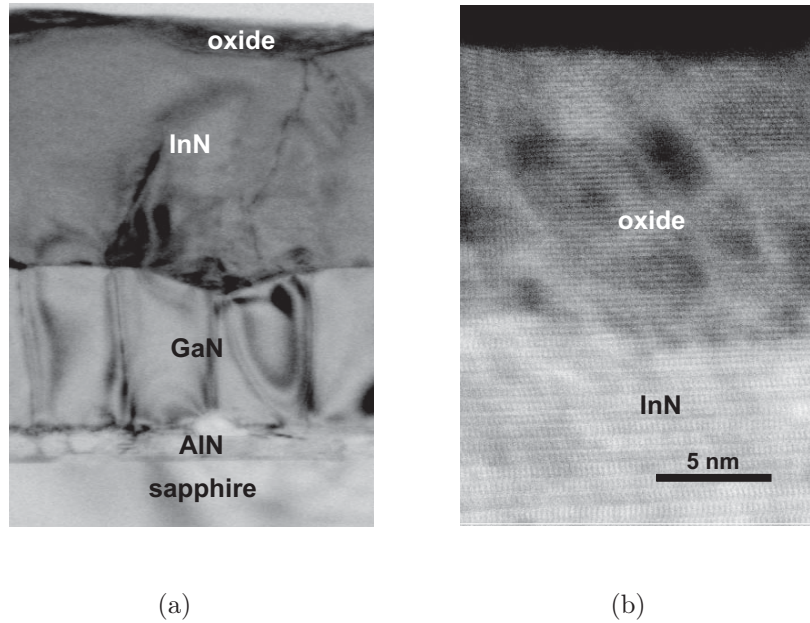
Figure 8.3: TEM images of the anodically oxidized InN electrode (measured by A. Chuvilin and U. Kaiser, Electron Microscopy Group of Materials Science, Ulm University)

not completely stable in 0.1 M H_2SO_4. Fig. 8.4 shows the cyclic voltammetry measurements for the n-doped ($N_D \approx 1 \times 10^{19}$ cm^{-3}) InN electrodes before and after anodic oxidation. The initial electrode showed a potential window of approx. 2 V in the μA/cm^2-range and low background currents of approx. 0.2 to 0.5 μA/cm^2. The potential window was therefore smaller than for GaN or diamond. The small current peak at -0.8 V vs. SCE could be ascribed to a reduction of the oxide layer which is expected also on the initial surface. This behavior was similar to that of InP electrodes and could be explained by partial decomposition of the electrode material [127, 128]. Anodic oxidation of the InN electrode resulted in an increase of the background current after polarizing the electrode to cathodic potentials. The oxidized InN electrode showed also a shift of the onset of the oxygen evolution reaction to higher anodic potentials, which could be expected for a surface covered by an oxide layer. However, this effect was less pronounced then for GaN, where the oxygen evolution was completely suppressed. Besides, the hydrogen evolution was nearly not affected. This might indicate a decomposition of the oxide at cathodic potentials or that the oxide layer is transparent for the diffusion of ions, which correlates with the pore-like structure revealed by TEM measurements.
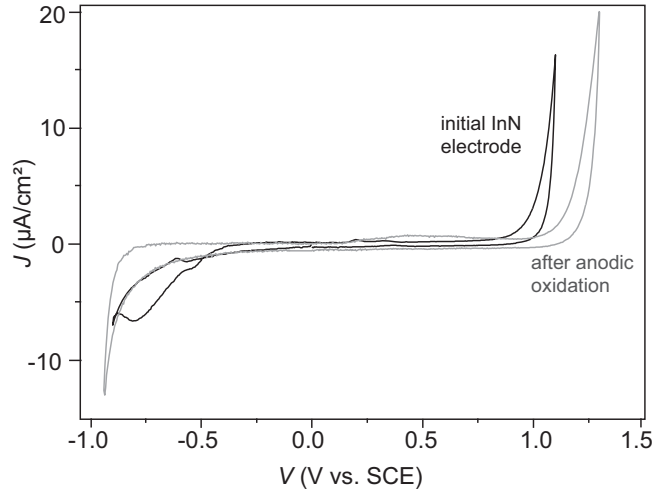
Figure 8.4: Cyclic voltammetry plots of the n-doped InN electrode in 0.1 M H$_2$SO$_4$

Impedance spectroscopy measurements of the initial InN electrode revealed that the impedance could be fitted by two RC-circuits in series. One RC-circuit could be clearly ascribed to the semiconductor, the second one either to the double layer or to a thin surface oxide which is expected to be present even on the "as-grown" (and air-exposed) surface. Again, the parallel resistances were in the M$\Omega \times$ cm^2 range within the potential window. The Mott-Schottky plots of the initial and oxidized InN electrodes are shown in fig. 8.5(a). For the initial electrode, the slope of the Mott-Schottky plot was not constant, which can be ascribed to the surface accumulation layer. Using the equation

$$n(x) = \frac{C^3}{q\varepsilon_0\varepsilon_r \frac{dC}{dV}} \qquad (8.1)$$

the carrier profile could be calculated. The results is shown in fig. 8.5(b) and shows an electron accumulation at the surface, similar to reports in literature [129]. Integrating the carrier profile resulted in a accumulated surface charge of approx. 2×10^{13} cm^{-2}. The calculated bulk concentration was in the range of 9×10^{18} cm^{-3} and therefore close to the expected value. The extracted flatband potential and the value for the open-circuit potential V_{OCP} = -0.1 V vs. SCE yielded in a downwards band bending of approx. 0.8 eV, which is also consistent with results shown in literature [124].

The impedance characteristics were significantly changed after oxidation. Impedance spectroscopy measurements showed that a larger number of elements
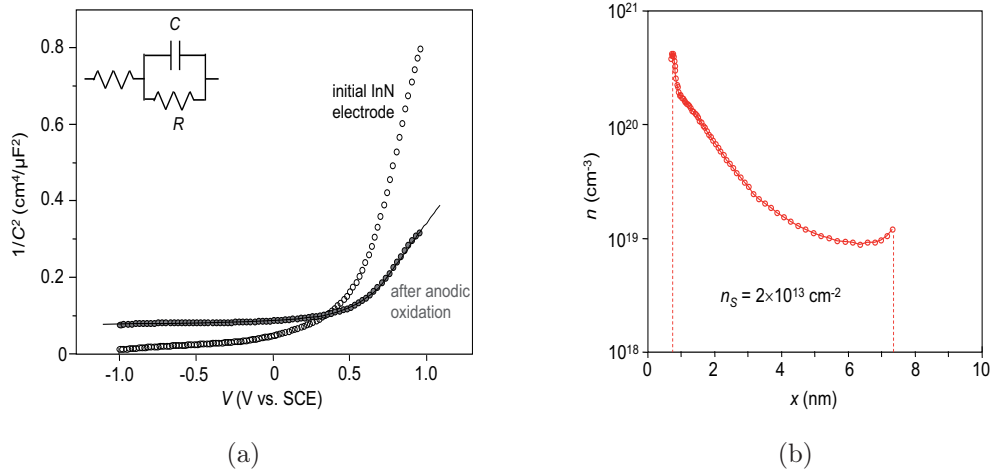
Figure 8.5: (a) Mott-Schottky plots of the n-doped InN electrode in 0.1 MH_2SO_4. (b) carrier profile for the initial InN electrode extracted from the Mott-Schottky plot.

was necessary for an adequate fitting in the whole frequency range, but the single elements could not be clearly ascribed to depletion- or double layer. However, the Mott-Schottky plot extracted from the simple RC-equivalent circuit still showed MOS-like characteristics: At cathodic potentials corresponding to electron accumulation, the value for the capacitance was limited to 2.25 $\mu F/cm^2$. For a dielectric constant of 10, this corresponds to a oxide layer thickness of approx. 4 nm, which is correlates well with the results from TEM measurements. At anodic potentials, the Mott-Schottky plot showed a constant slope corresponding to a doping concentration of approx. 1×10^{19} cm^{-3}.

In summary, the measurements have shown that indium nitride electrodes are oxidized under anodic conditions, similar to gallium nitride. This limits the stability especially at high anodic potentials and in oxidizing electrolytes.

Chapter 9

Summary

In this work, the characteristics of oxygen-terminated diamond electrodes exposed to different surface treatments have been analyzed. It was shown that the characterisitcs of oxygen-terminated diamond depend on the used oxidation treatment, which can be explained by different carbon-oxygen surface functionalities and different amounts of sp^2-content. The analysis was performed by electrochemical characterization methods which were correlated to the results of X-ray photoemission spectroscopy (XPS) measurements. The oxidation treatments which were analyzed were wet-chemical oxidation in H_2SO_4:CrO_3 followed by H_2SO_4:H_2O_2, anodic oxidation in 0.1 M KOH, a soft RF oxygen plasma treatment and reactive ion etching in argon/oxygen plasma.

Wet-chemical oxidation converts the hydrogen termination of the as-grown surface into one monolayer of carbon-oxygen groups with a surface coverage of 100 % or slightly below. The surface functionalities are mainly hydroxyl- and ether groups. Anodic oxidation in alkaline electrolyte is a very effective method for the surface oxidation of diamond electrodes, since it leads to a fully oxidized surface and removes all non-diamond components. This treatment induces mainly ether groups on the diamond surface as well as a chemisorbed layer of 1 nm in thickness.

A soft RF oxygen plasma induces additional surface carbonyl groups. The change in the sp^2-content was in the range of the detection limit of the XPS analysis. Reactive ion etching in argon/oxygen plasma, which is used e.g. for the fabrication of microelectrode arrays for FET structures, induces even at relative low power (25 W) a significant amount of defects. In addition, the diamond surface is converted into an α-carbon film with the thickness of approx. 4 nm. These surface damage effects have to be considered if plasma processes are used for the diamond technology, because they can significantly affect the device characteristics. After argon/oxygen plasma, the initial diamond surface characteristics can be almost restored by hydrogen plasma at about 700 °C. The effect of this recovery treatment is most probably a conversion of the α-carbon layer into graphite, which is then etched by the hydrogen plasma.

After all four surface treatments, the diamond electrodes showed a typical potential window of water dissociation of 3.0 to 3.5 eV and low background currents within this potential window. However, the oxidation treatments lead to slight differences, e.g. in the adsorption characteristics and in the hydrogen evolution. For nanocrystalline diamond electrodes, the RF oxygen plasma process leads to an additional contribution to the oxygen evolution current at lower potentials, which could be ascribed to the grain boundary defects. Besides, the diamond electrodes generally showed slightly increased background currents in alkaline compared to acidic electrolytes.

One main part of the analysis was the analysis of the diamond electrodes by impedance spectroscopy to extract the electronic surface barrier in contact to the electrolytes. It was shown that the value for the surface barrier ranges from approx. 1.0 eV for RF oxygen plasma to 1.7 eV for anodic oxidation. In the case of argon/oxygen plasma, this value might be even lower than for oxygen plasma. These differences in the electrode characteristics can be explained by the different amounts of sp^2-contents and by the different carbon-oxygen surface groups, as resolved by XPS measurements.

Three examples for the application of diamond electrodes have been shown in this work. Diamond electrodes are promising for the oxidation of organic compounds like ethanol. The main advantage compared to metal electrodes is the stability at high anodic potentials, which enables the complete oxidation of these compounds to CO_2 and avoids fouling due to organic intermediates which could remain on the electrode surface.

Another interesting application is the fabrication of microelectrode arrays completely in diamond, which are stable even in harsh environments. By using a nitrogen-doped cap layer on top of a highly boron-doped contact layer, the background current could be reduced by approx. two orders of magnitude. The active microelectrode areas were defined by e-beam lithography and plasma etching, resulting in dimensions of the single microelectrodes below 1 μm, which is much smaller than for comparable structures shown in literature. The fabricated sub-microelectrode array showed typical characteristics of hemispherical diffusion and high signal current densities, which correlated well with theoretical data. For the fabrication process, it was important to restore the initial surface characterisitcs after the etching process, using the hydrogen plasma treatment mentioned above. Otherwise, the microelectrode performance was significantly lower.

A similar electrode concept is the use of diamond as a support for catalytically active nanoparticles. It was shown that in the case of nanocrystalline diamond, the grain boundaries provide a low-resistive path from the particles across the cap layer to a highly doped contact layer underneath. This could be very promising for the fabrication of such electrodes with very low background current.

Both the microelectrode array and the NCD electrode with nanoparticles showed typical features of a heterogeneous electrode, where the small active areas determine the signal to be measured and the large surrounding area the background

current. From the electrochemical analysis, it was possible to extract a model for such electrodes, which could be important for further optimization.

Finally, it was shown that the same characterization methods which have been used for the diamond electrodes can also be used in the case of III-nitrides. The characteruzed GaN and InN electrodes showed a potential window of water dissociation of approx. 3.0 V and 2.0 - 2.5 V, respectively, together with low background currents similar to the case of diamond. However, it was shown that these materials are not stable under strongly oxidizing conditions, although also these materials are considered to be chemically very inert. The stability under such harsh conditions is therefore one of the main advantages of oxygen-terminated diamond electrodes.

Bibliography

[1] K. Kobashi, *Diamond Films.* Elsevier, 2005.

[2] R. S. Sussmann, ed., *CVD-Diamond for Electronic Devices and Sensors.* John Wiley & Sons, 2009.

[3] A. Aleksov, M. Kubovic, N. Kaeb, U. Spitzberg, A. Bergmair, G. Dollinger, T. Bauer, M. Schreck, B. Stritzker, and E. Kohn, "Diamond field effect transistors - concepts and challenges," *Diamond and Related Materials*, vol. 12, pp. 391–398, 2003.

[4] E. Kohn, M. Adamschik, P. Schmid, A. Denisenko, A. Aleksov, and W. Ebert, "Prospects of diamond devices," *Journal of Physics D: Applied Physics*, vol. 34, pp. R77–R85, 2001.

[5] A. Fujishima, T. Einaga, T. Rao, and D. A. Tryk, eds., *Diamond Electrochemistry.* Elsevier Publ., 2005.

[6] Y. Kado, T. Goto, and R. Hagiwara, "Stability of a boron-doped diamond electrode in molten chloride systems," *Diamond and Related Materials*, vol. 18, pp. 1186–1190, 2009.

[7] C. H. Hamann, A. Hamnett, and W. Vielstich, *Electrochemistry.* Wiley VCH, 2007.

[8] H. B. Martin, A. Argoitia, U. Landau, A. Anderson, and J. C. Angus, "Hydrogen and oxygen evolution on boron-doped diamond electrodes," *Journal of the Electrochemical Society*, vol. 143, pp. L134–L136, 1996.

[9] Y. Cai, A. B. Anderson, J. C. Angus, and L. N. Kostadinov, "Hydrogen evaluation on diamond electrodes by the Volmer-Heyrovski mechanism," *Journal of the Electrochemical Society*, vol. 154, pp. F36–F43, 2007.

[10] H. B. Suffredini, S. Machado, and L. A. Avaca, "The water decomposition reactions on boron-doped diamond electrodes," *Journal of the Brazilian Chemical Society*, vol. 15, pp. 16–21, 2004.

[11] L. Chen, D. Guay, and A. Lasia, "Kinetics of the hydrogen evolution reaction on ru $=_2$ and iro$_2$ oxide electrodes in h$_2$so$_4$ solution: An ac impedance study," *Journal of the Electrochemical Society*, vol. 143, pp. 3576–3584, 1996.

[12] W. Vielstich, A. Lamm, and H. A. Gasteiger, eds., *Handbook of fuel cells*. Wiley, 2003.

[13] H. B. Martin, A. Argoitia, J. C. Angus, and U. Landau, "Voltammetry studies of single-crystal and polycrystalline diamond electrodes," *Journal of the Electrochemical Society*, vol. 146, pp. 2959–2964, 1999.

[14] J. A. Bennet, J. Wang, Y. Show, and G. Swain, "Effect of sp^2-bonded nondiamond carbon impurity on the response of boron-doped polycrystalline diamond thin-film electrodes," *Journal of the Electrochemical Society*, vol. 151, pp. E306–E314, 2004.

[15] J. Iniesta, P. A. Michaud, M. Panizza, G. Cerisola, A. Aldaz, and C. Comninellis, "Electrochemical oxidation of phenol at boron-doped diamond electrode," *Electrochimica Acta*, vol. 46, pp. 3573–3578, 2001.

[16] P. L. Hagans, P. M. Natisham, B. R. Stoner, and W. E. O´Grady, "Electrochemical oxidation of phenol using boron-doped diamond electrodes," *Journal of the Electrochemical Society*, vol. 148, pp. E298–E301, 2001.

[17] D. Gandini, E. Mahe, P. A. Michaud, W. Haenni, A. Perret, and C. Comninellis, "Oxidation of carboxylic acids at boron-doped diamond electrodes for wastewater treatment," *Journal of Applied Electrochemistry*, vol. 30, pp. 1345–1350, 2000.

[18] M. A. Rodrigo, P. A. Michaud, I. Duo, M. Panizza, G. Cerisola, and C. Comninellis, "Oxidation of 4-chlorophenol at boron-doped diamond electrode for wastewater treatment," *Journal of the Electrochemical Society*, vol. 148, pp. D60–D64, 2001.

[19] M. Panizza, P. A. Michaud, G. Cerisola, and C. Comninellis, "Anodic oxidation of 2-naphtol at boron-doped diamond electrodes," *Journal of Electroanalytical Chemistry*, vol. 507, pp. 206–214, 2001.

[20] M. Fryda, A. Dietz, D. Herrmann, A. Hampel, L. Schaefer, C. P. Klages, A. Perret, W. Haenni, C. Comninellis, and D. Gandini, "Wastewater treatment with diamond electrodes," *Electrochemical Society Proceedings*, vol. 32, pp. 473–483, 1999.

[21] J. A. Garrido, A. Härtl, S. Kuch, M. Stutzmann, O. A. Williams, and R. B. Jackman, "pH sensors based on hydrogenated diamond surfaces," *Applied Physics Letters*, vol. 86, p. 073504, 2005.

[22] K. S. Song, Y. Nakamura, Y. Sasaki, M. Degawa, J. H. Yang, and H. Kawabata, "pH-sensitive diamond field-effect transistors (fets) with directly aminated channel surface," *Analytica Chimica Acta*, vol. 573-574, pp. 3–8, 2006.

[23] M. Dipalo, C. Pietzka, A. Denisenko, H. El-Hajj, and E. Kohn, "O-terminated nano-dimaond ISFET for applications in harsh environment," *Diamond and Related Materials*, vol. 17, pp. 1241–1247, 2008.

[24] A. Denisenko, G. Jamornmarn, H. El-Hajj, and E. Kohn, "pH sensor on O-terminated diamond using boron-doped channel," *Diamond and Related Materials*, vol. 16, pp. 905–910, 2007.

[25] M. Dipalo, Z. Gao, J. Scharpf, C. Pietzka, M. Alomari, F. Medjdoub, J. F. Carlin, N. Grandjean, S. Delage, and E. Kohn, "Combining diamond electrodes with GaN heterostructures for harsh environment ISFETs," *Diamond and Related Materials*, vol. 18, pp. 884–889, 2009.

[26] T. Knickerbocker, T. Strother, M. P. Schwartz, J. N. Russell, J. Butler, L. M. Smith, and R. J. Hamers, "DNA-modified diamond surfaces," *Langmuir*, vol. 19, pp. 1938–1942, 2003.

[27] A. Härtl, E. Schmich, J. A. Garrido, J. Hernando, S. C. Catherino, S. Walter, P. Feulner, A. Kromka, D. Steinmüller, and M. Stutzmann, "Protein-modified nanocrystalline diamond films for biosensor applications," *Nature Materials*, vol. 3, pp. 736–742, 2004.

[28] G. J. Zhang, K. S. Song, Y. Nakamura, T. Ueno, T. Funatsu, I. Ohdomari, and H. Kawarada, "DNA micropatterning on polycrystalline diamond via one-step deirect amination," *Langmuir*, vol. 22, pp. 3728–3734, 2006.

[29] J. Kusterer, A. Alekov, A. Pasquarelli, R. Müller, W. Ebert, F. Lehmann-Horn, and E. Kohn, "A diamond-on-silicon patch-clamp-system," *Diamond and Related Materials*, vol. 14, pp. 2139–2142, 2005.

[30] Z. Gao, V. Carabelli, E. Carbone, E. Coombo, F. Demaria, M. Dipalo, S. Gosso, C. Manfredotti, A. Pasquarelli, Y. Xu, E. Vittone, and E. Kohn, "Transparent diamond microelectrode for biochemical application." Diamond and Related Materials.

[31] M. You, F. C.-N. Hong, S. Jeng, and S. M. Huang, "Low-temperature growth of highly transparent nanocrystalline diamond films on quartz glass by hot-filament chemical vapor deposition," *Diamond and Related Materials*, vol. 18, p. 155, 2009.

[32] P. T. Joseph, N.-H. Tai, Y.-C. Chen, H.-F. Cheng, and I.-N. Lin, "Transparent ultrananocrystalline diamond films on quartz substrate," *Diamond and Related Materials*, vol. 17, pp. 476–480, 2008.

[33] M. Dipalo, *Nanocrystalline Diamond Growth and Device Applications*. PhD thesis, Ulm University, 2008.

[34] H. El-Hajj, *Growth and Characterisation od Diamond delta-doped Layers for FET Applications*. PhD thesis, Ulm University, 2008.

[35] K. Janischowsky, W. Ebert, and E. Kohn, "Bias enhanced nucleation of diamond on silicon (100) in a HFCVD system," *Diamond and Related Materials*, vol. 12, pp. 336–339, 2003.

[36] K. Nassau, *Diamond films and coatings*, ch. Synthesis of bulk diamond: History and present status. Noyes Publ., 1993.

[37] M. Schreck, F. Hoermann, H. Roll, J. K. Lindner, and B. Stritzker, "Diamond nucleation on iridium buffer layers and subsequent textured growth: A route for the realization of single-crystal diamond films," *Applied Physics Letters*, vol. 78, p. 192, 2001.

[38] K. Janischowsky, *Wachstum hochorientierter Diamantschichten auf Silizium mittels Hot Filament CVD-Diamond*. PhD thesis, Friedrich Alexander Universität Erlangen-Nürnberg, 2003.

[39] M. Kunze, A. Vescan, G. Dollinger, A. Bergmaier, and E. Kohn, "δ-doping in diamond," *Carbon*, vol. 37, pp. 787–791, 1999.

[40] T. H. Borst, *Dotierte homoepitaktische Diamantschichten*. PhD thesis, Universität Ulm, 1995.

[41] T. H. Borst and O. Weis, "Electrical characterization of homoepitaxial diamond films doped with B, P, Li and Na during crystal grown," *Diamond and Related Materials*, vol. 4, p. 948, 1995.

[42] A. Aleksov, *Konzepte und Technologie für diamantbasierende Feldeffekttransistoren*. PhD thesis, Ulm University, 2002.

[43] S. M. Sze, *Physics of Semiconductor Devices*. John Wiley & Sons, 1981.

[44] P. W. May, W. J. Ludlow, M. Hannaway, P. J. Heard, J. A. Smith, and R. N. Rosser, "Raman and conductivity studies of boron-doped microcrystalline diamond, facetted nanocrystalline diamond and cauliflower diamond films," *Chemical Physics Letters*, vol. 446, pp. 103–108, 2007.

[45] A. T. Collins, "Diamond electronic devices - a critical appraisal," *Semiconductor Science and Technology*, vol. 4, pp. 605–611, 1989.

[46] M. Kasu, K. Ueda, H. Ye, Y. Yamaguchi, S. Sasaki, and T. Makimoto, "High RF outfut power for H-terminated diamond FETs," *Diamond and Related Materials*, vol. 15, 4-6, pp. 783–786, 2006.

[47] F. Maier, M. Riedel, B. Mantel, J. Ristein, and L. Ley, "Origin of surface conductivity in diamond," *Physical Review Lett.*, vol. 85, pp. 3472–3475, 2000.

[48] D. Kueck, A. Schmidt, A. Denisenko, and E. Kohn, "Analysis of passivated diamond surface channel FET in dual-gate configuration - localizing the surface acceptor," *Diamond and Related Materials*, 2009.

[49] H. El-Hajj, A. Denisenko, A. Kaiser, R. S. Balmer, and E. Kohn, "Diamond MISFET based on boron delta-doped channel," *Diamond and Related Materials*, vol. 17, pp. 1259–1263, 2008.

[50] A. Denisenko and E. Kohn, "Diamond power devices. concepts and limits," *Diamond and Related Materials*, vol. 14, pp. 491–498, 2005.

[51] J. Shirafuji and T. Sugino, "Electrical properties of daimond surfaces," *Diamond and Related Materials*, vol. 5, pp. 706–713, 1996.

[52] G. Sine, L. Ouattara, M. Panizza, and C. Comninellis, "Electrochemical behavior of fluorinated boron.-doped diamond," *Electrochemical and Solid-State Letters*, vol. 6, pp. D9–D11, 2003.

[53] T. Kondo, H. Ito, K. Kusakabe, K. Ohkawa, K. Honda, Y. Einaga, A. Fujishima, and T. Kawai, "Characterization and electrochemical properties of CF_4 plasma-treated boron-doped diamond sutfaces," *Diamond and Related Materials*, vol. 17, pp. 48–54, 2008.

[54] T. Kondo, H. Ito, K. Kusakabe, K. Ohkawa, K. Honda, Y. Einaga, A. Fujishima, and T. Kawai, "Characterisation and electrochemical properties of cf4 plasma-treated boron-doped diamond surfaces," *Diamond and Related Materials*, vol. 17, pp. 48–54, 2008.

[55] J. C. Angus, H. B. Martin, U. Landau, Y. E. Estefeeva, B. Miller, and N. Vinokur, "Conductive diamond electrodes: Applications in electrochemistry," *New Diamond and Frontier Carbon Technology*, vol. 9, pp. 175–187, 1999.

[56] D. M. Kolb, "An atomistic view on electrochemistry," *Surface Sciemce*, vol. 500, pp. 722–740, 2002.

[57] D. Becker and K. Jüttner, "Influence of surface inhomogenities of boron-doped CVD-diamond electrodes on reversible charge transfer reactions," *Journal of Applied Electrochemistry*, vol. 33, pp. 959–967, 2003.

[58] J. van de Lagemaat, D. Vanmaekelbergh, and J. J. Kelly, "Electrochemistry of homoepitaxial CVD diamond: energetics and electrode kinetics in aqueous electrolytes," *Journal of Electroanalytical Chemistry*, vol. 475, pp. 139–151, 1999.

[59] D. E. Yates, S. Levine, and T. W. Healy, "Site-binding model of the electrical double layer at the oxide/water interaface," *Journal of the Chemical Society, Faraday Transactions 1*, vol. 70, pp. 1807–1818, 1974.

[60] I. Larsson and P. Attard, "Surface charge of silver iodide and several metal oxides. are all surfaces nernstain?," *Journal of Colloid and Interface Science*, vol. 227, pp. 152–163, 2000.

[61] M. Bayer, C. Uhl, and P. Vogl, "Theoretical study of electrolyte gate AlGaN/GaN field effect transistor," *Journal of Applied Physics*, vol. 97, p. 033703, 2005.

[62] Y. V. Pleskov, Y. E. Estefeeva, M. D. Krotova, V. Y. Mishuk, V. A. Laptev, Y. N. Polyanov, and Y. M. Borzdov, "Effect of crystal structure on the behavior of diamond electrodes," *Journal of the Electrochemical Society*, vol. 149, pp. E260–E264, 2002.

[63] M. N. Latto, D. J. Riley, and P. W. May, "Impedance studies of boron-doped CVD diamond electrodes," *Diamond and Related Materials*, vol. 9, pp. 1181–1183, 2000.

[64] J. R. Macdonald, ed., *Impedance Spectroscopy.* John Wiley Publ., 1987.

[65] T. Kondo, K. Honda, D. A. Tryk, and A. Fujishima, "Covaent modification of single-crystal diamond electrode surface," *Journal of the Electrochemical Society*, vol. 152, pp. E18–E23, 2005.

[66] H. Girard, N. Simon, D. Ballutaud, M. Herlem, and A. Etcheberry, "Effect of anodic and cathodic treatments on the chrage transfer of boron doped diamond electrodes," *Diamond and Related Materials*, vol. 16, pp. 316–325, 2007.

[67] Y. V. Pleskov, V. Y. Mishuk, M. A. Abaturov, V. V. Elkin, M. D. Krotova, V. P. Varnin, and I. G. Teremetskaya, "Synthetic semiconductor diamond electrodes: determination of acceptor concentration by linear and non-linear impedance measurements," *Journal of Electroanalytical Chemistry*, vol. 396, pp. 227–232, 1995.

[68] H. El-Hajj, A. Denisenko, A. Bergmair, G. Dollinger, M. Kubovic, and E. Kohn, "Characterization of boron δ-doped diamond for electronic applications," *Diamond and Related Materials*, vol. 17, pp. 409–414, 2008.

[69] W. P. Gomes and F. Cardon, "Electron energy levels in semiconductor electrochemistry," *Progress in Surface Science*, vol. 12, pp. 155–216, 1982.

[70] T. J. Davies and R. G. Compton, "The cyclic and linear sweep voltammetry of regular and random arrays of microdisc electrodes: Theory," *Journal of Electroanalytical Chemistry*, vol. 585, pp. 63–82, 2005.

[71] G. Speranza, S. Torrengo, L. Minati, M. Filippi, M. Castellino, C. Manfredotti, C. Manfredotti, M. Dipalo, A. Pasquarelli, E. Kohn, H. El-Hajj, and E. Vitone, "Characterisation of UV-irradiated nanocrystalline diamond," *Diamond and Related Materials*, vol. 17, pp. 1194–1198, 2008.

[72] A. Härtl, J. A. Garrido, S. Nowy, R. Zimmermann, C. Werner, D. Horinek, R. Netz, and M. Stutzmann, "The ion sensitivity of surface conductive single-crystal diamond," *Journal of the American Chemical Society*, vol. 129, pp. 1287–1292, 2007.

[73] H. Notsu, I. Yagi, T. Tetsuma, D. A. Tryk, and A. Fujishima, "Surface carbonyl groups on oxydized diamond electrodes," *Journal of Electroabalytical Chemistry*, vol. 492, pp. 31–37, 2000.

[74] G. Sine, D. Smida, M. Limat, G. Foti, and C. Comninellis, "Microemulsion synthesized Pt/Ru/Sn nanoparticles on BDD for alcohol electro-oxidation," *Journal of the Electrochemical Society*, vol. 154, pp. B170–B174, 2007.

[75] T. Kondo, H. Ito, K. Kusakabe, K. Ohkawa, Y. Einaga, A. Fujishima, and T. Kawai, "Plasma etching treatment for surface modification of boron-doped diamond elesctrodes," *Electrochimica Acta*, vol. 52, pp. 3841–3848, 2007.

[76] U. Hilleringmann, *Silizium Halbleitertechnologie*. B.G. Teubner Stuttgart, 2004.

[77] C. Pietzka, A. Denisenko, L. A. Kibler, J. Scharpf, Y. Men, and E. Kohn, "Surface modification of single-crystal boron-doped diamond electrodes for low background current," *Diamond and Related Materials*, vol. 18, pp. 816–819, 2009.

[78] C. Fadley, "Angle-resolved x-ray photoelectron spectroscopy," *Progress in Surface Science*, vol. 16, pp. 275–388, 1984.

[79] R. Berman, *Density, lattice constant and expension coefficients of diamond, in: Growth and properties of diamond*. INSPEC, 1994.

[80] K. Yanamoto, H. Watanabe, and M. Ogura, "XPS study of diamond surface after mass-separated low-energy phosphoros ion irradiation," *Diamond and Related Materials*, vol. 14, pp. 389–392, 2005.

[81] J. S. Foord and C. S. Goeting, "Diamond electrodes modified by argon ion bombardement," *physica status solidi (a)*, vol. 201, pp. 2439–2443, 2004.

[82] W. M. Lau, L. J. Huang, I. Bello, Y. M. Yiu, and S. T. Lee, "Modification of surface band bending of diamond by low energy argon and carbon ion bombardement," *Journal of Applied Physics*, vol. 75, pp. 3385–3391, 1994.

[83] P. K. Baumann and R. J. Nemanich, "Electron affinity and schottky barrier height of metal-diamond (100), (111), and (110) interfaces," *Journal of Applied Physics*, vol. 83, pp. 2072–2082, 1998.

[84] A. Aleksov, A. Denisenko, M. Kunze, A. Vescan, A. B. G. Dollingrer, W. Ebert, and E. Kohn, "Diamond diodes and transistors," *Semiconductor Science and Technology*, vol. 18, pp. S59–S66, 2003.

[85] Y. G. Chen, M. Ogura, and H. Okushi, "Temperature dependence on current voltage characteristics of nickel/diamond schottky diodes on high quality boron-doped homoepitaxial diamond film," *Applied Physics Letters*, vol. 82, no. 24, pp. 4367–4369, 2003.

[86] N. Simon, H. Girard, D. Ballutaud, S. Ghodbane, A. Deneuville, M. Herlem, and A. Etcheberry, "Effect of H and O termination on the charge transfer of moderately boron doped diamond electrodes," *Diamond and Related Materials*, vol. 14, pp. 1179–1182, 2005.

[87] H. Girard, N. Simon, D. Ballutaud, E. de la Rochefoucauld, and A. Etcheberry, "Effects of controlled anodic treatments on electrochemical behavior of boron doped diamond," *Diamond and Related Materials*, vol. 16, pp. 888–891, 2007.

[88] S. Ferro, A. D. Battisti, I. Duo, C. Comninellis, W. Haenni, and A. Perret, "Chlorine evolution at highly boron-doped diamond electrodes," *Journal of the Electrochemical Society*, vol. 147, pp. 2614–2619, 2000.

[89] A. Grill, V. Patel, and C. Jahnes, "Novel low k dielectrics based on diamond-like carbon materials," *Journal of the Electrochemical Society*, vol. 145, pp. 1649–1653, 1998.

[90] F. Hernandez, A. Denisenko, and E. Kohn, "Nanoscale surface modification of diamond for enhanced electrochemical sensing: Electrochemical characteristics of the surface modification," *Diamond and Related Materials*, vol. 16, pp. 867–871, 2007.

[91] T. Iwasita and E. Pastor, "A dems and fTIR spectroscopic investigation of adsorbed ethanol on polycrystalline platinum," *Electrochimica Acta*, vol. 39, pp. 531–537, 1994.

[92] J. C. Forti, P. Olivi, and A. R. de Andrade, "Electrochemical behavior of ethanol oxidation on a $Ti/Ru_{0.3}Ti_{0.7-x}Sn_{(x)}O_2$-electrode," *Journal of the Electrochemical Society*, vol. 150, pp. E222–E226, 2003.

[93] P. Bommersbach, M. Mohamedi, and D. Guay, "Electro-oxidation of ethanol at sputter-depositd platinum-tin catalysts," *Journal of the Electrochemical Society*, vol. 154, pp. B876–B882, 2007.

[94] A. L. Colley, C. G. Williams, U. D. Johansson, M. E. Newton, P. R. Unwin, N. R. Wilson, and J. V. Macpherson, "Examination of the spatially heterogenous electroactivity of boron-doped diamond microarray electrodes," *Analytical Chemistry*, vol. 78, pp. 2539–2548, 2006.

[95] M. Pagels, C. E. Hall, N. S. Lawrence, A. Meredith, T. G. J. Jones, H. P. Godfried, C. S. J. Pickles, J. Wilman, C. E. Banks, R. G. Compton, and L. Jiang, "All-diamond microelectrode array devices," *Analytical Chemistry*, vol. 77, pp. 3705–3708, 2005.

[96] M. Bonnauron, S. Saada, L. Rousseau, G. Lissorgues, C. Mer, and P. Bergonzo, "High aspect ratio diamond microelectrode array for neuronal activity measurements," *Diamond and Related Materials*, vol. 17, pp. 1399–1404, 2008.

[97] K. L. Soh, W. P. Kang, J. L. Davidson, S. Basu, Y. M. Wong, D. E. Cliffel, A. B. Bonds, and G. M. Swain, "Diamond-derived microelectrodes array for electrochemical analysis," *Diamond and Related Materials*, vol. 13, pp. 2009–2015, 2004.

[98] B. V. Sarada, T. N. Rao, D. A. Tryk, and A. Fujishima, "Electrochemical characterization of highly boron-doped diamond microelectrodes in aqueous electrolyte," *Journal of the Electrochemical Society*, vol. 146, pp. 1469–1471, 1999.

[99] J. M. Shannon, "A majority-carrier camel diode," *Applied Physics Letters*, vol. 35, pp. 63–65, 1979.

[100] M. Kubovic, H. El-Hajj, J. E. Butler, and E. Kohn, "Diamond merged diode," *Diamond and Related Materials*, vol. 16, pp. 1033–1037, 2007.

[101] C. Pietzka, A. Denisenko, M. Dipalo, and E. Kohn, "Nano-crystalline diamond electrodes with cap layer decorated by gold particles," *Diamond and Related Materials*, vol. 19, pp. 56–61, 2010.

[102] A. Denisenko, C. Pietzka, L. A. Kibler, and E. Kohn, "Lateral depletion of contact to metallic nanoparticle on boron-doped diamond electrodes," *Journal of the Electrochemical Society*, vol. 157, pp. H342–H348, 2010.

[103] A. T. Collins, *Properties and Growth of Diamond*, ch. Breakdown field and saturated carrier velocity in diamond, p. 228. INSPEC, 1994.

[104] T. J. Davies, S. Ward-Jones, C. E. Banks, J. del Campo, R. Mas, F. X. Munoz, and R. G. Compton, "The cyclic and linear sweep voltammetry of regular arrays of microdisc electrodes: Fitting of experimental data," *Journal of Electroanalytical Chemistry*, vol. 585, pp. 51–62, 2005.

[105] I. Gonzalez-Gonzalez, D. A. Tryk, and C. R. Cabrera, "Polycrystalline boron-doped diamond films as supports for methanol oxidation electrocatalysts," *Diamond and Related Materials*, vol. 15, pp. 275–278, 2006.

[106] F. Montilla, E. Morallon, I. Duo, C. Comninellis, and J. L. Vazquez, "Platinum particles deposited on synthetic boron-doped diamond surfaces. application to methanol oxidation," *Electrochimica Acta*, vol. 48, pp. 3891–3897, 2003.

[107] Y. Zhang, V. Suryanarayanan, I. Nakazawa, S. Yoshihara, and T. Shirakashi, "Electrochemical behavior of Au nanoparticle deposited on as-grown and O-termijnated diamond electrodes for oxygen reduction in alkaline solution," *Electrochimica Acta*, vol. 49, pp. 5235–5240, 2004.

[108] B. Piela and P. Wrona, "Capacitance of the gold electrode in 0.5 m h$_2$so$_4$ solution: a.c. impedance studies," *Journal of Electroanalytical Chemistry*, vol. 388, pp. 69–79, 1995.

[109] A. Sarapuu, M. Nurmik, H. Mändar, A. Rosental, T. Laaksonen, K. Konturi, D. J. Schiffrin, and K. Tammeveski, "Electrochemical reduction of oxygen on nanostructured gold electrodes," *Journal of Electronanlytical Chemistry*, vol. 612, pp. 78–86, 2008.

[110] O. Ambacher, M. Eickhoff, A. Link, M. Hermann, M. Stutzmann, F. Bernardini, V. Fiorentini, Y. Smorchkova, J. Speck, U. Mishra, W. Scharff, V. Tilak, and L. F. Eastman, "Electronics and sensors based on pyroelectric AlGaN/GaN heterostructures," *physica status solidi (c)*, vol. 0, pp. 1878–1907, 2003.

[111] F. Medjdoub, M. Alomari, J.-F. Carlin, M. Gonschorek, E. Feltin, M. A. Py, N. Grandjean, and E. Kohn, "Barrier-layer downscaling of InAlN/GaN HEMTs," *IEEE Electron Device Letters*, vol. 29, p. 422, 2008.

[112] N. A. Chaniotakis, Y. Alifragis, G. Konstantinidis, and A. Georgakilas, "Gallium nitride-based potentiometric anion sensor," *Analytical Chemistry*, vol. 76, pp. 5552–5556, 2004.

[113] S. J. Pearton, B. S. Kang, S. Kim, F. Ren, B. P. Gila, C. R. Abernathy, J. Lin, and S. N. G. Chu, "GaN-based diodes and transisrors for chemical, gas, biological and pressure sensing," *J. Phys.: Condens. Matter*, vol. 16, pp. R961–R994, 2004.

[114] G. Steinhoff, M. Herrmann, W. J. SChaff, L. F. Eastman, M. Stutzmann, and M. Eickhoff, "pH response of GaN surfaces and its application for pH-sensitive field-effect transistors," *Applied Physics Letters*, vol. 83, pp. 177–179, 2003.

[115] B. S. Kang, H. T. Wang, F. Ren, M. Hlad, B. P. Gila, C. R. Abernathy, S. J. Pearton, C. Li, Z. Low, J. Lin, J. W. Johnson, P. Rajagopal, J. C. Roberts, E. L. Piner, and K. J. Linthicum, "Role of gate oxide in AlGaN/GaN high-electron mobility transistor pH sensors," *Journal of Electronic Materials*, vol. 37, pp. 550–553, 2007.

[116] T. Kokawa, T. Sato, and H. H. anf T. Hashizume, "Liquid-phase sensors using open-gate AlGaN/GaN high electron mobility transistor structure," *Journal of Vacuum Science and Technology*, vol. B24, pp. 1972–1976, 2006.

[117] C. Pietzka, A. Denisenko, M. Alomari, F. Medjdoub, J. F. Carlin, E. Feltin, N. Grandjean, and E. Kohn, "Effect of anodic oxidation on the characteristics of lattice-matched AlInN/GaN heterostructures," *Journal of Electronic Materials*, vol. 37, pp. 616–623, 2008.

[118] A. Denisenko, C. Pietzka, A. Chuvilin, U. Kaiser, H. Lu, W. J. Scharff, and E. Kohn, "Depletion of surface accumulation charge in InN by anodic oxidation," *Journal of Applied Physics*, vol. 105, p. 033702, 2009.

[119] A. Pakes, P. Skeldon, G. E. Thompson, J. W. Fraser, S. Moisa, G. I. Sproule, M. J. Graham, and S. B. Newcomb, "Anodic oxidation of gallium nitride," *Journal of Material Science*, vol. 38, pp. 343–349, 2003.

[120] S. Chevtchenko, X. Ni, Q. Fan, A. A. Baski, and H. Morkoc, "Surface band bending of a-plane GaN studued by Kelvin force microscopy," *Applied Physics Letters*, vol. 88, p. 122104, 2006.

[121] G. Koley and M. G. Spencer, "Surface potential measurements on gan and algan/gan heterostructures by scanning Kelvin probe microscopy," *Journal of Applied Physics*, vol. 90, pp. 337–344, 2001.

[122] M. Okhubo, "Effects of dissolved oxygen on anodic etching of n-type GaN films using a sodium hydroxide electrolyte," *Japanese Journal of Applied Physics*, vol. 36, pp. L955–L958, 1997.

[123] T. D. Veal, I. Mahboob, L. F. Piper, C. F. McConville, H. Lu, and W. J. Scharff, "Indium nitride: Evidence of surface accumulation," *Journal of Vaccum Science Technology B*, vol. 22, pp. 2175–2178, 2004.

[124] V. Cimalla, M. Niebelschütz, G. Ecke, V. Lebedev, O. Ambacher, M. Himmerlich, S. Krischok, A. J. Schaefer, H. Lu, and W. J. Scharff, "Surface band bending at nominally undoped and Mg-doped InN by Auger electron spectroscopy," *physica status solidi (a)*, vol. 203, pp. 59–65, 2006.

[125] Y.-S. Lu, C. C. Huang, J. A. Yeh, C. F. Chen, and S. Gwo, "InN-based anion selective sensors in aqueous solutions," *Applied Physics Letters*, vol. 91, p. 202109, 2007.

[126] H. Lu, W. J. Scharff, and L. F. Eastman, "Surface chemical modification of InN for sensor apparatus," *Journal of Applied Physics*, vol. 96, pp. 3577–3579, 2004.

[127] A. Gagnaire, J. Joseph, and A. Etcheberry, "Spectroellipsometric study of the electrochemical modification of InP," *Journal of the Electrochemical Society*, vol. 134, pp. 2475–2478, 1987.

[128] J. Vigneron, M. Herlem, E. M. Khoumri, and A. Etcheberry, "Cathodic decomposition of InP studied by XPS," *Applied Surface Sciemce*, vol. 201, pp. 51–55, 2002.

[129] H. Lu, W. J. Schaff, L. F. Eastman, and C. E. Stutz, "Surface charge accumulation of InN films grown by molecular-beam epitaxy," *Applied Physics Letters*, vol. 82, pp. 1736–1738, 2003.

List of publications

- T. Zimmermann, M. Neuburger, P. Benkart, F. J. Hernandez-Guillen, C. Pietzka, M. Kunze, I. Daumiller, A. Dadgar, A. Krost, E. Kohn, "Piezoelectric GaN sensor structures", *IEEE Electron Device Letters*, vol. 27, pp. 309-312, 2006

- A. Denisenko, C. Pietzka, A. Romanyuk, H. El-Hajj, E. Kohn, "The electronic surface barrier of boron-doped diamond by anodic oxidation", *Journal of Applied Physics*, vol. 103, pp. 014904-014908, 2008

- M. Dipalo, C. Pietzka, A. Denisenko, H. El-Hajj, E. Kohn, "O-terminated nano-dimaond ISFET for Applications in harsh environment", *Diamond and Related Materials*, vol. 17, pp. 1241-1247, 2008

- C. Pietzka, A. Denisenko, M. Alomari, F. Medjdoub, J. F. Carlin, E. Feltin, N. Grandjean, E. Kohn, "Effect of Anodic Oxidation on the Characteristics of Lattice-Matched AlInN/GaN Heterostructures"´, *Journal of Electronic Materials*, vol. 37, pp. 616-623, 2008

- A. Denisenko, C. Pietzka, A. Chuvilin, U. Kaiser, H. Lu, W. J: Scharff, E. Kohn, "Depletion of surface accumulation charge in InN by anodic oxidation", *Journal of Applied Physics*, vol. 105, pp. 033702-033705, 2009

- C. Pietzka, A. Denisenko, L. A. Kibler, J. Scharpf, Y. Men, E. Kohn, "Surface modification of single-crystal boron-doped diamond electrodes for low background current", *Diamond and Related Materials*, vol. 18, pp. 816-818, 2009

- M. Dipalo, Z. Gao, J. Scharpf, C. Pietzka, M. Alomari, F. Medjdoub, J. F. Carlin, N. Grandjean, S. Delage, E. Kohn, "Combining diamond electrodes

with GaN heterostructures for harsh environment ISFETs", *Diamond and Related Materials*, vol. 18, pp. 884-889, 2009

- C. Pietzka, A. Denisenko, M. Dipalo, E. Kohn, "Nano-crystalline diamond electrodes with cap layer decorated by gold particles", *Diamond and Related Materials*, vol. 19, pp. 56-61, 2010

- A. Denisenko, C. Pietzka, L. A. Kibler, E. Kohn, "'Lateral depletion of contact to metallic nanoparticles on boron-doped diamond electrodes, *Journal of the Electrochemical Society*, vol. 157 (3), H342-H348 2010

- C. Pietzka, A. Denisenko, A. Romanyuk, P. J. Schäfer, L. A. Kibler, J. Scharpf, E. Kohn, "Electronic Surface Barrier Properties of Diamond oxidized by plasma treatments", *Diamond and Related Materials*, vol. 19, pp. 213-216, 2010

- A. Denisenko, A. Romanyuk, C. Pietzka, J. Scharpf, E. Kohn, "Surface structure and surface barrier characteristics of boron-doped diamond in electrolytes after CF4 plasma treatment in RF-barrel reactor", accepted to *Diamond and Related Materials*, 2010

Acknowledgements

Lebenslauf

Persönliche Daten

Geburtstag:	30.08.1980
Geburtsort:	Sögel
Adresse:	Friedenstr. 25, 89231 Neu-Ulm

Schulausbildung

08/1987 – 06/1991:	Grundschule in Meppen
08/1991 – 06/1993:	Orientierungsstufe in Meppem
08/1993 – 06/2000:	Windthorst-Gymnasium in Meppen Abschluss: Abitur

Hochschulstudium

10/2000 – 03/2006:	Studium der Elektrotechnik an der Universität Ulm
10/2004:	Studienarbeit: Piezoelektrische Sensorstrukturen mit AlGaN/GaN – HEMTs
07/2005 – 01/2006:	Diplomarbeit: Herstellung und Charakterisierung von GaN-basierenden pH-Sensoren
seit 04/2006:	wissenschaftlicher Mitarbeiter an der Universität Ulm, Institut für Elektronische Bauelemente und Schaltungen